UNIVERSITY OF SOUTHAMPTON

FACULTY OF ENGINEERING, SCIENCE AND MATHEMATICS

Optoelectronics Research Centre

Designing a Nanoscale X-ray Source: Towards Single Molecule X-ray Scattering

Christopher Andrew Froud

Thesis for the degree of Doctor of Philisophy

2007

UNIVERSITY OF SOUTHAMPTON

ABSTRACT

FACULTY OF ENGINEERING, SCIENCE AND MATHEMATICS

Optoelectronics Research Centre

Doctor of Philosophy

DESIGNING A NANOSCALE X-RAY SOURCE: TOWARDS SINGLE MOLECULE X-RAY SCATTERING

Christopher Andrew Froud

This thesis describes the design and construction of a femtosecond X-ray source based on high harmonic generation in an argon filled hollow capillary waveguide. The system has demonstrated excellent efficiency at generating harmonics in the range $20 - 50$ eV and is tuneable by exploiting the ionization-induced blue-shift that occurs in the waveguide.

Phase-matching is extremely important for efficient high harmonic generation. In a hollow capillary, this becomes a complicated three-dimensional problem. We show that the beating between the different transverse modes of the capillary has a prominent effect and develop a useful diagnostic technique for imaging their behaviour which could lead to a better understanding of phase-matching.

The X-ray source is designed for X-ray scattering experiments, which will ultimately allow the imaging of single biomolecules. Such experiments will require an intense, focused X-ray beam. Towards this aim, this thesis demonstrates focusing techniques based on tapered capillary optics, including a model that was developed to understand their behaviour.

Contents

Declaration v

Acknowledgements vii

1 Introduction **1**

2 Towards Single Molecule X-Ray Scattering **8**

2.1 Introduction 8

2.2 The importance of proteins structures 10

2.3 Radiation damage 12

2.4 Image reconstruction 14

2.5 Conceptual experiment 25

2.6 Summary 27

3 High Harmonic Generation **28**

3.1 Introduction 28

3.2 Single-atom response 29

3.2.1 Ionization 30

3.2.2 Propagation 34

3.2.3 Recombination 35

3.2.4 Quantum model 38

3.3 Macroscopic effects 39

3.3.1 Phase-matching 40

3.3.2 Absorption 49

3.3.3 Harmonic build-up 50
3.4 Summary 52

4 Generating High Harmonics 54
4.1 Introduction 54
4.2 High power, ultra-fast laser system 54
4.2.1 Ti:sapphire oscillator 55
4.2.2 Dazzler 56
4.2.3 Chirped pulse amplifier 60
4.2.4 Pulse characterisation 63
4.3 XUV generation 67
4.3.1 Hollow waveguide 68
4.3.2 Optical windows 75
4.3.3 High vacuum system 75
4.3.4 XUV filtering 77
4.3.5 XUV spectrometer 80
4.4 Results 81
4.4.1 Phase-matched generation 82
4.4.2 XUV spectrum 85
4.4.3 Spatial profile 91
4.4.4 Spatio-spectral mapping 92
4.5 Summary 95

5 Ionization induced effects in a capillary 96
5.1 Introduction 96
5.2 Experimental setup 97
5.3 Results and discussion 98
5.4 Summary 106

6 Mode propagation in a hollow waveguide 107
6.1 Introduction 107

6.2 Capillary modes 108
6.3 Experimental 112
6.4 Results 113
6.5 Simulation 116
6.6 Summary 119

7 Focusing X-rays **123**

7.1 Introduction 123
7.2 X-ray interactions with matter 124
    7.2.1 X-ray refractive index 125
    7.2.2 X-ray propagation and absorption 128
    7.2.3 Total external reflection 131
    7.2.4 Reflection coefficients 133
7.3 X-ray optics 134
    7.3.1 Zone plates 136
    7.3.2 Multi-layered mirrors 136
    7.3.3 Grazing incidence optics 137
    7.3.4 Capillary optics 138
7.4 Modelling 141
    7.4.1 Gaussian X-ray source 142
    7.4.2 Tapered surface 146
    7.4.3 Ray trajectories 146
    7.4.4 Surface normal 149
    7.4.5 Reflected intensity 149
    7.4.6 Simulation 150
    7.4.7 Camera 150
7.5 Experimental 151
    7.5.1 Fabrication 151
    7.5.2 Alignment 153
7.6 Results and discussion 154

7.7 Summary 158

8 Conclusions and future work **161**

A XUV Spectrometer **163**

A.1 Optical Design 163

A.2 Wavelength Calibration 164

A.2.1 Numerical Calibration 165

A.2.2 XUV Calibration Lamp 166

References **169**

DECLARATION OF AUTHORSHIP

I, Christopher Andrew Froud, declare that the thesis entitled ”Designing a Nanoscale X-Ray Source: Towards Single Molecule X-Ray Scattering” and the work presented in it are my own. I confirm that:

- this work was done wholly or mainly while in candidature for a research degree at this University;
- where any part of this thesis has previously been submitted for a degree or any other qualification at this University or any other institution, this has been clearly stated;
- where I have consulted the published work of others, this is always clearly attributed;
- where I have quoted from the work of others, the source is always given. With the exception of such quotations, this thesis is entirely my own work;
- I have acknowledged all main sources of help;
- where the thesis is based on work done by myself jointly with others, I have made clear exactly what was done by others and what I have contributed myself;
- parts of this work have been published as:

  Froud, C.A., Rogers, E.T., Hanna, D.C., Brocklesby, W.S., Praeger, M., de Paula, A.M., Baumberg, J.J., and Frey, J.G., *Soft-x-ray wavelength shift induced by ionization effects in a capillary*, Optics Letters, 31(3): 374, 2006. Also selected for the June 2006 issue of Virtual Journal of Ultrafast Science, Volume 5, Issue 6, Ultrafast Methods And Measurement Techniques, *www.vjultrafast.org*

Praeger, M., de Paula, A.M., Froud, C.A., Rogers, E.T.F., Stebbings, S.L., Brocklesby, W.S., Baumberg, J.J., Hanna, D.C., and Frey, J.G., *Spatially resolved soft X-ray spectrometry from single-image diffraction*, Nature Physics, 3(3): 176-179, 2007.

Signed: ______________________________

Date: ______________________________

Acknowledgements

It was late summer 2002, not long before I was due to graduate from my undergraduate degree and I was sat having coffee with Jeremy Frey. He and Bill Brocklesby had recently been awarded a generous pot of money from the Research Council's Basic Technology programme and he was excitedly explaining his *big idea* to me. They were going to build a powerful *X-ray laser* that would be able to image single molecules. The idea captivated me.

Six months later and I was the founder member of the *Ultra-fast X-ray Group*. For his assistance in those early days, I am indebted to James Gates, for his patience with answering my endless questions—"How does this work?" or "What happens if I press that?" Especially considering James was trying to write-up at the time.

This was an exciting time. The group grew to include Ana de Paula and Matthew Praeger, with whom I spent many happy hours in the lab. Between us, the former Physics stores[1]were transformed into a high-tech laser laboratory. Later, Sarah Stebbings, Ben Mills, Ed Rogers, James Grant-Jacob and Richard Chapman joined the group. They have been a fantastic group to work with. We have shared the successes together and helped each other through frustrating times when experiments refused to work.

Working on such an inter-disciplinary project has given me the opportunity to work with a diverse range of people. In particular, I'd like to thank Jeremy Baumberg and Dave Hanna for their general advice and use-

---

[1] Thanks Vince—I'm not sure you're ever going to forgive us for stealing your store room.

ful conversations and from the Rutherford Appleton Laboratory, I'd like to thank Graham Hirst for many useful conversations and Gareth Derbyshire for helping us to get our X-ray spectrometer working properly!

The project would not have been possible without the specialist skills available within the wider University community. From the Optoelectronics Research Centre (ORC), I am very grateful to Andy Webb for his skill in fabricating and drilling capillary and Gilberto Brambilla for fabricating fibre tapers. From the School of Chemistry, I greatly appreciate the skilled work of the glass-blowing workshop, and John Dyke and Alan Morris who very kindly provided us with the plans which form the basis of the helium discharge lamp we built to calibrate our X-ray spectrometer. I'd like to thank Phil Connell and the other staff from the mechanical workshop for their help in the design and construction of some of our experimental equipment, and Graham Chadwick from the electronics workshop for building the helium lamp power supply, and for some interesting rock-climbing conversations.

I must thank my family and Jane for helping me get this far and for their patience and love. I think that, for Jane, being the girlfriend of somebody writing a thesis might be harder work than doing it yourself. Thanks for washing my socks and cooking me dinner when I didn't have the time.

I've been privileged to work with so many inspirational and talented people; none more so than my supervisors. Without Bill and Jeremy's endless enthusiasm and optimism, I doubt that I would ever have reached the point of writing this. There were many times that I have walked into one of their offices carrying a bewildering pile of graphs to leave feeling that the whole world made sense. Their insight has taught me new ways of thinking.

Finally, to everyone who asked, ″Have you finished yet?″ I can now confidently say, ″Yes, I have!″

“God does not play dice with the universe. He plays an ineffable game of his own devising, which might be compared, from the perspective of any of the other players, to being involved in an obscure and complex version of poker in a pitch dark room, with blank cards, for infinite stakes, with a dealer who won’t tell you the rules, and who smiles all the time.”

Terry Pratchett, *“Good Omens”*

Chapter 1

Introduction

The discovery of X-rays in 1896 by Willhelm Röntgen [1] is an important milestone in the history of science. His discovery revealed a new world, hidden from our own eyes, sparking a revolution in scientific and medical imaging techniques. X-rays give access to atomic scale spatial resolution and have proved invaluable for the structural analysis of solid-state materials, in atomic physics and molecular chemistry and in the life-sciences where they have aided the discovery of the building blocks of life, including DNA. The invention of the laser in 1960 [2, 3] started a chain of developments, producing progressively shorter pulsed light sources which have offered us insight into the temporal dynamics of events on ever decreasing timescales. Today, it is routine to generate femtosecond laser pulses in the infrared, which can be used to monitor atomic and electronic motion, however, the long wavelengths of these lasers prevent us from directly imaging molecular structure at atomic resolution. In the past decade, X-rays and femtosecond lasers have been combined to produce sources which take advantage of their respective spatial and temporal resolution, opening up a whole new field of structural dynamics.

A number of techniques exist for producing ultra-fast X-ray pulses; figure 1.1 summarizes the characteristic pulse length and energy profile avail-

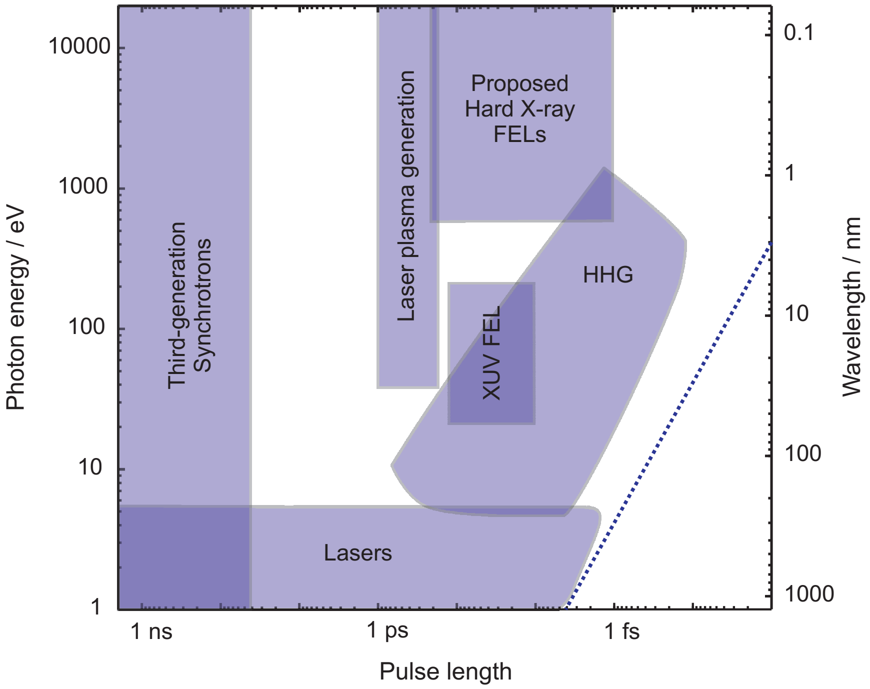

Figure 1.1: The pulse length and photon energy/wavelength ranges covered by a variety of ultra-fast X-ray sources. In general, higher photon energies are available from the accelerator based sources, such as the free electron lasers (FELs), while the shortest pulse lengths may be obtained by high harmonic generation (HHG). Currently, high harmonic generation is the only technique capable of producing X-ray pulses that approach the single optical-cycle limit for electromagnetic radiation, represented by the dashed line. Adapted from reference [4].

able from a variety of sources. All of these techniques rely, in some way, on femtosecond lasers, with the exception of third-generation synchrotron sources, such as Diamond, which are capable of producing X-ray bursts of 10–100 ps [5]. Femtosecond lasers are being employed in the next generation of accelerator based X-ray sources. These X-ray Free Electron Lasers (FELs), such as FLASH at the Deutsches Elektronen-Synchrotron (DESY), generate an ultra-short electron bunch in a femtosecond laser-driven photocathode which is then accelerated to gigaelectronvolt energies. As of 2007, FLASH was producing X-ray pulses in the range 13–50 nm with pulse lengths as short as 10 fs [6] and work is underway on the next generation of

FEL sources, such as the Linear Coherent Light Source (LCLS) at the Stanford Linear Accelerator Centre (SLAC) that will offer femtosecond pulses at hard X-ray wavelengths [7].

Another method for producing ultra-fast X-ray pulses, that will be used for the experiments described in this thesis, is high harmonic generation, a non-linear optical technique which up-converts infrared laser photons into X-ray photons. High harmonic generation is capable of producing the shortest X-ray pulses and currently holds the record for producing the shortest light pulse ever measured—a single isolated 130 attosecond pulse [8]. High harmonic generation typically produces 10^7 photons per pulse at 30 nm [9], comparing favourably with bending magnet radiation from synchrotron storage rings [5], across a region from 10 eV to a few kiloelectron volts [10]. This region is often referred to as the soft X-ray (SXR) and/or extreme ultraviolet (XUV) spectral region and is particularly interesting because it contains the K- and L-absorption edges of a large number of important elements. These edges are associated with the removal of core electrons from low lying atomic orbitals, which results in the strong absorption characteristics of matter in this spectral region. The strong atomic resonances characteristic of these spectral regions mean that all materials have absorption lengths of a few micrometers or less, which has historically held back development. However, while these resonances make the science technically challenging, they also provide an enormous amount of element specific and chemical information. Furthermore, the relatively short wavelengths provide an advantage for viewing small structures in microscopy and for writing small structures in lithography.

Figure 1.2 shows the region of the electromagnetic spectrum containing the soft X-ray and extreme ultraviolet. The soft X-ray region is placed just below the K-absorption edge of carbon at 250 eV and the hard X-ray region at several kiloelectron volts, while the XUV region is bounded by

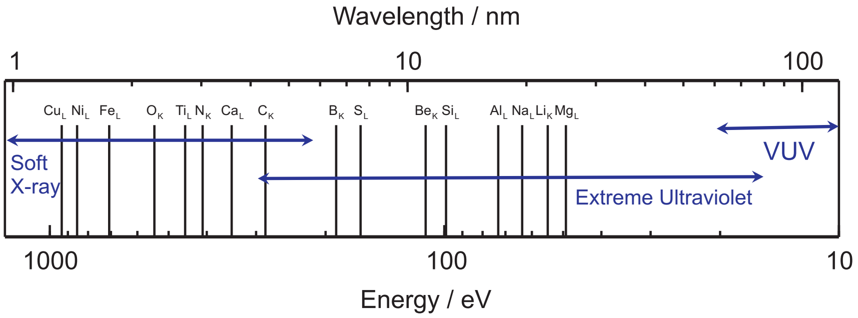

Figure 1.2: The region of the electromagnetic spectrum from the vacuum ultraviolet (VUV), through extreme ultraviolet to soft X-ray showing a number of important K- and L-absorption edges of elemental species. Data from reference [11].

the vacuum ultraviolet (VUV) at about 30 eV and the soft X-ray region at 250 eV [12]. A number of key absorption edges lie within this region, of particular interest are the L-absorption edge of silicon and, for the study of biological systems, the K-absorption edges of carbon, oxygen, and nitrogen. The region between the K-edges of carbon (284 eV, 4.37 nm) and oxygen (543 eV, 2.28 nm) define a region commonly called the *water window* (figure 1.3). This region is of particular interest for microscopy in the life sciences because of the relative transparency of water and natural contrast with carbon, as well as the possibility for element specific mapping of potassium or calcium that have L-edges in the water window [13].

In addition to the role of XUV in spectroscopy and microscopy, there is a growing interest in soft X-ray scattering. At first, this may seem surprising given that the wavelengths are too large to fit interatomic length scales, however, it proves to be ideal for imaging nanostructures. XUV scattering offers the possibility for diffraction limited lens-less imaging free from aberration using holographic techniques [15, 16] or phase inversion algorithms [17,18]. By tuning the X-ray wavelength to match particular absorption edges it is possible to enhance the contrast for particular elemental or chemical species [19]. This resonant X-ray scattering technique can be used

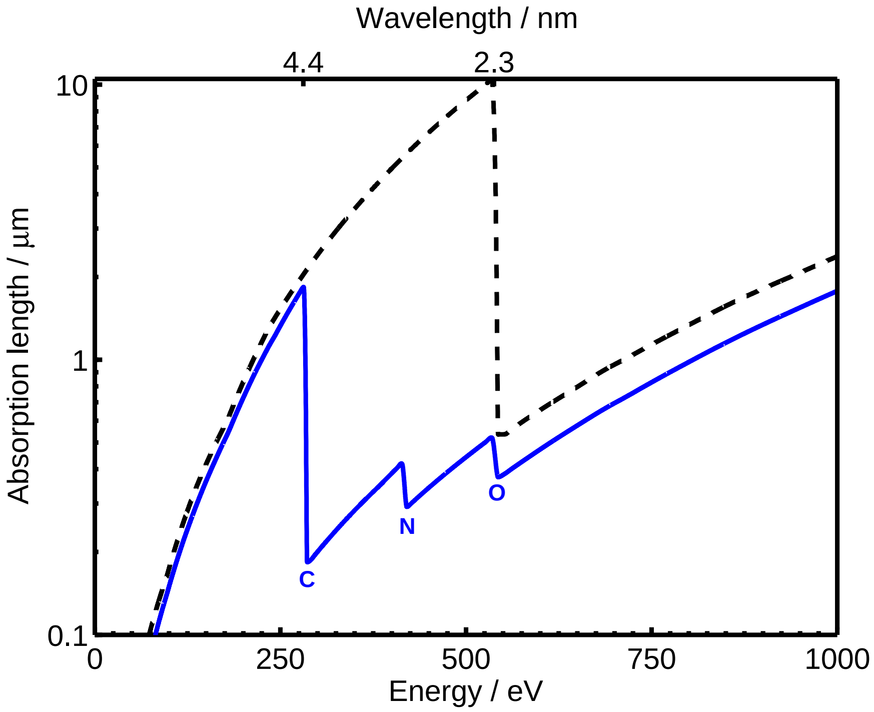

Figure 1.3: The absorption length for XUV in water (dashed line) and majority constituents of a protein sample (solid line), in the region of the water window. Data from reference [14].

to explore the composition of chemically heterogeneous, structured nanomaterials [20] and the distribution of domains in magnetic materials [5,19] where it can also be a sensitive detector of charge and spin [21].

Another promising application for soft X-ray scattering is for probing the shape of large proteins and biological macromolecules. Information on the protein space envelope can be used to improve molecular modelling [22, 23] and the availability of high intensity, femtosecond X-ray sources promises to extend diffractive imaging of non-periodic samples down to the ultimate limit of single molecules [24] and to timescales suitable for probing dynamical structure of the fastest biological processes [25] such as ligand-protein interactions [26], the cis-trans isomerisation of Rhodopsin [27,28] and the femtosecond reorganization of hydrogen bonds in aqueous solutions [29]. Single molecule X-ray scattering removes the need for sample crystallization which is a pre-requisite in current methods which rely on the coherent scattering from a large array of identical molecules in a crystal to achieve detectable signals. Crystallization is a bottleneck in modern protein structure determination [30] which has become increasingly acute with the advent of modern genomic sequencing where the number of identified proteins currently outweighs the number with complete crystal structures [31]. It is expected that single molecule X-ray scattering will improve the throughput of X-ray structure determination for biological materials, such as membrane bound proteins which are currently extremely difficult and time-consuming to crystallize [32] as well as opening up new avenues for materials that are currently impossible to crystallize.

This thesis presents my contribution towards the continuing work in Southampton to build and optimize an XUV source suitable for single molecule X-ray scattering experiments. Chapter 2 examines the driving forces behind single molecule X-ray scattering, discussing the potential rewards that are available and the problems that will need to be negotiated on the way.

The XUV beamline is based on high harmonic generation in a hollow core capillary waveguide and in chapter 3 the theory of high harmonic generation is reviewed, looking in detail at the theory that affects generation in hollow core capillary waveguides, before reviewing the experimental configuration that was designed in chapter 4.

During the development of the high harmonic source, it was discovered that it is possible to tune the wavelength of the harmonic output by taking advantage of the non-linear interaction of the laser pulse with the ionized generating medium. A tuneable source of coherent X-rays is of significant interest for X-ray spectroscopy and resonant soft X-ray scattering experiments and chapter 5 discusses the theoretical basis and experimental results from this work. Chapter 6 discusses spectrally resolved imaging techniques that were developed to understand the role the ionized gas plays in the harmonic generation process as the basis of future work to improve the efficiency and energy characteristics of the harmonic beam.

Single molecule scattering can benefit from a confined X-ray source to increase photon flux and spatial resolution, however focusing X-rays requires different techniques to those commonly employed in the visible because of high material absorption and because the refractive index of materials is less than unity for X-rays. A promising technique is the use of grazing incidence, tapered hollow capillary optics; chapter 7 discusses the theoretical basis of this work and describes the experimental results that were achieved.

Finally, Chapter 8 looks briefly at how this work has placed us for achieving the goal of single molecule scattering and reviews ideas for future experiments.

Chapter 2

Towards Single Molecule X-Ray Scattering

2.1 Introduction

Single molecule spectroscopy has become a routine analytical tool over the past fifteen years, allowing the study of molecular and biological systems beyond the ensemble average, to study transient processes and the dynamics of individual molecules as they interact with their local environment [33]. However, using visible and ultraviolet light, the molecule itself is too small to image directly. Instead, current techniques rely on indirect structural information, for example, by using time-resolved Raman and infrared spectroscopy [26] or by measuring fluorescence resonance energy transfer (FRET) [34, 35] to deduce information about protein conformational changes. This has offered us insight into some of the fastest processes in biology and chemistry which occur on femtosecond timescales. However, none of these spectroscopic techniques are capable of providing the atomic resolution, three-dimensional structural information, that can be provided by X-ray crystallography.

In X-ray crystallography, the scattering from a large array of identical molecules in a periodic sample, such as a crystal, add coherently to form Bragg peaks. By taking the Fourier transform of the resulting diffraction pattern and applying analytical techniques to compensate for the phase information that is lost by the detector, it is possible to reconstruct the electron density, and hence the atomic positions in the crystal at atomic resolution [36]. The formation of Bragg peaks results in an amplification of the diffracted signal of the order of N^2, where N is the number of unit cells in the crystal [37]. This amplification greatly reduces the intensity of the X-ray source required to achieve a detectable diffraction pattern and, for large crystals, allows relatively weak laboratory based X-ray sources, such as rotating anode machines, to be used. However, as the number of readily crystallizable proteins decreases, crystallization has become the major bottleneck in the process, taking many years of painstaking work in some cases [25]. This is especially true in the case of large bio-molecules which can be extremely difficult to crystallize [30] and where it is typically not possible to form large well ordered crystals [38].

The ability to resolve a diffraction pattern depends on a combination of sample size, sample quality and source brightness. Over the last 25 years, research at synchrotron beamlines has reduced the sample size necessary for X-ray crystallography. This has allowed the acquisition of structural data from micron-sized samples [39, 40], since the source brightness compensates for the reduction in scattering signal. In 2004, 76% of all submissions to the Protein Data Bank [41] were based on data measured at synchrotron beamlines [38].

Reducing the size scale further, to perform scattering experiments on single biological macromolecules or other non-crystalline media, is an attractive proposition. This would allow the systematic study of structures of key biological interest which are not amenable to crystallization and hence are not accessible to conventional X-ray crystallography [37]. It has been estimated that $20 - 40\%$ of all protein molecules are difficult or impossible to crystallize [42, 43], including membrane bound proteins, only a handful of which are known, large macromolecules and non-repetitive structures such as cells. The next section briefly discusses why protein structure determination is so important in modern biochemistry and molecular biology. The rest of this chapter considers the key scientific and technical challenges that face single molecule structural determination and discusses the solutions that have been proposed.

2.2 The importance of proteins structures

Proteins are the building blocks of life. These ubiquitous macromolecules occur in all areas of plant and animal biology, performing an enormous variety of functions. They make up the tissues of the human body and the enzymes which catalyze reactions, they transport and store oxygen in the form of globins, form hormones such as insulin and fight disease by forming antibodies [30].

Proteins are polymers built from the standard amino acids. The general form of these α-amino acids is NH_2-CHR-COOH where R represents one of 20 different side chains. These side chains vary considerably in size, shape, charge, hydrogen-bonding or hydrophobic nature and chemical reactivity [44]. The sequence of amino acids forms a protein's primary structure and is dictated by the sequence of base pairs in the genes.

Estimates for the number of protein encoding genes in the Human Genome vary wildly from 25,000 - 100,000 [45, 46] and, with the possibility that genes can code for multiple proteins [46] and post-translational modification can occur [47] then the number of proteins could be significantly greater. As of 2007, more than 38,000 structures exist in the protein data bank [41], but not all of these are unique. Therefore, within human biology alone, there is an enormous challenge to characterize all the possible proteins.

Chemical composition does not go the full way to explaining the functional diversity of proteins. Equally important is the role shape, or conformation plays. Proteins are dynamic molecules and remarkably, they fold to form complex three dimensional structures—a feat that they are predisposed for and which occurs spontaneously, mediated by electrostatic interactions (hydrogen bonding and Van der Waals) and steric considerations between the functional groups within the protein chain and with their environment (i.e., solvent).

Having an accurate three dimensional protein structure is essential in rational drug design, where a protein is isolated and its structure determined to identify active sites. With a knowledge of the size, shape and chemical properties of the protein, potential target molecules can be identified that may be directed to block binding sites or inhibit enzymatic activity and control the biological processes. The development of treatments for the human immunodeficiency virus (HIV) that causes acquired immunodeficiency syndrome (AIDS) exemplifies the rational drug design process. X-ray crystal structures of the HIV-1 protease were used as the starting point for creating inhibitor targets. Structural analysis, in combination with molecular modelling, has lead to a number of successful treatments which deactivate the virus and greatly decreases the mortality rate associated with AIDS [48]. This structure based approach to drug discovery has greatly reduced the time and cost required to bring new drugs onto the market.

X-ray crystallography has been the mainstay of protein structure determination and is responsible for providing 85% of the structures available in the protein data bank [41]. Its popularity is due in part to its capability of providing a greater detail of structural data than spectroscopic techniques, including bond lengths and bond angles [36].

2.3 Radiation damage

X-rays primarily interact with the electrons in matter through elastic scattering and absorption. The elastically scattered photons carry information about the electron distribution in the material while the absorbed X-ray photons can result in radiation induced damage. Experiments on single molecules and other non-crystalline media are limited by the significant radiation damage that occurs to the samples as a result of the very large radiation doses that are required [43] to which biological material is particularly susceptible.

Cooling the sample can help reduce sample damage [49] but during the lengths of exposure necessary to collect data using conventional techniques, the large amount of energy imparted to the molecule by the X-ray beam is sufficient to cause the sample to deteriorate. This can result in movement of the atomic positions, meaning that the longer the exposure time, the less information the final scattering pattern contains about the original structure [24].

Since the photoabsorption cross section of carbon at all wavelengths in the soft and hard X-ray region is much greater than the elastic scattering cross sections (figure 2.3), the photoelectric effect will be the primary damage mechanism [50]. More photons will deposit energy into the sample than will be elastically scattered to give useful structural information. The photons which are absorbed can potentially cause damage through sample heating and ionization [24].

In the photoelectric effect, absorption of a photon results in the emission of an electron in a low-lying orbital; the unstable configuration of the resulting ionized species undergoes relaxation whereby an electron in a higher orbital drops down to fill the hole. In this process, energy is usually lost as a fluorescent X-ray photon in heavy atoms or, in light elements, as an Auger electron, which is usually ejected.

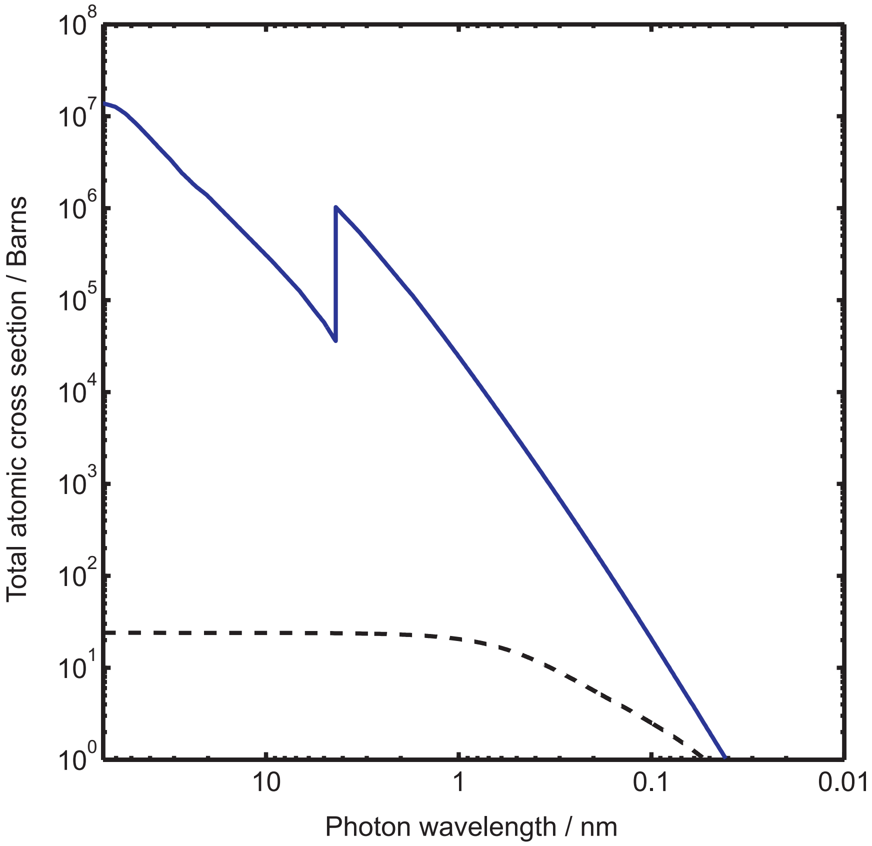

Figure 2.1: The atomic cross sections for carbon for photoabsorption (solid line) and elastic scattering (dashed line) as a function of wavelength. (1 Barn = 10^{-28} m^{-2}) Data from reference [14].

Auger emission dominates (over 95%) for carbon, nitrogen, oxygen and sulphur. Hence, in these elements, absorption of each X-ray photon results in the removal of two electrons. The photoionization of inner shell electrons can result in states where, before the outer shell electrons have time to relax, they can effectively be *unbound* and therefore emitted in an effect called shake-up [50].

Inelastic (Compton) scattering represents another damage mechanism since this results in a direct momentum transfer between the X-ray photon and an electron. In cases where the energy imparted exceeds the electron's binding energy, the electron can be ionized. This effect is most significant for hard X-ray experiments since the Compton scattering cross-sections are very small in the soft X-ray region.

The energetic photoelectrons, Auger and shake-up electrons which are emitted can further interact with the sample when they leave the atom they were emitted from resulting in further damage. Ultimately, ionization results in a build up of positive charge which leads to a Coulomb explosion.

An approach to overcoming the degrading effects of radiation damage, using a short X-ray pulse to record the scattering pattern in a time shorter than the timescale of the damage process, was first suggested by Solem and Baldwin [51]. This is supported by data from a series of molecular dynamics simulations performed by Neutze *et al.* [24] which show that using an ultra-short pulse (< 50 fs) of high intensity X-ray radiation could substantially increase X-ray tolerance and allow the imaging of single biomolecules. This modelling demonstrated that the damage threshold at 1 Å could be increased to around 10^5–10^7 photons per Ångstrom depending on pulse duration compared with only 200 photons per Ångstrom in conventional experiments [49].

2.4 Image reconstruction

In the visible, it is possible to make aberration-free, diffraction limited lenses, allowing imaging with a spatial resolution limited only by the wavelength. At X-ray wavelengths, manufacturing such a lens is technically more demanding and while focal sizes of tens of nanometers have been achieved, atomic-resolution lenses do not seem feasible [52]. Chapter 7 discusses techniques for making X-ray optics in more detail.

It is possible to achieve atomic resolution imaging without lenses by performing the image reconstruction numerically, using a computer—the electron density, and hence atomic positions, being related to the diffraction pattern by the Fourier transform. Consider an image $f(\mathbf{x})$, where $\mathbf{x}$ is a position vector in image space. The Fourier transform $F(\mathbf{k})$ of the image is given by [53]

$$F(\mathbf{k}) = \int_{-\infty}^{\infty} f(\mathbf{x}) \exp(i2\pi\mathbf{k}\cdot\mathbf{x})dx, \tag{2.1}$$

where $\mathbf{k}$ is the position vector in Fourier space. In practice, since the diffraction pattern is projected onto a camera composed of a grid of N pixels of finite size, we instead use the discrete Fourier transform [18]

$$F(\mathbf{k}) = \sum_{x=0}^{N-1} f(\mathbf{x}) \exp(i2\pi\mathbf{k}\cdot\mathbf{x}/N), \tag{2.2}$$

where $\mathbf{x}$ and $\mathbf{k}$ are discretized and represent pixels that range in each dimension from 0 to $(N-1)$. Since $F(\mathbf{k})$ is complex, the correct image will be obtained by inverse Fourier transform of the diffraction pattern

$$f(\mathbf{x}) = \sum_{x=0}^{N-1} F(\mathbf{k}) \exp(-i2\pi\mathbf{x}\cdot\mathbf{k}/N), \tag{2.3}$$

if the magnitude and phases are known and the Fourier transform is sampled at a frequency at least equal to the Nyquist frequency [54]. Where the amplitude and phases are known, the Nyquist frequency is the minimum sampling frequency required for the correct inversion of the Fourier transform [54]. Since only $|F(\mathbf{k})|^2$ can be measured experimentally, the data corresponds to [55]

$$|F(\mathbf{k})| = \left|\sum_{x=0}^{N-1} f(\mathbf{x}) \exp(i2\pi\mathbf{k}\cdot\mathbf{x}/N)\right|. \tag{2.4}$$

There exists a set of N-equations of the form given by equation 2.4 and the solution of the phase problem involves solving each of these equations for $f(\mathbf{x})$, for each pixel element in $F(\mathbf{k})$.

For a one-dimensional object composed of N pixels, where $f(\mathbf{x})$ is complex, there are N equations of the form given by equation 2.4 whereas there are $2N$ unknowns because $f(\mathbf{x})$ has both real and imaginary components. For complex-valued objects in two- and three-dimensions, the total number of equations is N^2 and N^3 respectively, while the total number of unknown variables is $2N^2$ and $2N^3$ respectively. When $f(\mathbf{x})$ is real, the number of unknown variables reduces to N, whereas the number of independent equations also goes down to $N/2$ because the magnitude of the Fourier transform $|F(\mathbf{k})|$ has central symmetry [42]. By extension to two- and three-dimensional real objects, the total number of equations is $N^2/2$ and $N^3/2$, respectively, and the total number of unknown variables is N^2 and N^3 respectively. In a crystal, the diffracted intensity is concentrated in discrete Bragg peaks which imposes a limit on the sampling rate of its Fourier transform. The result of this is that the phase problem for a crystal sampled at Bragg density is under-determined by a factor of two; equation 2.4 cannot be solved without additional information and the phase is not unique [55]. In X-ray crystallography, a variety of methods, such as the direct method [53], have been developed for solving the phase problem. The direct method involves applying atomicity and positivity constraints to equation 2.4 to greatly reduce the number of unknown variables.

When the specimen is non-crystalline, the diffraction pattern is continuous and no longer exhibits Bragg peaks. This changes the nature of the phase retrieval problem since it is possible to sample the Fourier transform at a frequency greater than the Nyquist frequency. This increases the number of independent equations for the same number of unknown variables [43]. The oversampling ratio α is given by [55]

$$\alpha = \frac{\text{volume of electron density region} + \text{volume of no-density region}}{\text{volume of electron density region}}, \tag{2.5}$$

where the volume of the region represents the total grid points inside the region. Miao and Sayre have shown [54, 55] that for $\alpha > 2$, the number of independent equations exceeds the number of unknown variables and, in principal, the phase information can be retrieved from the diffraction pattern using an iterative algorithm.

The oversampling technique is best illustrated by an example. Figure 2.2(b) shows an object and figure 2.2(a) its diffraction pattern. Sampling the diffraction pattern at the Nyquist frequency produces an $N \times N$ array which is inverted on a computer, using the fast Fourier transform (FFT) technique to give an $N \times N$ array where the object fills the array. Figure 2.2(c) shows the diffraction pattern of the same object sampled at twice the Nyquist frequency, resulting in $2N \times 2N$ array. The inverse fourier transform of the diffraction pattern, shown in figure 2.2(d), gives a $2N \times 2N$ array where the object occupies the same $N \times N$ area as before, but is now surrounded by a zero-density region which is used to drive the phase retrieval process.

Phase retrieval is a non-linear optimization problem in a multi-dimensional phase space, the dimensionality being equal to the number of phases to be retrieved. In principal there exists a unique phase solution in an oversampled two- and three-dimensional diffraction pattern [56], the challenge is to find it from the large number of non-linear equations involved. The majority of algorithms are based on an iterative transform algorithm (ITA), which cycles between image and Fourier space, respectively enforcing constraints of known object support and known diffraction modulus. Most of these algorithms are descendants of the Gerchberg-Saxton error-reduction algorithm [17], or Fienup's hybrid input-output method [18].

Figure 2.3 illustrates the general concept of phase retrieval using a hybrid input-output (HIO) type algorithm. In the HIO procedure, constraints are iteratively applied in image and Fourier space, and a feedback param-

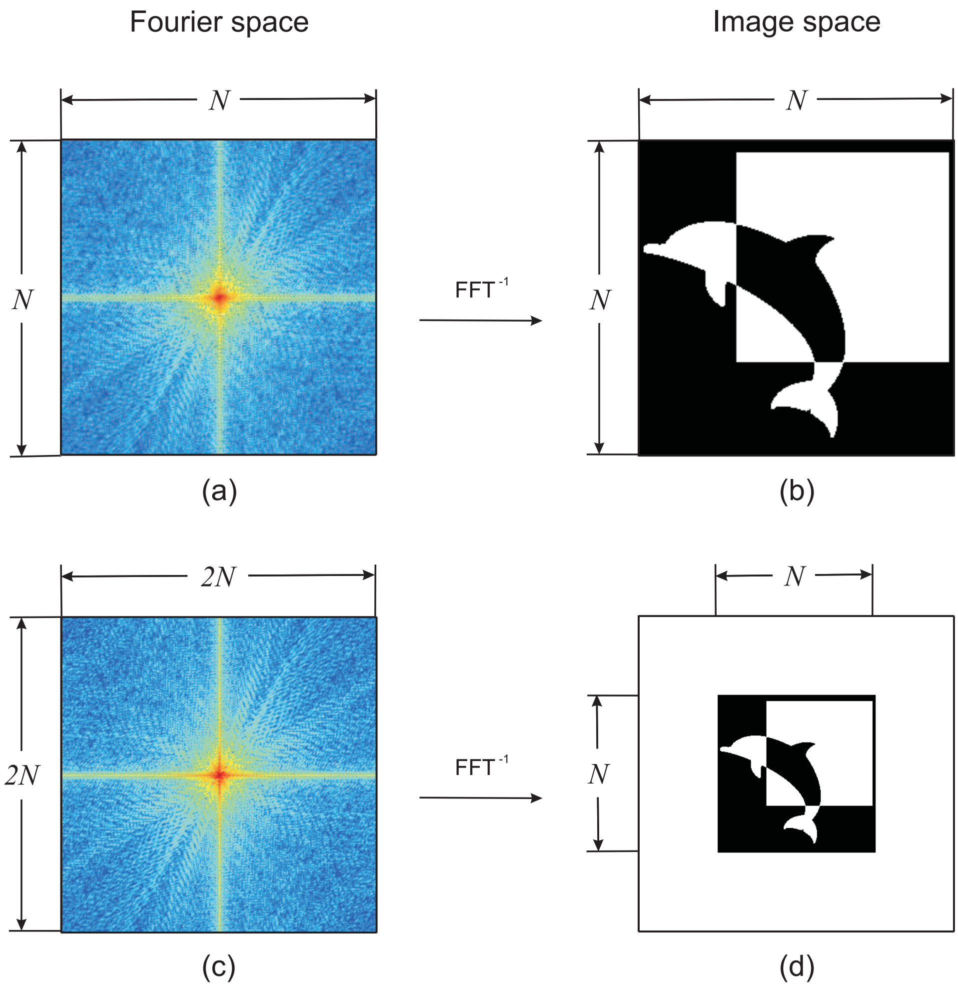

Figure 2.2: (a) The diffraction pattern of an object is sampled at the Nyquist frequency and (b) the inverse Fourier transform gives the reconstructed image which fills the resulting array. (c) The diffraction pattern is oversampled at twice the Nyquist frequency and (d) the inverse Fourier transform gives the reconstructed object which is now surrounded by an area of zero-density, which can be used in phase retrieval.

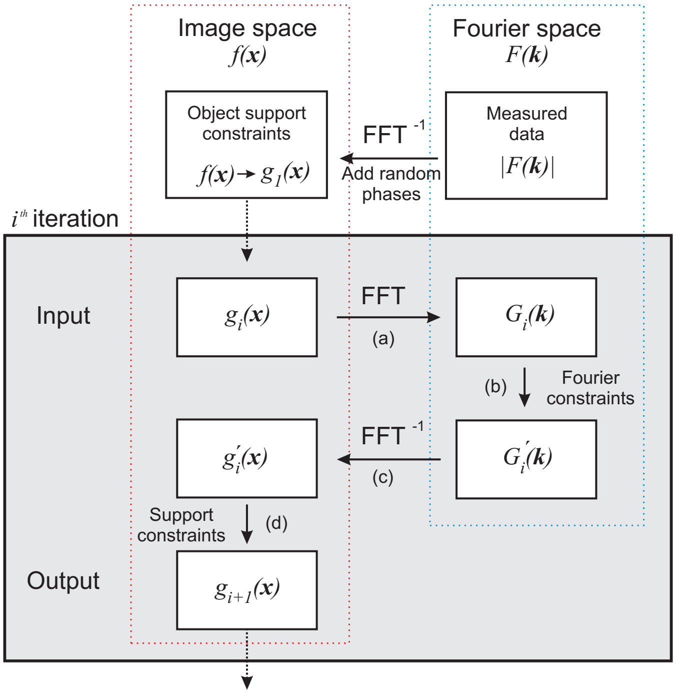

Figure 2.3: A schematic representation of the hybrid input-output (HIO) algorithm for iterative phase retrieval.

eter is applied in image space to damp the effect of the support constraints which allows the algorithm to climb out of local minima. The process begins with a measured, oversampled diffraction pattern $|F(\mathbf{k})|$, shown in figure 2.4(a), to which random phases are added. This is inverse Fourier transformed to give a initial estimate of the object $f(\mathbf{x})$, shown in figure 2.4(b). For this object, we define a mask to separate the electron density and no-density regions based on an initial estimate of the envelope of the object, called the support. This envelope can be selected, for example, from a low-resolution optical or electron micrograph of the image [37]. This object is used as the basis of the first iteration step $g_1(\mathbf{x})$ in the input-output algorithm.

The input image $g_i(\mathbf{x})$ is Fourier transformed, as shown in figure 2.3(c), to give a diffraction pattern $G_i(\mathbf{k})$. In figure 2.3(d), the Fourier constraints are applied to give $G_i'(\mathbf{k})$, taking the phase information present in $G_i(\mathbf{k})$ and replacing the magnitude with that from $|F(\mathbf{k})|$. $G_i'(\mathbf{k})$ is inverse Fourier transformed to give the new object $g_i'(\mathbf{x})$, shown in figure 2.3(e). Object support constraints are enforced on the real space image in figure 2.3(f), driving the electron density outside the support to zero using the equation

$$g_{i+1}(\mathbf{x}) = g_i(\mathbf{x}) - \beta g_i'(\mathbf{x}), \qquad \mathbf{x} \notin S \tag{2.6}$$

where S represents the region inside the object support and β is a constant.

Miao and Sayre [54, 55] have developed an iterative algorithm for retrieving the phase from oversampled scattering patterns and Miao has used this technique to retrieve images of nanostructured gold samples [40, 57] and single particles of the *Escherichia coli* bacteria [58] from experimental scattering data.

To illustrate the concept of phase retrieval, which will be a necessary step in the reconstruction of structural information from X-ray scattering data, I have written an iterative transfer algorithm in Matlab®. The al-

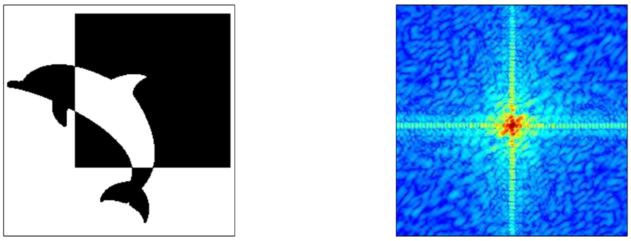

(a) (b)

Figure 2.4: (a) Real space object and (b) intensity of the simulated oversampled scattering pattern, shown on a logarithmic scale.

gorithm is based on the HIO method described above, with the addition of a support refinement step which was recently developed by Marchesini *et al.*, called Shrinkwrap [59]. The Shrinkwrap algorithm does not require *a priori* knowledge of the shape of the object. This is advantageous since it has been shown that the quality of the support affects the quality of the retrieved image [60]. In the first iteration, the autocorrelation function is used as an estimate of the object support. This is not particularly accurate but guarantees that the object will fit within the support. As the algorithm develops, the support is continually updated by thresholding the intensity of a blurred version of the current object. By thresholding, the envelope of the object is traced at a given intensity contour and a gaussian blurring function is applied to smooth out noise and, if necessary, expand the area of the support. The algorithm is very stable, successfully converging to the correct support and object, and has been used for the successful reconstruction of experimental X-ray diffraction patterns [59,61,62].

The algorithm was tested with the simulated oversampled diffraction data shown in figure 2.4(b), which was created by taking the squared magnitude of the Fourier transform of the 64×64 pixel object shown in figure 2.4(a), using the Fast Fourier Transform (FFT) method. The diffraction pattern is oversampled by a factor $\alpha = 4$ by surrounding the object with a zero density border, as described in figure 2.2. The algorithm starts from the autocorrelation function, obtained by taking the Fourier transform of the diffraction pattern and an initial estimate for the support mask is obtained by thresholding the autocorrelation function at the 3% intensity level. The HIO algorithm is applied, as described above, with a feedback parameter $\beta = 0.9$. Every 20 iterations, we apply a support refinement step by gaussian blurring and thresholding the current estimate of the reconstructed image. This is done by convolving the current image with a Gaussian of width σ. The new mask, which will be used in subsequent iterations, is then created by applying a threshold at the 20% level. The width σ is set initially to 3 pixels and reduced by 3% every time the Shrinkwrap step is applied down to a minimum of 1 pixel. These parameters have been refined to improve the speed of convergence of the algorithm for this dataset. Figure 2.5 shows the progress of the algorithm and mask after 1, 10, 100 and 500 iterations of the algorithm, showing the progressive refinement of the mask and retrieved object. After 500 iterations, the final support is obtained (figure 2.5(j)) and further refinement of the object is achieved by performing 500 iterations of the HIO algorithm starting from random phases, with a feedback parameter $\beta = 0.9$. The complete phase retrieval of the object from the 128×128 pixel diffraction data took 37 seconds on a single-processor, 1.7 GHz Intel® Centrino® system with 512 MB of memory.

The progress of the retrieval algorithm can be monitored by measuring the real-space error [18]

$$E^2 = \sum_{x \notin S} [g'(\mathbf{x})]^2, \tag{2.7}$$

where S is the support and $g'(\mathbf{x})$ as defined in figure 2.3 is the current estimate of the real space object. The error E for the phase retrieval shown in figures 2.5(a-h) is shown in figure 2.6.

Another example of particular interest is phase retrieval from a complex

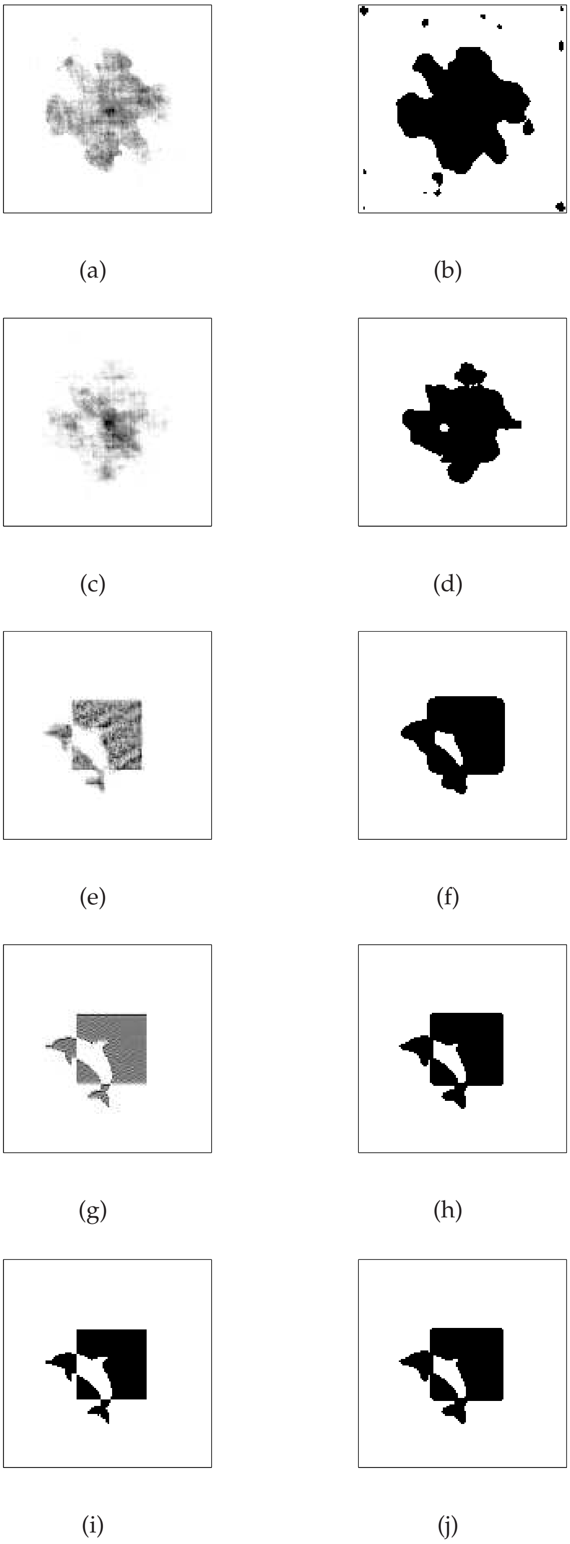

Figure 2.5: Progress of the reconstruction algorithm showing (a) the retrieved object and (b) mask after 1 iteration, (c-d) 10 iterations, (e–f) 100 iterations and (g-h) 500 iterations of the HIO algorithm with support refinement by the Shrinkwrap technique. (i) Retrieved object after refinement with 500 iterations of the HIO algorithm using (j) as the final support.

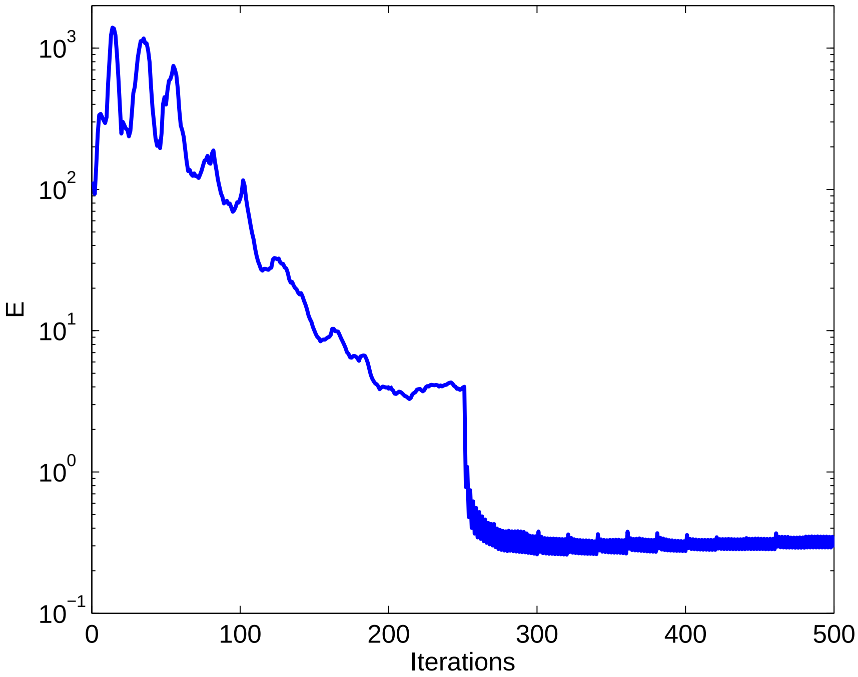

Figure 2.6: Error as a function of number of iterations for the image reconstruction illustrated in figure2.5(a–h).

valued object which can occur, for example, when the object is not illuminated by a plane-wave [59]. This has proved to be a challenging problem, however, it has been shown that it is possible given a sufficiently tight support [60]. The adaptive support refinement in the Shrinkwrap algorithm [59] satisfies this requirement, making the algorithm highly successful at the retrieval of complex valued object. Figure 2.7(a) illustrates the phase of a complex valued objects. Using 1500 iterations of the HIO algorithm with a support refinement step every 20 iterations as described above, a very tight support was formed. Figure 2.7(b) illustrates the reconstructed phase profile which, with the exception of the arbitrary phase shift which occurs, shows perfect agreement with the original object. The phase shift, and other ambiguities about the absolute position and inversion about the origin can occur because $f(\mathbf{x})$, $f(\mathbf{x}+\xi_1)\exp(i\phi_1)$, and $f^*(-\mathbf{x}+\xi_2)\exp(i\phi_2)$, all give rise to the same value for $|F(\mathbf{k})|$, where ξ_1, ξ_2, ϕ_1 and ϕ_2 are real constants [53, 55].

(a) (b)

Figure 2.7: (a) The phase component of a complex valued object and (b) the reconstruction of this phase profile. Aside from the arbitrary phase shift which occurs, a perfect reconstruction of the phase profile is possible.

2.5 Conceptual experiment

In an intense, focused X-ray beam, no biological sample is likely to survive more than one X-ray pulse. However, to form three-dimensional images requires more than one view of the sample. With repeatable samples, a full three-dimensional data set may be constructed from the diffraction patterns of identical molecules in random orientations. Figure 2.8 shows a schematic representation of such an experiment. A stream of identical molecules is inserted into the X-ray beam using mass spectroscopic sample selection and injection techniques [43, 50, 63]. The arrival time of the molecule is carefully synchronized with the X-ray pulses. Unlike the use of a solid support, such as holding the sample on a silicon nitride membrane, this technique ensures the particle is the only scattering object in the beam. The resulting scattering pattern is recorded on a charge-coupled device (CCD) detector.

The multiple patterns that are recorded can be sorted and classified to

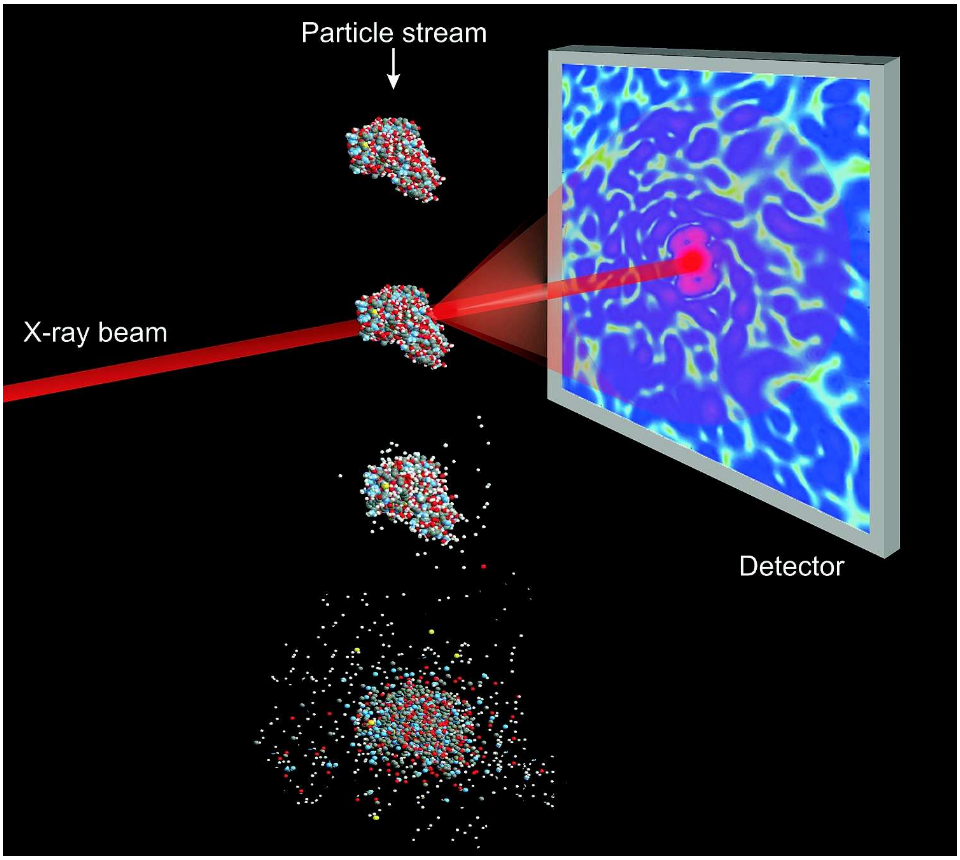

Figure 2.8: Schematic representation of a single molecule X-ray scattering experiment. The intensity pattern formed when an intense X-ray pulse scatters from the particle is recorded by a charge-coupled device (CCD) detector. A stream of single molecules are injected into the beam; their arrival time is synchronised to coincide with the arrival of the X-ray pulse. The intense X-ray pulse ionizes the molecule, ultimately leading to Coulomb explosion and allowing only a single diffraction pattern to be recorded from each molecule. (Protein molecules taken from reference [24] and diffraction pattern adapted from [64].)

group like orientations together, averaging the images within each group to improve signal-to-noise which may be insufficient to produce high resolution data from a single X-ray shot [65]. In cryoelectron microscopy, cross-correlation techniques have been developed to sort individual images into groups based on similar orientations [64]. After classification and averaging, the relative orientation of each image can be determined to produce a three-dimensional map of Fourier space [65]. The phase retrieval techniques described in section 2.4 can then be applied in three-dimensions to recreate the three-dimensional electron density of the sample.

A recent experiment performed by Chapman *et al.* at the FLASH soft X-ray free-electron laser demonstrated single-shot imaging of a nanoscale, non-period object. An intense 25 fs pulse, containing 10^{12} photons at 30 nm was capable of producing a single-shot diffraction pattern before destroying the sample. The image was reconstructed using the over-sampling phase retrieval method and importantly, shows no measurable sign of radiation induced damage [61]. This experiment gives an estimate of the number of photons required from a high harmonic source for a single-shot diffraction experiment and recently, Hergott *et al.* demonstrated a high harmonic source capable of producing $> 10^{11}$ photons per pulses at 53 nm by loosely focusing high energy 60 fs 25 mJ pulses into a Xenon gas jet [66].

2.6 Summary

In this chapter, we have reviewed the key aims of single molecule X-ray scattering and discussed the challenges presented by radiation damage caused by irradiating the sample with with intense X-rays. This can be mitigated by using a femtosecond X-ray source and in the next chapter, we look at the theory behind high harmonic generation, the technique we will use to generate femtosecond XUV pulses.

Chapter 3

High Harmonic Generation

3.1 Introduction

In high harmonic generation, the extreme non-linear optical response of a medium to an intense laser field ($> 10^{13}$ W cm^{-2}) results in a proportion of the incident laser being converted to higher frequencies. These harmonic frequencies ν_q are an integer multiple q of the fundamental frequency ν_0,

$$\nu_q = q\nu_0, \tag{3.1}$$

where q is the harmonic number [67]. In the first reports of high harmonic generation [68,69] it was noticed that the harmonic spectrum, shown schematically in figure 3.1, consists of three characteristic regions: perturbative, plateau and cut-off. The *perturbative region* corresponds to those harmonic orders where the intensity is observed to decrease rapidly and is so-called because this behavior can be explained in terms of perturbation theory [70]. For the higher orders, a *plateau* region of equally intense harmonics is observed which extends up to the *cut-off* as the maximum frequency is reached. It is not possible to explain the behavior of the high order harmonics and plateau region in terms of perturbation theory which

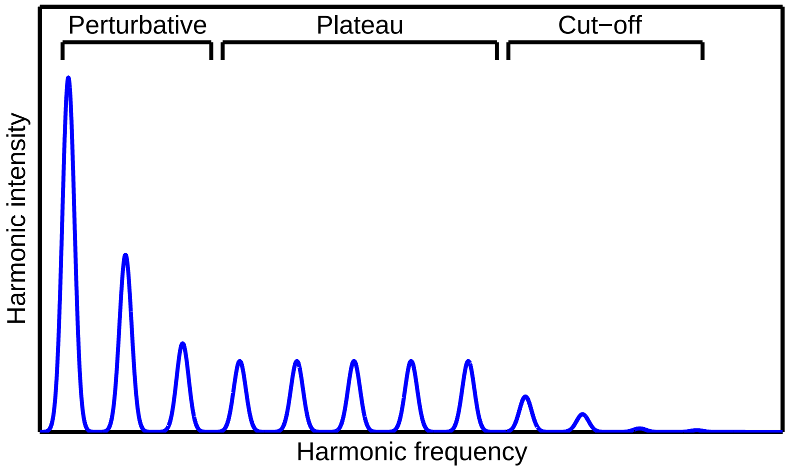

Figure 3.1: Schematic high harmonic spectrum showing the typical features. There is a rapid decrease in intensity over the first few orders followed by a plateau region of constant intensity which is terminated by a cut-off, the highest harmonics that are generated.

predicts that efficiency decreases with increasing harmonic order [4].

3.2 Single-atom response

For a full understanding of all the features of the experimentally observed high harmonic spectrum, it is necessary to use the quantum mechanical models discussed in section 3.2.4. However, many of the features can be understood in terms of a simpler semi-classical model of the single atom response to the intense field which was developed by Corkum [71]. In this three-step model, which is summarized in figure 3.2, the electron is first ionized. It is then free to propagate as a classical particle under the influence of the oscillating laser field. When the laser field changes sign, the electron will be accelerated back towards the parent ion before finally, the electron recombines. The kinetic energy that the electron has acquired plus the ionization potential of the atom is given up as a high energy photon

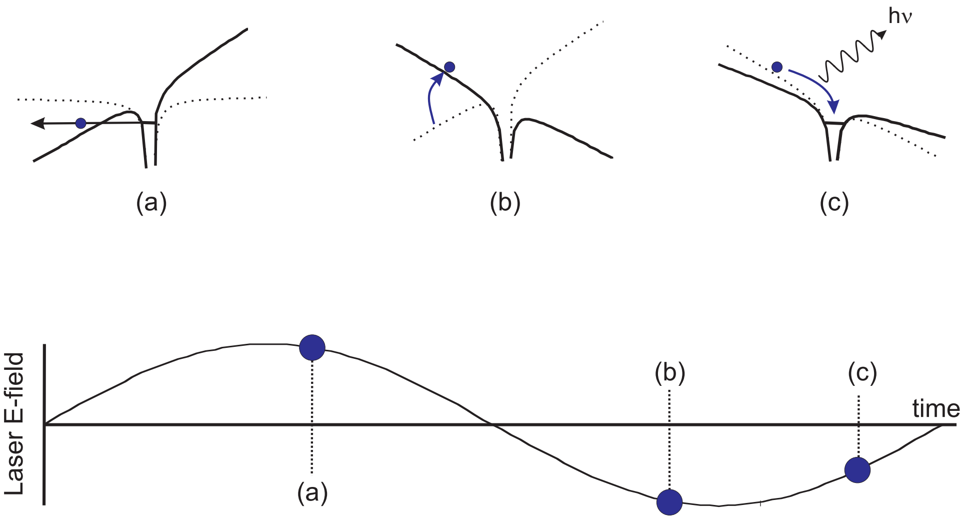

Figure 3.2: The three-step model. (a) The electron is ionized and (b) the free-electron is driven away from the parent ion. (c) After the sign of the electric field reverses, the electron may be accelerated back to recombine with the parent ion to emit a photon with energy equal to the kinetic energy of the electron plus its ionization potential.

when the electron recombines. Each of these steps is discussed in detail in the following section.

3.2.1 Ionization

There are three ionization regimes for an atom in a strong laser field. At modest intensities, multiphoton ionization (MPI) occurs by the absorption of multiple photons via intermediate states (figure 3.3(a)). As the field stren-gth increases, the electric field $\mathbf{E}(t)$ of the laser will produce a potential $e\mathbf{E}(t)\mathbf{r}$ that is sufficient to significantly distort the Coulomb potential

$$V(\mathbf{r},t) = -\frac{e^2}{4\pi\epsilon_0 r} + e\mathbf{E}(t)\mathbf{r}, \tag{3.2}$$

where e is the charge on the electron, ϵ_0 is the permittivity of free space and $\mathbf{r}$ is a position vector [4]. This distortion (figure 3.3(b)) forms a potential

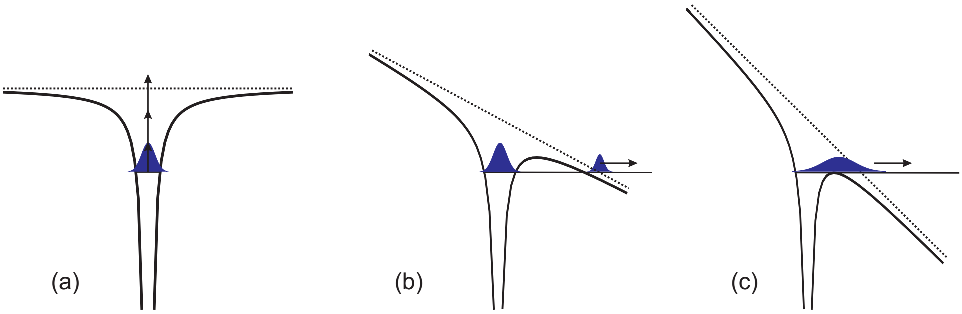

Figure 3.3: The three possible mechanisms for ionization. (a) Multi-photon ionization dominates at lower intensities. (b) As the intensity is increased, the atomic potential is distorted and tunnel ionization is possible. (c) At even higher intensities, the potential barrier is suppressed and over the barrier ionization occurs.

barrier through which the electron can escape by tunneling [72]. As the electric field strength is increased further, the barrier becomes suppressed to such an extent that the electron can pass over the top of it (figure 3.3(c)). This process is called over the barrier ionization (OTBI) and occurs for intensities given by [73]

$$I_c = 4 \times 10^9 (I_p^4 Z^2), \tag{3.3}$$

where I_c is expressed in W cm^{-2}, Z is the residual charge on the ion after ionization and I_p is the ionization potential in electron volts. For neutral argon, where $I_p = 15.76$ eV [74] and $Z = 1$, the threshold for OTBI is 2.5×10^{14} W cm^{-2}.

The mechanism of tunnel ionization has been extensively studied, with the theory originating from the work of Keldysh. A comprehensive review of the development of this work was given recently by Popov [74], which gives an expression for the rate of tunnel ionization

$$w = \kappa^2 C_{\kappa l}^2 \sqrt{\frac{3}{\pi}}(2l+1)\frac{(l+m)!}{2^m m!(l-m)!} 2^{2n^*-m} F^{m+1.5-2n^*} \exp\left[-\frac{2}{3F}\left(1-\frac{1}{10}\gamma^2\right)\right], \quad (3.4)$$

where w is given in the atomic unit of frequency, 4.13×10^{16} s^{-1}, l and m are the angular momentum and magnetic quantum numbers of the atom respectively, $C_{\kappa l}$ is the dimensionless asymptotic coefficient of the atom wavefunction away from the nucleus (values for common atoms and ions are given in [74]) and κ, the principle quantum number n^* and the reduced field F are given by

$$\kappa = \sqrt{\frac{I_p}{I_H}} \quad (3.5)$$

$$n^* = \frac{Z}{\sqrt{2I_p}} \quad (3.6)$$

$$F = \frac{E}{\kappa^3 E_a}, \quad (3.7)$$

where I_p is the ionization potential for the atom, $E_a = 5.14 \times 10^9$ V cm^{-1} is the atomic unit of electric field intensity, $I_H = 13.6$ eV is the ionization potential of hydrogen and E is the amplitude of the laser electric field given in atomic units. The Keldysh parameter γ is given by

$$\gamma = \frac{1}{2K_0 F}, \quad (3.8)$$

where $K_0 = I_p/\hbar\omega$ is the number of photons required for MPI. The Kelydsh parameter determines whether the atom is ionized in the tunneling ($\gamma \ll 1$) or multiphoton regime ($\gamma \gg 1$) [74].

Given an unchirped sinusoidal pulse of frequency ω_0 we can calculate an instantaneous value of the electric field E as a function of time t through

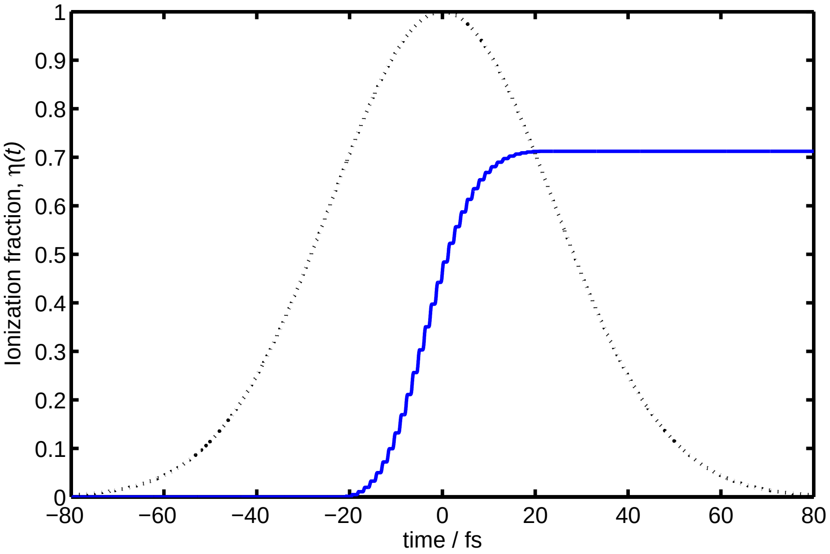

Figure 3.4: Ionization fraction η (solid line) of argon as a function of time t for a 40 fs laser pulse (dashed line) with a peak intensity of 3×10^{14} W cm^{-2}.

the pulse from

$$E(t) = E_0 \cdot \Re \left\{ \exp \left[-2ln2 \left(\frac{t}{\tau} \right)^2 \right] \exp(i\omega_0 t) \right\}, \tag{3.9}$$

where E_0 is the peak field and τ is the full width at half maximum of the intensity of the gaussian temporal profile. Equations 3.4 and 3.9 can then be used to calculate the ionization rate $w(t)$ through the oscillating laser field which can be converted to an ionization fraction $\eta(t)$ by

$$\eta(t) = 1 - \int_0^t N_a(t')\omega(t')dt', \tag{3.10}$$

where N_a is the number of neutral atoms. Figure 3.4 shows an example of the ionization fraction as a function of time during a 40 fs pulse. The ionization is calculated over each time step and the total ionization integrated to give the ionization level at any time within the pulse [75].

3.2.2 Propagation

After the electron is ionized, it can be considered to be a free electron whose motion is governed only by the laser field [71]. The force that the electron experiences will be proportional to the laser electric field $E(t) = E_0 \sin(\omega t)$. By integrating the classical equations of motion, a classical position $x(t)$ and velocity $v(t)$ can be obtained for the electron as a function of time [76]:

$$v(t) = -v_o(\cos(\omega t) + v_0 \cos(\omega t')), \tag{3.11}$$

$$x(t) = \frac{1}{\omega}(-v_0 \sin(\omega t) + v_0 \sin(\omega t')) + (t - t_0)v_0 \cos(\omega_t'), \tag{3.12}$$

where $v_0 = E_0 e/m\omega$. It is assumed that the electron escapes at time t' with initial position $x(t') = 0$ at velocity $v(t') = 0$.

Depending on the time t' that the electron enters the continuum, it may follow a number of different trajectories. For HHG to occur, the electron must be accelerated away from the nucleus and then return to its original position, $x = 0$, to recombine and emit an XUV photon. Figure 3.5 shows a number of possible trajectories for electrons emitted at different times through the optical cycle. Electrons emitted while the field is growing in absolute value ($0 < t/\tau < 0.25$) are accelerated away from the core and will never return and therefore these trajectories do not contribute to the harmonic emission (trajectory (a) in figure 3.5). If the electron is released at the peak of the field ($t/\tau = 0.25$) it returns to its parent ion with zero kinetic energy (trajectory (b) in figure 3.5). Electrons that are emitted when the field is decreasing in absolute value ($0.25 < t/\tau < 0.5$) recombine with a higher kinetic energy and spend a shorter time in the continuum. Finally, electrons emitted when the field is close to zero ($t/\tau \sim 0.5$) spend a very short time in the continuum and acquire a small amount of kinetic energy.

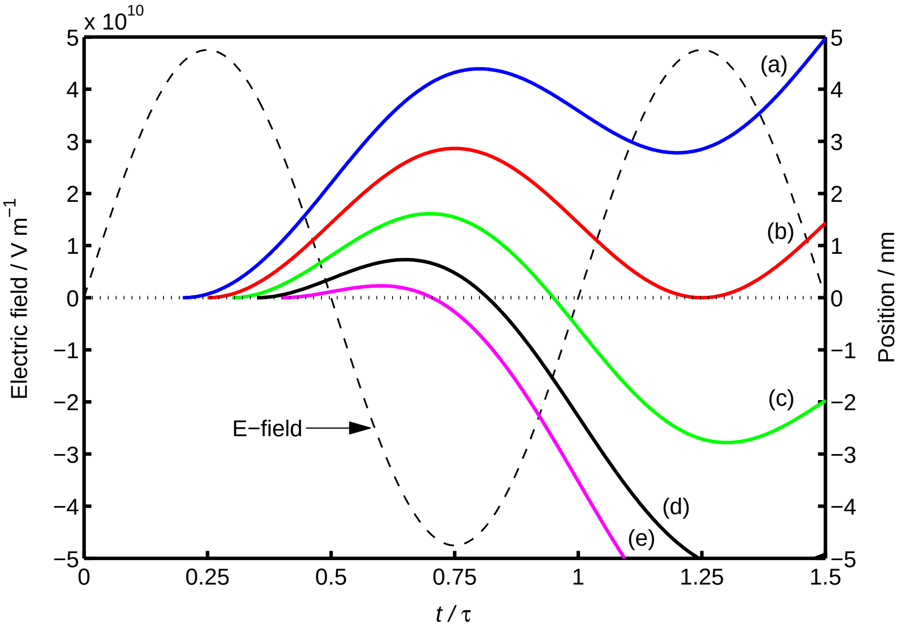

Figure 3.5: The electron trajectories in the continuum corresponding to different release times t during the optical cycle of period τ. An electron emitted at (a) $t/\tau = 0.2$ represents an electron that is accelerated from the core and does not contribute to harmonic generation, (b) at $t/\tau = 0.25$ the electron returns with zero kinetic energy and at $t/\tau =$(c) 0.3, (d) 0.35 and (e) 0.4 the electron has varying return kinetic energy.

3.2.3 Recombination

When an electron recombines with its parent ion, a photon is emitted with energy equal to

$$\hbar\omega = E_{\mathrm{KE}} + I_p, \tag{3.13}$$

where E_{KE} is the kinetic energy the electron acquired in the laser field and I_p is the ionization potential. As discussed in the previous section and shown in figure 3.5, the slope of the trajectory at $x = 0$ when the electron re-encounters the ion assumes different values corresponding to different velocities and therefore different kinetic energies. Solving equation 3.12 for $x(t) = 0$ numerically, it is possible to calculate the kinetic energy as a function of release time (figure 3.6) and determine that the maximum ki-

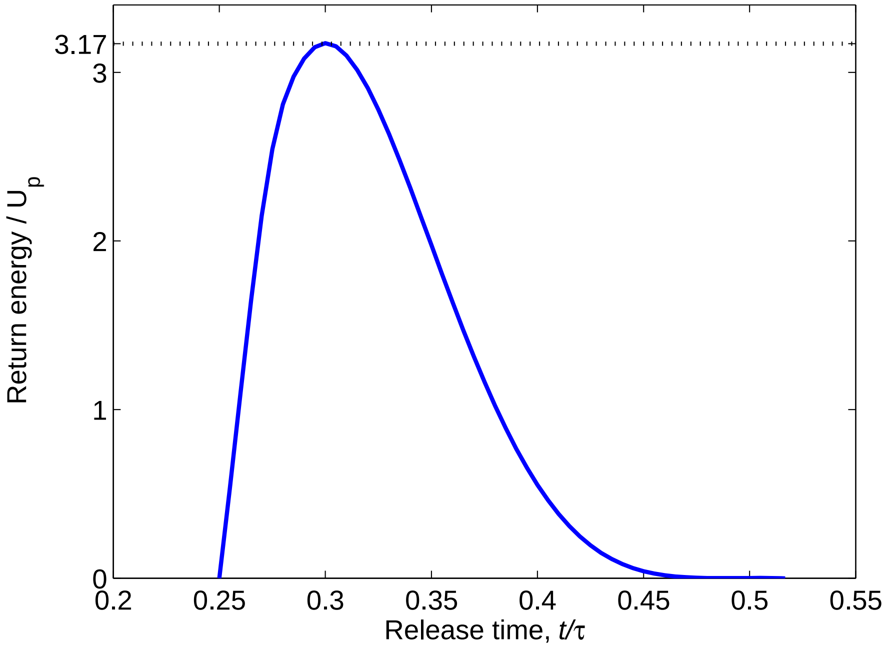

Figure 3.6: Return kinetic energy of the electron expressed in units of the ponderomotive energy U_p as a function of the release time t/τ.

netic energy the electron may acquire is given by $\sim 3.17U_p$, where U_p is the ponderomotive energy,

$$U_p = \frac{e^2E_0^2}{4\omega^2 m_e^2}, \tag{3.14}$$

which is the average kinetic energy of an electron oscillating in an electromagnetic field of amplitude E_0 and angular frequency ω.

The maximum kinetic energy that the electron can acquire corresponds to the maximum photon energy E_c which can be generated and therefore we expect the high harmonic spectrum to be cut-off at photon energies higher than [71]

$$E_c = I_p + 3.17U_p. \tag{3.15}$$

According to this classical picture, the highest possible harmonic or-

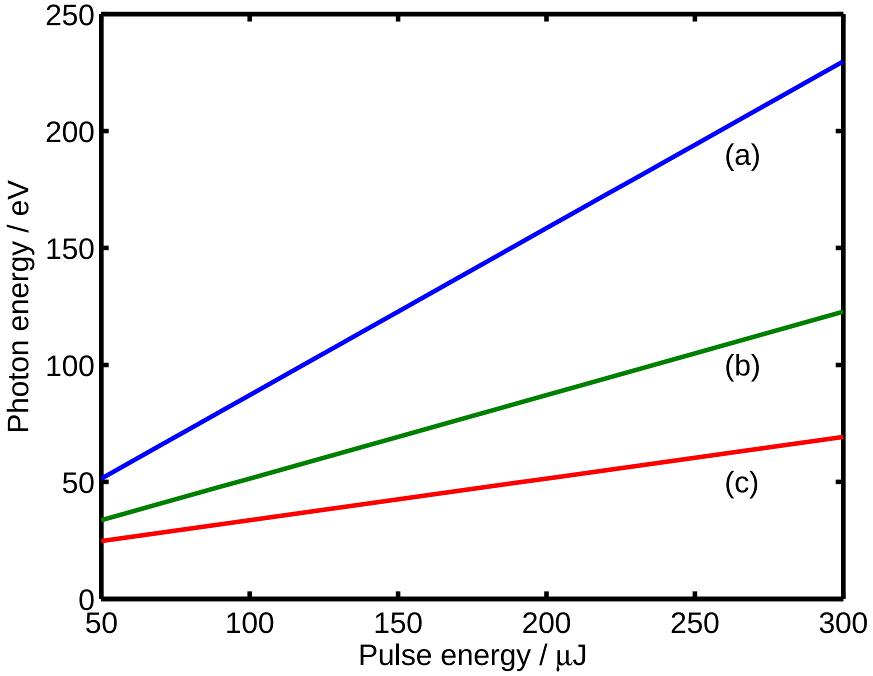

Figure 3.7: The highest photon energy achievable in argon for laser pulses of wavelength 780 nm and pulse lengths (a) 10 fs, (b) 20 fs and (c) 40 fs focused into a 75 μm radius capillary. Shorter pulses and higher energies push the cut-off to increase the maximum harmonic order.

der that can be achieved will be a function of the ionization potential of the gas medium and the wavelength, pulse width and pulse energy of the laser. Figure 3.7 illustrates the highest photon energy that can be achieved in neutral argon. It is clear that by increasing the pulse energy or decreasing the pulse length, the cut-off will be shifted to higher energy. The highest photon energy achievable in neutral atoms is ultimately limited by the saturation intensity, hence the harmonic cut-off may be increased by choosing a generating gas with a large ionization potential, such as helium [77], or using ions [78,79]. As such, neutral atoms, molecules and ions when illuminated with laser intensities of $10^{13} - 10^{16}$ W cm^{-2} can emit high harmonics in the range of tens to several hundreds of electron volts. The highest energy that has been generated to-date is 1.3 keV, demonstrated by focusing a few-cycle pump pulse with a peak intensity of 1.4×10^{16} W cm^{-2} into a helium gas jet [10].

So far, this discussion has not considered why the harmonic peaks exist at odd integer multiples of the fundamental frequency, f. This can now be understood by considering the temporal structure of the harmonic emission which repeats every half cycle $T/2$ of the laser field. As a result, the Fourier transform of the time-domain signal will have a frequency separation $1/(T/2) = 2f$. In a medium that possesses inversion symmetry, such as the gases commonly used for harmonic generation, the induced polarization is an odd function of the electric field, repeating every half-cycle of the laser field but with a change of direction, hence only odd harmonics are formed.

In section 3.3 this simple single atom picture is extended to incorporate macroscopic effects, including phase-matching and absorption and it will be seen that propagation effects can impact upon the harmonic emission that is observed.

3.2.4 Quantum model

In the previous section, it has been demonstrated that much of the high harmonic generation process, including the overall range of photon energies generated can be understood in terms of the semi-classical three-step model. However, for a more complete picture, a fully quantum mechanical treatment is required. In a quantum model, as the laser field strength increases, part of the electron wave function tunnels from the atomic potential and propagates in free space away from the atom. As the sign of the laser field reverses, the extended electron wavefunction re-encounters the part of the wavefunction still in the ground state of the atom. The part of the wavefunction that propagates in the laser field is phase shifted relative to the ground-state wavefunction, resulting in an oscillating dipole. By taking the Fourier transform of this time domain signal, the harmonic spectrum can be recovered. A quantum-mechanical formulation of the three-step model has been developed by Lewenstein *et al.* [80] which successfully explains the characteristics of harmonic generation, such as the photon energy cutoff, as well as offering insight into the spectral characteristics and divergence properties of the beam. The remarkable success of the semi-classical three-step model can be explained by the fact that the classical trajectories correspond to those trajectories in the quantum mechanical model which add constructively [81]). Many of the properties of the harmonic emission are related to the phase of the electron, which is given by [82]

$$\Phi = q\omega t_f - S(p_{st}, t_i, t_f)/\hbar, \tag{3.16}$$

where q is the harmonic order, ω is the laser frequency, t_i is the time the electron is released in the laser field, t_f is the recollision time and S is the semi-classical action over the electron's trajectory. The phase of the emitted harmonics is therefore not simply related to the phase of the driving laser, but also to an intrinsic phase component that can vary with the laser intensity.

3.3 Macroscopic effects

The previous section addressed the single atom response which is responsible for generating the harmonic frequencies. However, high harmonic generation does not only involve a single atom but an ensemble which are coherently driven by the laser. The following section discusses the importance of propagation effects, such as phase-matching.

3.3.1 Phase-matching

For any non-linear optical process to be efficient, the emission from a large number of atoms must radiate coherently. As the driving laser passes through the medium, it induces a coherent harmonic signal that co-propagates with it. If this signal is to build in intensity over the entire interaction length, the phase velocity of the driving laser and induced harmonics must be the same, that is, the process must be *phase-matched*; this is shown schematically in figure 3.8. In phase-matched harmonic generation, the harmonic emission at all points in the interaction region adds constructively, leading to bright output at the harmonic frequency.

Consider the wave equation for the fundamental laser $E_f = e^{i(k_f x - \omega t)}$ and generated harmonics $E_q = e^{i(k_q x - q\omega t)}$ where k_f and k_q are the wavevectors of the fundamental and harmonic respectively and q is the harmonic order. Phase-matching is achieved when the phase mismatch, given by equation 3.17, is zero:

$$\Delta k = k_q - qk_f = 0. \tag{3.17}$$

In a phase-matched process ($\Delta\ k = 0$) the intensity grows as the square of the density (and hence in a homogeneous medium it grows as the square of the propagation distance). This is shown in figure 3.9(a) and is contrasted with a process that is not phase matched which results in a coherence length L_c after which there is a $\pi-$phase shift between the fundamental and harmonic (figure 3.9(b)). The coherence length is related to the phase mismatch Δk by $L_c = \pi/\Delta k$. Macroscopically, all the light generated in one coherence length is completely cancelled by light generated in the next coherence length and therefore, harmonics generated in a process which is not phase matched arise only from the last two coherence lengths.

The value of Δk is influenced by several factors. Since high harmonics are generated in a gas medium which exhibits a wavelength dependent

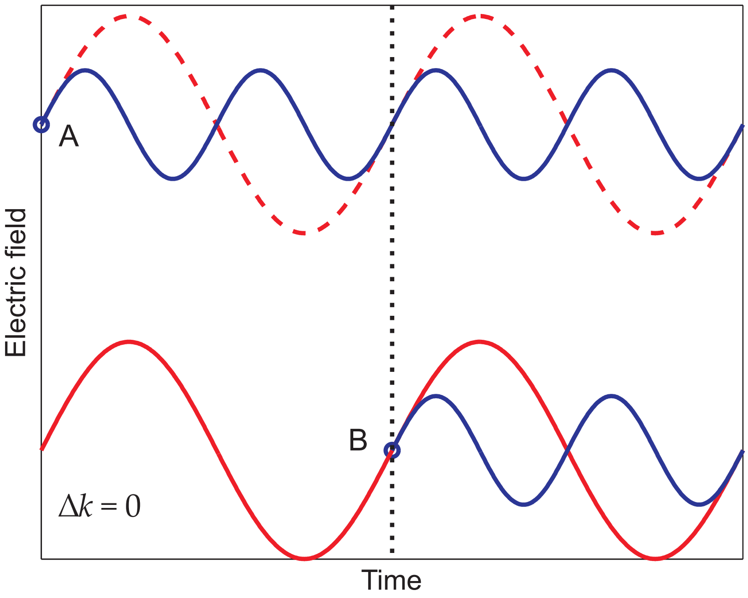

(a)

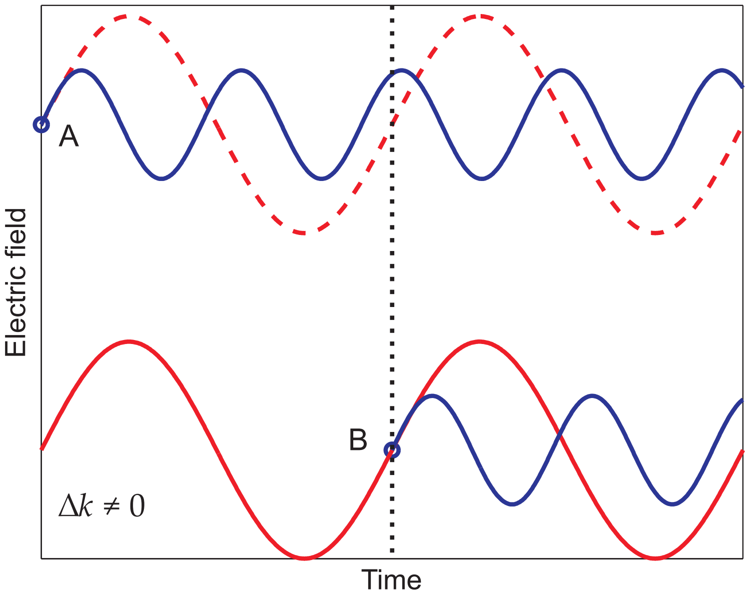

(b)

Figure 3.8: An example of phase-matching in second harmonic generation. (a) When the (red line) fundamental and (blue line) second harmonic propagate with the same phase velocity, the harmonics from points A and B add in phase, enhancing the signal; (b) when their phase velocities differ, the harmonics from A and B cancel.

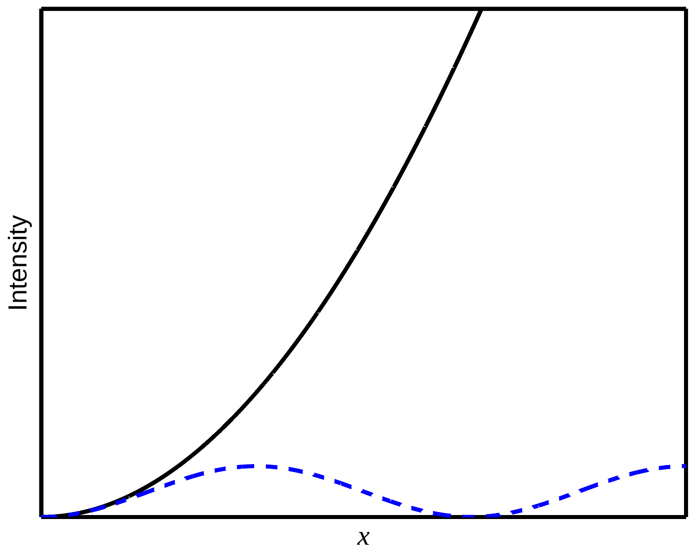

(a)

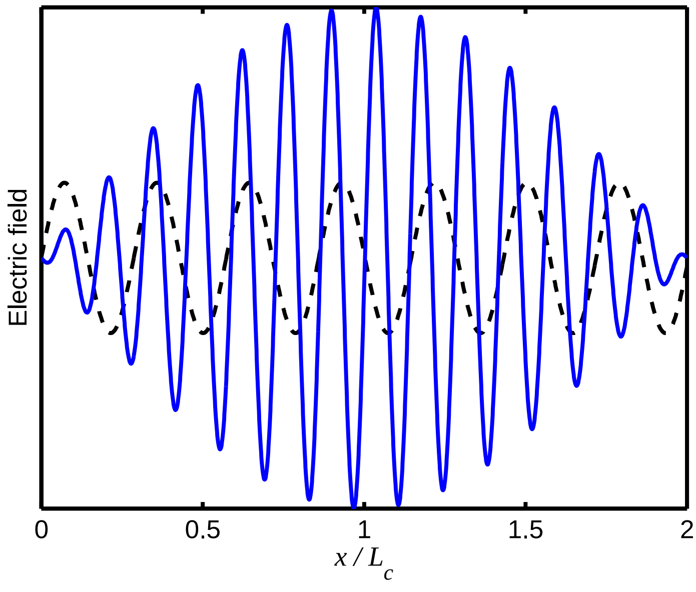

(b)

Figure 3.9: (a) When $\Delta k = 0$ (solid line) the intensity grows as the square of the propagation distance in the non-linear medium. When $\Delta k \neq 0$ (dotted line) the intensity oscillates between zero and a small value with period $2L_c$, where L_c is the coherence length. (b) Phase mismatch in second harmonic generation causes a build up in the harmonic field (solid line) over the coherence length L_c at which point a π-phase shift between the driving laser (dashed line) and harmonic results in destructive interference over the next coherence length.

refractive index, the wavevector will be modified by the neutral gas dispersion Δk_{disp}. The high intensities required to generate harmonics lead to the generation of free electrons and the plasma dispersion provides another contribution Δk_{plasma} to the wavevector. Additionally, a geometrical modification Δk_{geom} arises from focusing and propagation of the laser beam and the total wavevector mismatch can be written

$$\Delta k = \Delta k_{\text{disp}} + \Delta k_{\text{plasma}} + \Delta k_{\text{geom}}. \tag{3.18}$$

Geometrical effects

The geometrical contribution to the wavevector arises because of the need to confine the electromagnetic wave to a small region in space in order to create intensities sufficient for harmonic generation—in contrast, the geometrical contribution from an infinite plane wave would be zero. The form that Δk_{geom} takes depends on the experimental configuration. Figure 3.10 shows the three configurations that are commonly employed for high harmonic generation experiments: gas jet [83], gas cell [84, 85] and gas-filled capillary [9,86,87]. The gas jet and cell are examples of free space propagation where the geometrical wavevector contribution comes from the Guoy phase shift which occurs as the beam passes through the focus [88]. A gas cell may be preferred over a gas jet in some experiments where it is necessary to reduce the gas load into the vacuum chamber [89] or where it is desirable to have more control over the interaction length [90,91] which can lead to optimization of the phase-matching and improvements in conversion efficiency [92].

To generate harmonics in a gas-filled capillary, the laser is coupled into and propagates along a hollow waveguide and the geometrical contribution arises from the waveguide dispersion. There are several benefits to using a capillary in high harmonic generation experiments. The interaction

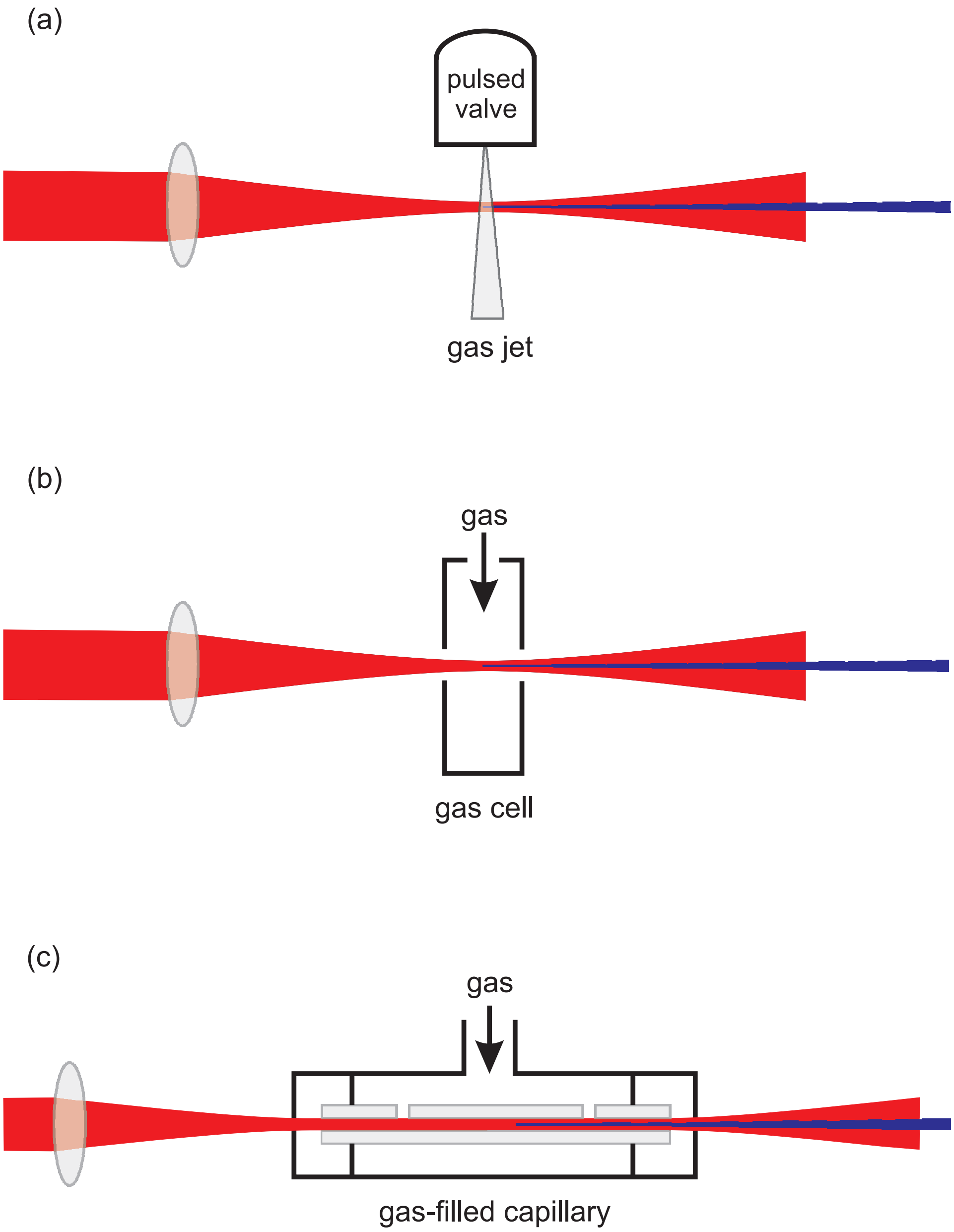

Figure 3.10: Three experimental geometries are typically employed in high harmonic generation: (a) gas jet, (b) gas cell and (c) gas-filled capillary.

length in a capillary can be greatly increased over that which is possible in a gas jet or cell, where the interaction length is limited by the confocal parameter and by ionization-induced defocusing. The waveguide controls the phase and intensity profile of the fundamental but the harmonics are virtually unaffected by the guide since they have a much smaller mode area. The fundamental propagates in a waveguide mode corresponding to a modified propagation vector which increases the phase velocity compared to free-space propagation. Thus, the waveguide contribution to Δk has opposite sign to the neutral gas and plasma contributions making it possible to balance the phase mismatch between the fundamental and harmonics [89].

To generate harmonics in a capillary, the laser is focused on the capillary and propagates inside. The waveguide modes, which are solutions to Maxwell's equations for the particular case of the boundary conditions of the hollow waveguide, have been given by Marcatili and Schmeltzer [93]. For a linearly polarized TEM$_{00}$ laser, coupled into a cylindrical fused silica waveguide of radius a filled with a gas of refractive index n, the propagation constant for the fundamental EH$_{11}$ mode is given by

$$k_f^2 = n^2 k_0^2 - \left(\frac{u_{11}}{a}\right)^2, \tag{3.19}$$

where k_0 is the propagation constant in vacuum and u_{11} is the first zero of the Bessel function J_0.

Dispersion

Any gas medium used for high harmonic generation exhibits a wavelength dependent refractive index, called dispersion, dependent on the spectral positions of absorption lines in the medium. The visible refractive index of the noble gases, such as argon, is slightly greater than unity and can be described using the Sellmeier equations [94]. These equations are fitted to experimental data and as such are valid over limited spectral regions, typically at wavelengths above the ultra-violet absorption bands. For the XUV, the refractive index, which is typically fractionally less than unity, may be calculated from atomic scattering factor data; this is discussed in more detail in chapter 7. Since the propagation vector depends on refractive index $k = (n\omega)/c$, this difference in the refractive index for visible and XUV photons leads to

$$\Delta k = \frac{2\pi q}{\lambda_f}\left[n_q - n_f\right], \tag{3.20}$$

where q is the harmonic order, λ_f is the fundamental wavelength and n_q and n_f are the refractive indices at the harmonic and fundamental respectively.

Refractive index

The refractive index of the partially ionized gas is given by [95]

$$n = 1 + P\left[(1-\eta)N_a\delta(\lambda) - \frac{\eta N_a r_e \lambda^2}{2\pi}\right], \tag{3.21}$$

where P is the gas pressure in bar, η is the ionization fraction, N_a is the number density at one bar, $\delta(\lambda) = \delta(\lambda_f) - \delta(\lambda_f/q)$ is the neutral gas dispersion at 1 bar and r_e is the classical electron radius. Any contribution from non-linear refractive index is usually neglected since its contribution is small at the intensities and low pressures encountered in the experiment [95].

From the refractive index in equation 3.21, the propagation constant for a laser of wavelength λ in the EH$_{11}$ mode of a hollow capillary is

$$k \approx \frac{2\pi}{\lambda} + \frac{2\pi P(1-\eta)\delta(\lambda)N_{atm}}{\lambda} + P\eta N_{atm} r_e \lambda - \frac{u_{11}^2\lambda}{4\pi a^2}, \tag{3.22}$$

where the terms correspond to the vacuum propagation, neutral gas dispersion, plasma dispersion and waveguide dispersion respectively. The phase mismatch $\Delta k = k_q - qk_f$ is therefore given by

$$\Delta k \approx q\frac{u_{11}^2\lambda_f}{4\pi a^2} + N_e r_e(q\lambda_f - \lambda_q) - \frac{2\pi N_a}{\lambda_q}[\delta\lambda_f - \delta(\lambda_q)], \tag{3.23}$$

where $N_a = (1-\eta)PN_a$ is the number of neutral atoms, $N_e = \eta PN_a$ is the number of electrons and λ_f and λ_q are the fundamental and harmonic wavelengths respectively. In previous studies, it has been assumed that the refractive index of the ionized gas atoms is unity [95]. This is not considered to be a good approximation and here we assume that the index of the ionized gas is approximately the same as the index of the neutral atoms. The effect of the waveguide on the XUV is ignored since the mode size of the XUV beam is considerably smaller than the fundamental and therefore it does not encounter the waveguide wall.

Figure 3.11 shows plots of Δk as a function of pressure and ionization fraction for each harmonic, obtained using equation 3.23. This illustrates that, for a particular ionization fraction, harmonic generation can be phase matched for higher photon energies using higher pressures. The ionization fraction, given by equation 3.10, is determined by the pulse energy and pulse length as shown in figure 3.12. Using a shorter fundamental pulse allows the atom to survive to higher intensity for a given ionization fraction which allows phase-matching for a given harmonic at a lower pressure. As will be seen in the next section, this is preferable because it reduces the amount of reabsorption of the X-rays by the generating medium.

It is important to remember that equation 3.23 does not imply that harmonics will be generated at these wavelengths, this depends on the energy and pulse length of the fundamental laser and generating higher energy harmonics requires sufficient laser energy according to equation 3.15.

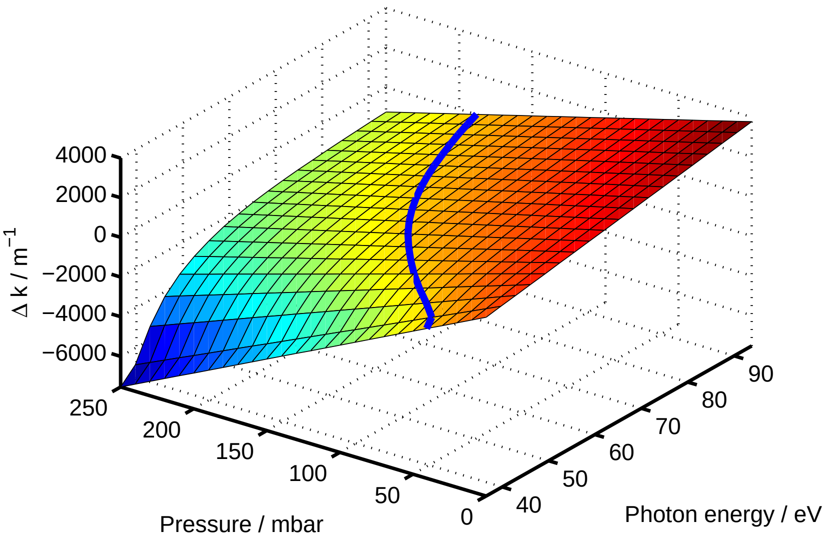

(a)

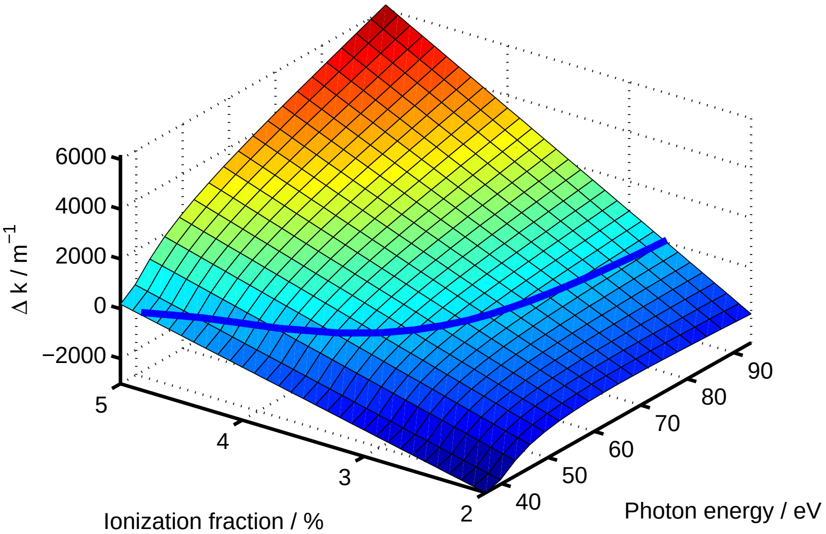

(b)

Figure 3.11: Phase mismatch Δk in argon (a) as a function of pressure and harmonic photon energy for a constant ionization fraction $\eta = 3.5\%$ and (b) as a function of ionization fraction and harmonic photon energy for a constant pressure $P = 80$ mbar. The solid blue line represents the $\Delta k = 0$ contour.

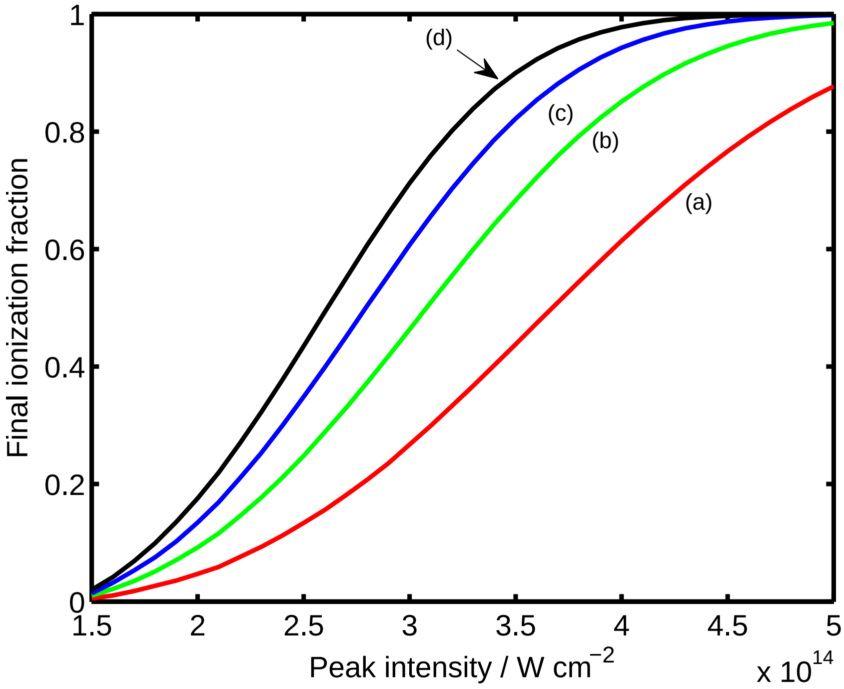

Figure 3.12: Final ionization fraction calculated from equation 3.10 for (a) 10 fs, (b) 20 fs, (c) 30 fs and (d) 40 fs pulses as a function of peak intensity, showing that atoms irradiated with shorter pulses reach a lower final ionization fraction for a given peak intensity.

3.3.2 Absorption

Most materials, including low pressure gases, are strongly absorbing to XUV. The absorption characteristics of materials to XUV can be predicted with reference to photoabsorption measurements tabulated by Henke *et al.* [14] or the comprehensive on-line database at the Center for X-ray Optics [96]. The transmitted intensity I through a length z of an ideal gas of constant pressure P, can be calculated from the tabulated mass absorption coefficient μ using the relationship,

$$I = I_0 \exp\left[-\left(\frac{P}{k_B T}\right)\mu z\right], \tag{3.24}$$

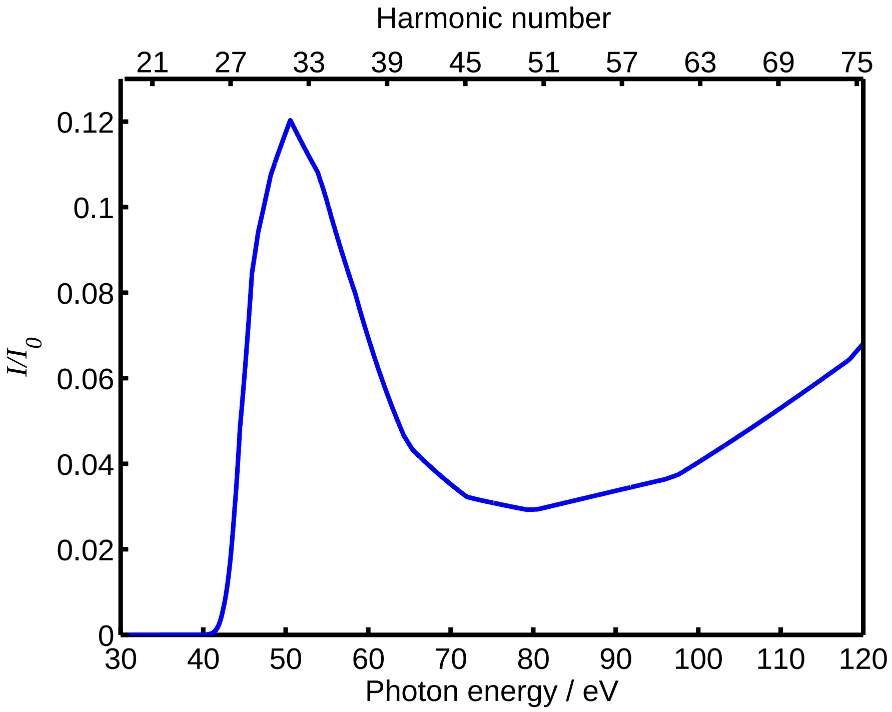

Figure 3.13: The transmission of 1 cm of argon at 100 mbar. Data from [14].

where I_0 is the incident intensity, k_b is the Boltzmann constant and T is the temperature. Figure 3.13 shows the transmitted intensity I as a function of photon energy for 1 cm of argon gas at a pressure of 100 mbar.

3.3.3 Harmonic build-up

The intensity build-up, given by both phase-matching and absorption in the generating medium, is modelled by [97]

$$|E|^2 \propto dN \left(\frac{1 + e^{-2\alpha L} - 2e^{-\alpha L} \cos \Delta k L}{\alpha^2 + \Delta k^2} \right), \tag{3.25}$$

where α is the absorption coefficient. The nonlinear source term here is dN, the number of atoms ionized at a given time and radius as, for a given gas, the probability of emission of a photon must be proportional to the number of ionization events that occur [97].

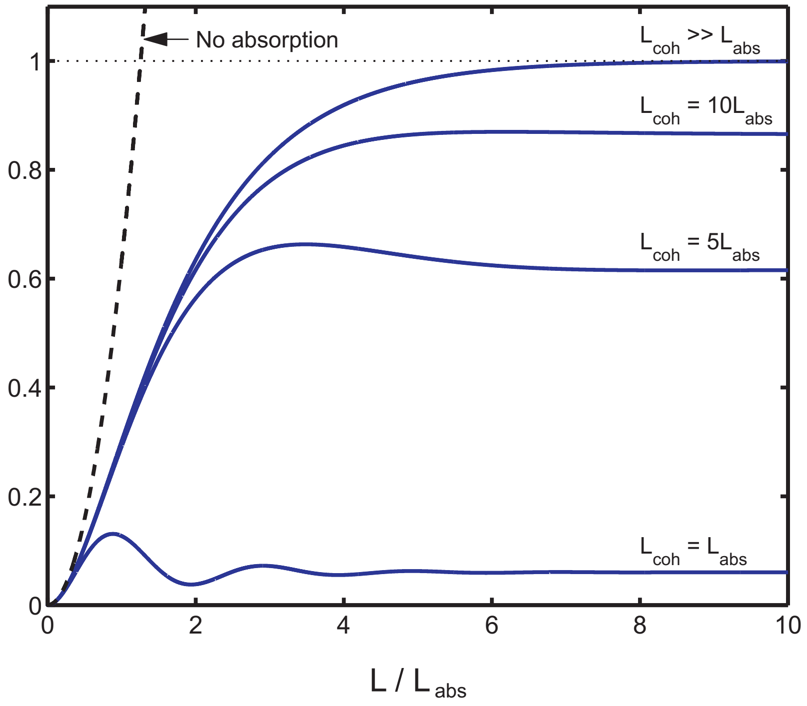

Figure 3.14: Harmonic build-up as a function of medium length L for different ratios of the absorption length L_{abs} to the coherence length L_{coh}. The dotted line corresponds to the case of zero absorption. Adapted from [98].

The length over which the harmonics build-up is limited by the shorter of the absorption length $L_{\text{abs}} = 1/2\alpha$ and the coherence length $L_{\text{coh}} = \pi/\Delta k$. The harmonic build-up for a phase-matched process ($\Delta\ k = 0$) as a function of medium length is shown in figure 3.14. It can be seen that in the absence of absorption, the build-up is proportional to the square of the medium length (as was shown in figure 3.9(a)). In the presence of absorption, even when the coherence length L_{coh} is infinite, the high harmonic emission saturates once the medium is longer than a few absorption lengths [98]. As the coherence length decreases, the harmonic emission saturates at smaller values. Figure 3.15 illustrates the relative intensity of harmonics of different energies generated in 30 mm of argon, showing that the optimum region for harmonic generation in this regime is between 45–65 eV. In figure 3.15(a) the intensity is plotted as a function of pressure and in figure 3.15(b) this is plotted as a function of ionization fraction and shows that phase-matching in argon is not possible when the ionization fraction exceeds $\sim\ 4\%$.

3.4 Summary

From this chapter it should be clear that the measured harmonic emission is a complicated function of the single atom response to the laser field which depends on the laser pulse energy and pulse length, the effects of phase-matching which also depend on the experimental geometry, and the absorption properties of the generating medium. The next chapter looks in detail at the experimental apparatus that was constructed to generate the high harmonics.

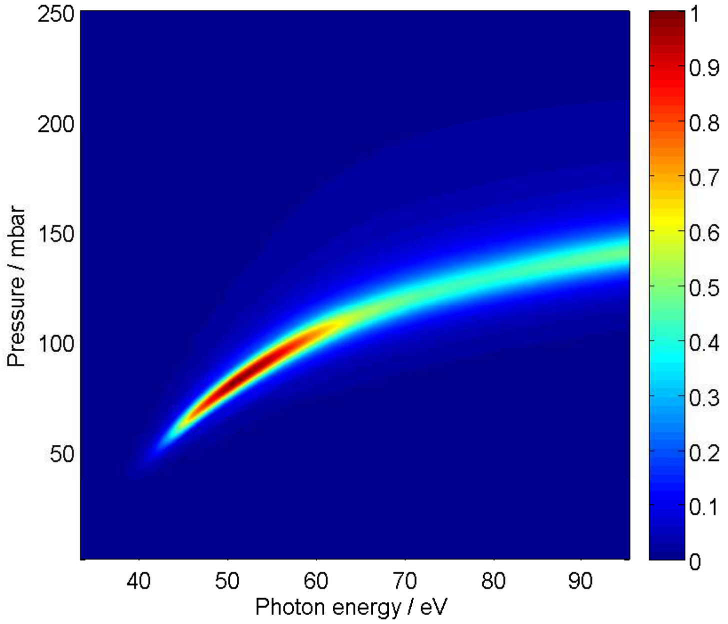

(a)

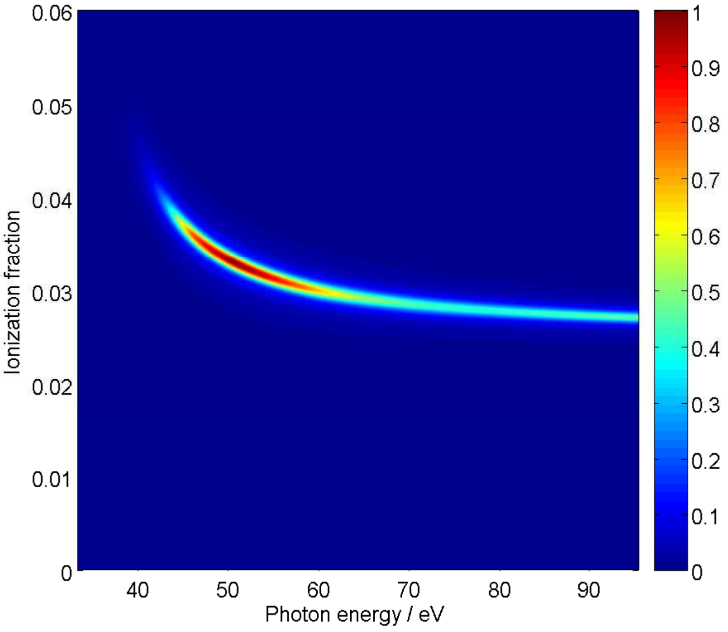

(b)

Figure 3.15: Predicted harmonic build-up in 30 mm of argon, shown on a normalized intensity scale; (a) as a function of pressure for an ionization fraction $\eta = 3.3\%$ and (b) as a function of ionization fraction for a pressure of 80 mbar.

Chapter 4

Generating High Harmonics

4.1 Introduction

This chapter discusses the experimental apparatus that was developed to generate and characterize the high harmonics. This developmental work forms a large part of my contribution to the project. In this chapter, each of the key components will be discussed in detail, including the femtosecond laser oscillator and amplifier system (section 4.2), the capillary based high harmonic source (section 4.3), filtering (section 4.3.4) and X-ray spectrometer (section 4.3.5).

4.2 High power, ultra-fast laser system

The past fifteen years has seen the rapid development of ultra-fast lasers. Compact and reliable oscillators, capable of generating optical pulses in the femtosecond regime, are now widely available [99]. The direct generation of pulses < 5 fs, has been demonstrated [100] and we are fast approaching the limit imposed by the optical cycle period of 2–3 fs for lasers operating in the visible and near infrared region.

Generally, these oscillators operate with peak powers of the order of a

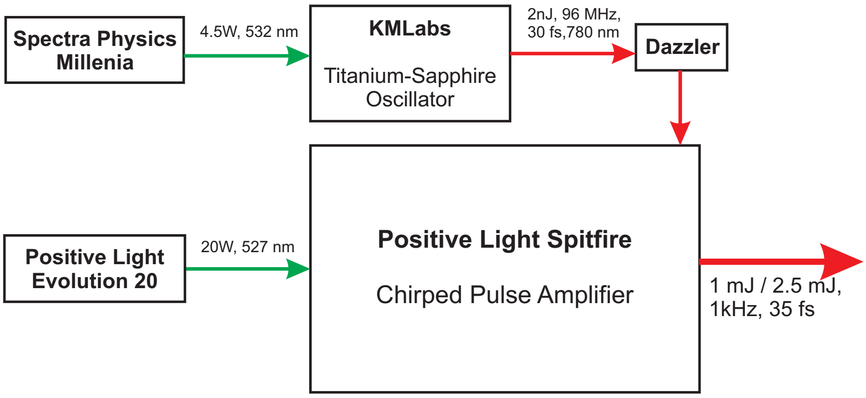

Figure 4.1: Overview of the high power, ultra-fast laser system

megawatt [101], making it necessary to use some form of laser amplifier to reach the peak laser fields high order harmonic generation requires (see section 3.2.3), which are several orders of magnitude more intense than the oscillator alone can provide.

For the experiments described in this thesis, we have used a commercial laser system which incorporates a Kapteyn-Murnane Laboratories (KML) oscillator to generate the initial ultra-fast pulse, in combination with a Positive Light Spitfire chirped pulse amplifier (CPA) system. A schematic overview of this system, including the pump lasers, is shown is figure 4.1.

4.2.1 Ti:sapphire oscillator

The KML oscillator [102] is a Kerr-lens mode-locked [103–107], titanium doped sapphire (Ti:sapphire) laser. Kerr-lens mode-locking relies on the optical Kerr effect whereby the refractive index n of a medium becomes a function of the incident intensity I according to,

$$n(I) = n_0 + n_2 I \tag{4.1}$$

where n_0 is the normal refractive index of the medium and n_2 is the intensity dependent, non-linear refractive index. Since the intensity of a laser beam is typically higher towards its center, the non-linear change of refractive index will be strongest at the center, resulting in an intensity induced lens and hence self-focusing of the beam. Self-focusing is the basis of Kerr-lens mode-locking whereby an aperture (either a real, physical aperture, or a virtual aperture caused by the finite size of the optics) causes gain to be higher in the case of self-focusing. When the laser is operating in a pulsed mode, the focused intensity within the Ti:sapphire crystal exceeds that required to induce self-focusing. In a cavity aligned for operation without this lens, the introduction of a lens causes loss within the cavity. However, modest displacements of one of the cavity mirrors can result in a decrease in loss in the laser cavity when Kerr lensing is present and hence the laser can be aligned to be stable in either mode.

As a solid-state laser material for use in ultra-fast lasers, Ti:sapphire has several desirable properties including high thermal conductivity, high energy storage density [101] and a wide gain bandwidth [108] which allows it to support extremely short pulses [103]. The crystal is pumped with 4.5 W from a diode based, frequency-doubled Nd:YAG laser (Spectra Physics Millenia) operating at 532 nm; this is an ideal source since it corresponds well with Ti:sapphire's broad absorption maximum at 500 nm [108].

Figure 4.2 shows a schematic of the KML cavity. A pair of prisms compensate for dispersion caused by the Ti:sapphire crystal and other intra-cavity optics. Careful optimization of the intra-cavity dispersion using short Ti:sapphire crystals and prism pairs [102, 109], is necessary to produce the shortest possible pulses [110–112].

4.2.2 Dazzler

The output from the KML is directed into the Dazzler, as shown in figure 4.1. The Dazzler is a type of acousto-optic modulator (AOM), called an acousto-optic programmable dispersive filter (AO-PDF), a device which

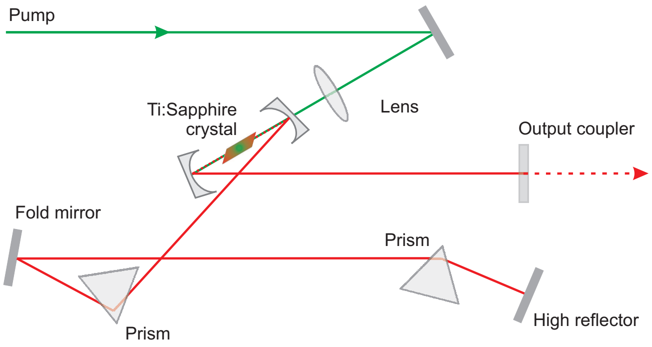

Figure 4.2: Schematic of the optical configuration of the Kapteyn-Murnane Laboratories (KML) Ti:sapphire Oscillator

can be used to shape the phase and amplitude profile of an ultrashort pulse [113].

The optical geometry and electrical connections to the AO-PDF are shown schematically in figure 4.3. An acoustic wave is launched into the 2.5 cm long birefringent paratellurite TeO_2 crystal by a piezoelectric transducer excited by an RF signal from a function generator controlled by a laptop computer. The acoustic wave travels along the z-axis of the crystal, reproducing the temporal shape of the generated RF signal. A 1kHz synchronization signal from the Evolution laser power supply is passed through a Stanford Research Systems Digital Delay Generator and is used to ensure that the arrival of the acoustic wave into the AO-PDF coincides with the arrival of the KML laser pulse that will be subsequently selected to seed the regenerative amplifier (see section 4.2.3). The Dazzler is not able to operate at the full 96 MHz repetition rate of the KML laser because of the acoustic wave velocity and this synchronization ensures that each pulse that is to be amplified is modified identically by the acoustic wave.

The incident optical wave initially travelling along the ordinary axis of

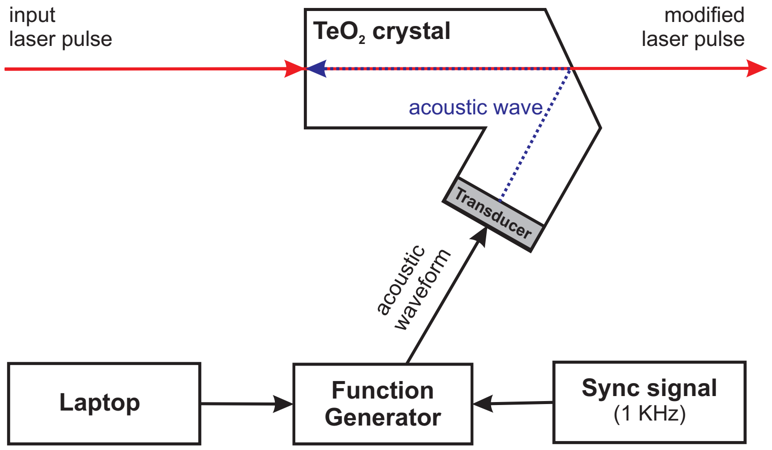

Figure 4.3: The acoustic wave is launched into a TeO$_2$ crystal by a transducer from an RF function generator controlled by a laptop computer. The crystal is cut such that the acoustic wave reflects from the end face and copropagates with the input optical wave. The acoustic and optical waves are carefully synchronized to a 1kHz reference signal. Adapted from reference [114].

the crystal has polarization parallel to that axis, with a propagation direction collinear with the propagation direction of the acoustic wave. The optical wave can interact with the acoustic wave, causing an optical wave to be coupled into the extraordinary axis with polarization parallel to the extraordinary axis (figure 4.4). For a specific frequency of the acoustic signal, phase-matching between the acoustic and optical signal can result in a coupling of the ordinary and extraordinary axes. At any one spatial frequency, in the acoustic signal, only one optical frequency can be diffracted at a position z. Each optical frequency ω travels a distance z before encountering the phase matched frequency and being diffracted into the extraordinary mode. Since the refractive index of each of these modes is different, each frequency will see time delay with respect to one another. The relative amplitude of the output pulse depends on the acoustic intensity at the position $z(\omega)$ where it is diffracted.

Even in a well optimized CPA system, where the positive dispersion of

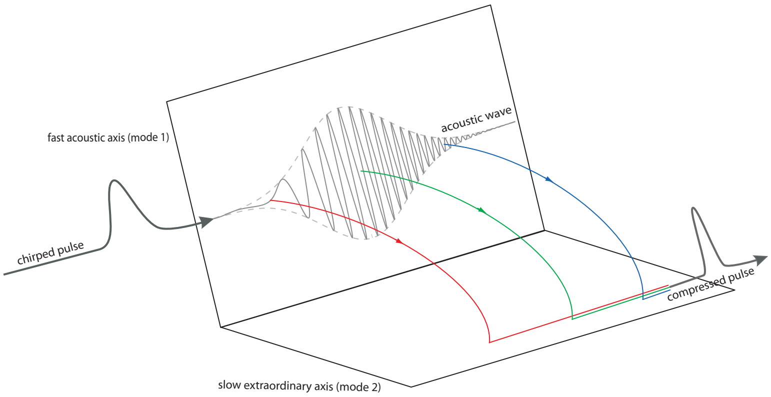

Figure 4.4: The individual frequency components of an input pulse originally incident along the ordinary axis of the crystal may be selectively diffracted into the extraordinary axis at a position along the crystal axis. In this way, the path length of each frequency component in the ordinary and extraordinary axes, which have different refractive indices, can be controlled. (Based on reference [113].)

the stretcher matches well the negative dispersion of the compressor, other optical components in the amplifier introduce GVD, higher order dispersion and nonlinear dispersion which must be compensated for. While it is possible to introduce prism pairs or dispersion compensating mirrors that will do this, they are not programmable and are limited to the first orders [114]. By using an AO-PDF, such as the Dazzler, we are able to address two key limitations of the CPA systems. We are able to correct for the GVD introduced by optical elements in the beam path and also to correct for any high order (third order or greater) dispersion introduced by the stretcher and compressor.

The Dazzler can make arbitrary programmable changes to the spectrum and phase of the pulse, for example, we could use it to create a hole in the centre of the spectrum (figure 4.5) which might be useful to overcome non-uniform narrowing of the amplified gain medium which can lead to a narrowing of the spectral bandwidth. It is possible to use the AO-PDF to correct for this by programming a filter where the transmission at the

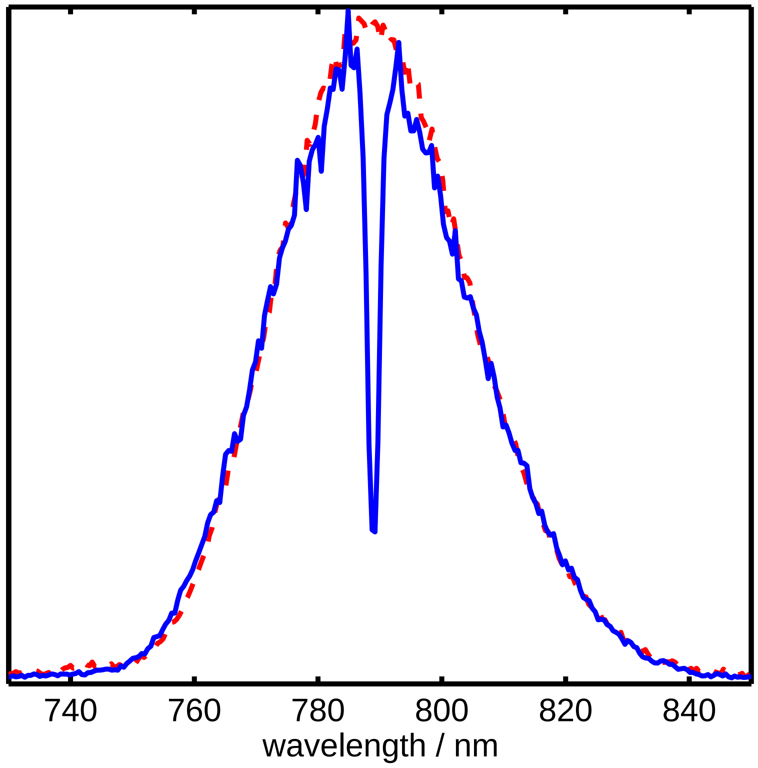

Figure 4.5: The KML laser spectrum before (dashed) and after (solid) the Dazzler has been programmed to give a spectral hole at 787 nm (FWHM 1.6 nm).

wings is greater than in the center.

In this way, the Dazzler can be used to produce an ideal pulse shape, or more frequently, can be used to optimize the pulse for a particular application, that is, optimization to produce high order harmonics. In chapter 5 we will look at the way we have used the Dazzler to frequency shift the high harmonics.

4.2.3 Chirped pulse amplifier

A commercial chirped pulse amplifier (CPA), the Positive Light Spitfire, was used to increase the energy of the seed pulse from the KML oscil-

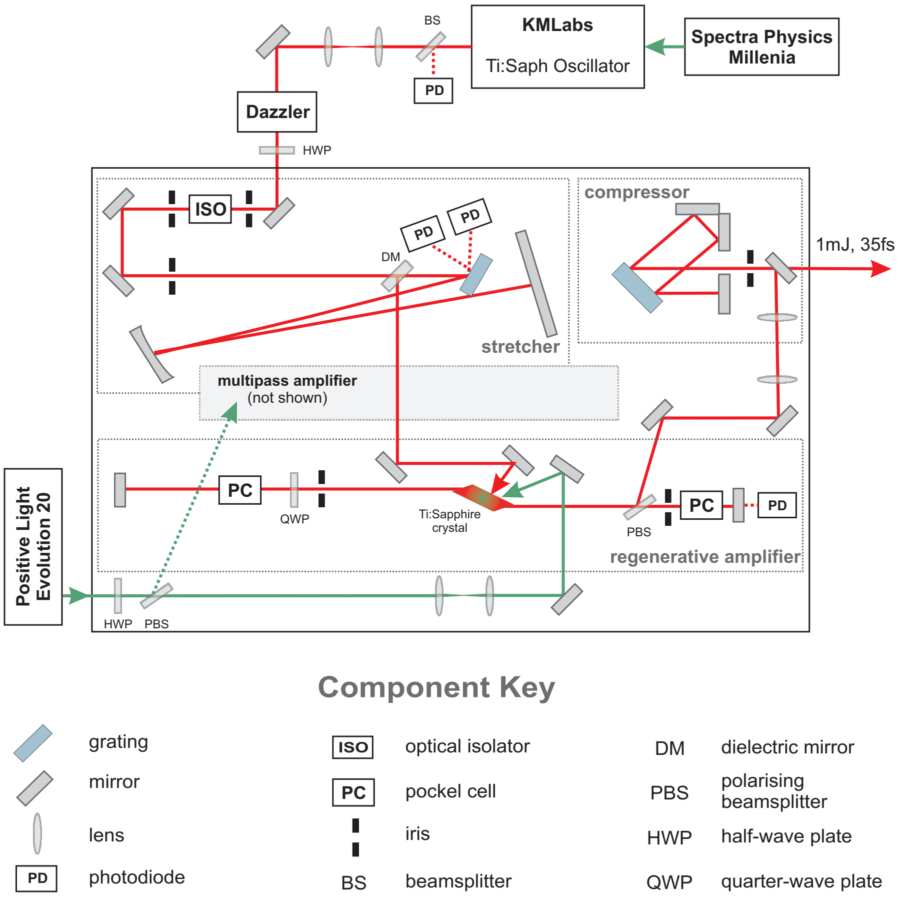

Figure 4.6: Schematic representation of the laser amplifier system

lator from the nanojoule to millijoule levels. The amplifier is capable of producing 35 fs pulses at a repetition rate of 1 kHz with 1 mJ, 2.5 mJ or 25 mJ of energy using the regenerative amplifier only, the regenerative amplifier and double-pass amplifier stage or the regenerative amplifier and two-stage multi-pass amplifier respectively. For the work described in this thesis, energies up to 1 mJ were used from the regenerative amplifier and therefore the 2.5 mJ and 25 mJ lines will not be described further.

The optical layout of the Spitfire CPA is shown in figure 4.6. The input pulse from the KML oscillator passes through a Faraday rotator which acts as an optical isolator and is then stretched to $\sim$ 100 ps using a double pass onto the stretcher grating. This allows the maximum energy to be extracted from the Ti:sapphire crystals before saturating, reducing the peak power of the pulse to prevent damage to the gain medium and reducing non-linear effects during amplification, such as self focusing, and self phase modulation [115]. A pair of photodiodes monitor the bandwidth of the stretched pulse, ensuring sufficient bandwidth to prevent damage to the gain medium.

The stretched seed pulse passes into the regenerative amplifier cavity. The amplifier is pumped by a 20 W diode pumped, frequency-doubled Nd:YLF laser (Positive Light Evolution 20) which is split by a half-wave plate and polarising beam splitter into 8 W to pump the regenerative amplifier and 12 W which can be used to power the optional multipass amplifier.

In the regen, the seed beam is carefully overlapped with the green pump laser on the Ti:sapphire crystal. The regen cavity is defined by two high reflectors and the number of round-trips around the cavity is controlled by the Pockel cells which are controlled by a digital delay generator (Positive Light SDG) which also synchronizes the arrival of seed laser pulses with the pump laser pulses. After a defined number of cavity round-trips and just before the gain medium is saturating, the pulse is switched out of the regen cavity.

After being output from the regen cavity, the amplified beam has an energy of approximately 1 mJ. At this stage, it can optionally pass through a further amplification stage which uses a bow-tie shaped multi-pass configuration through another Ti:Saphire crystal. This section is not shown on figure 4.6 since it was not used in the experiments in this thesis as it was found that the use of the multi-pass amplifier significantly degraded the beam quality.

After amplification, the beam makes a double pass onto the compressor grating which applies a negative chirp to compress the pulse close to the original seed pulse length. At the output from the amplifier, we typically measure a pulse length of 35–40 fs which can be optimized by tuning the distance between the compressor gratings which are on a motorized controlled mount.

4.2.4 Pulse characterisation

When we measure an ultrashort pulse, we wish to know its intensity and phase profile. In the frequency domain we can use a standard spectrometer to measure the spectrum, giving us intensity versus wavelength. In our case, we use an Ocean Optics HR2000CG spectrometer. Or, we can make measurements in the time domain, a technique which has historically been dominated by the autocorrelator which measures intensity versus time, effectively using the pulse to measure itself. Unfortunately, autocorrelators are not without their drawbacks [116]. Specifically, as the pulse becomes more complex, the autocorrelation of the pulse in fact becomes simpler causing the fine structure of the pulse to be lost. Secondly, the autocorrelation does not easily reveal the FWHM of the pulse since this depends on the pulse shape. If one assumes a Gaussian pulse with multiplication

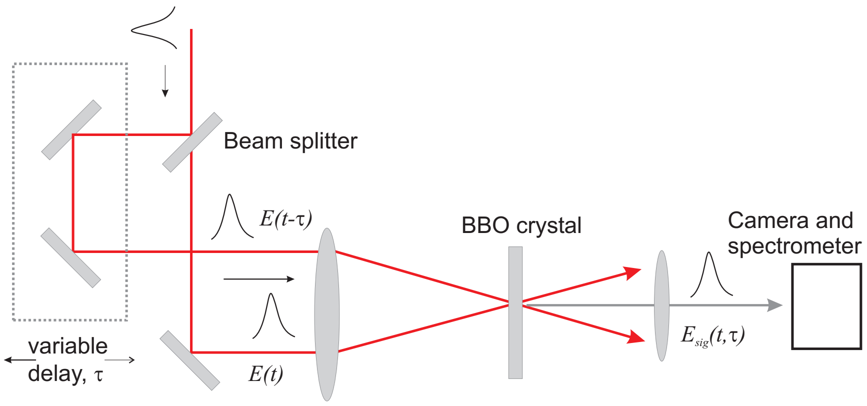

Figure 4.7: Experimental layout of an SHG FROG.

factor 1.41 a longer pulse will be predicted than if one assume a sech^2 with a multiplication factor of 1.54. This is further complicated by the fact that no pulse exactly fits a Gaussian or sech^2 function [116]. Further to this, autocorrelators can be quite tricky to align, and unfortunately, when not aligned correctly they can give misleading results.

FROG and GRENOUILLE

More recently, a series of techniques referred to as Frequency Resolved Optical Gating (FROG) have been developed which are able to extract the full intensity and phase data from an ultrashort pulse. In FROG, the incoming pulse is split in two and one pulse delayed with respect to the other, in much the same way as in autocorrelation. However, in FROG we then measure the spectrum of the signal pulse with respect to delay. This results in a time-frequency domain measurement where we can generate a two-dimensional trace of intensity versus frequency and delay. It now becomes possible to extract the full intensity and phase data from an ultrashort pulse [116].

Numerous geometries of FROG exist; figure 4.7 shows a second harmonic generation FROG (SHG FROG). In the SHG FROG, the pulses are spectrally resolved from an autocorrelator based around a second harmonic generating crystal, resulting in a trace of intensity I versus frequency ω and delay τ related to the spectrum of the pulse [116]

$$I(\omega,\tau) = \left| \int_{-\infty}^{\infty} E(t) + E(t-\tau)\exp(-i\omega t)dt \right|^2 . \tag{4.2}$$

The SHG FROG is a very sensitive measurement technique frequently used for low input pulse energies such as the unamplified pulses from a Ti:sapphire seed laser. The reason for this sensitivity is in part due to the strength of the second order non-linearity (compared to the weaker third-harmonics used by some FROG systems). Additionally, the SHG FROG gives a relatively high signal to noise ratio since the signal light is of a different frequency from the input pulse and hence scattered light may be easily filtered.

Trebino, O'Shea and co-workers have devised a novel SHG FROG (figure 4.8) using a thick non-linear crystal to replace the thin crystal and spectrograph, and a Fresnel biprism to replace the beam splitter and delay line. These innovations have led to the GRENOUILLE (GRating-Eliminated No-nonsense Observation of Ultrafast Incident Laser Light E-fields) [117]—an extremely compact ultrashort pulse measurement device capable of full intensity and phase measurements. The lack of a delay line means that the GRENOUILLE is a single shot device, making it possible to compare individual pulses from low repetition rate amplifier systems [118].

The Fresnel biprism is a prism with an apex angle approaching 180° [119]. When a wide beam is incident on the biprism, the beam is split into two and the resulting rays are overlapped into the SHG crystal with variable delay. The crystal is imaged onto a CCD camera, giving a plot of signal versus position (delay) in the horizontal plane, as in a traditional FROG geometry. However, in contrast to the conventional FROG geome-

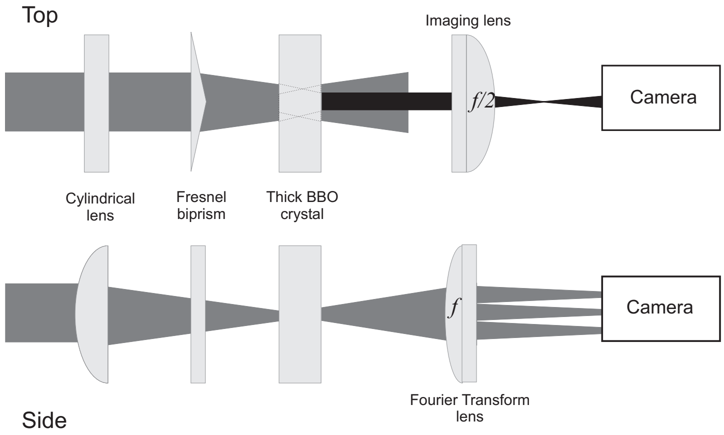

Figure 4.8: Schematic showing the GRENOUILLE beam geometry. (Adapted from reference [117].)

try, the beams in the GRENOUILLE are automatically aligned in space and time [117]. This greatly simplifies the optical alignment, negating the need to align a delay line.

The other innovation with the GRENOUILLE is in the use of a thick SHG crystal which reduces the phase-matching bandwidth and hence the phase matched wavelength becomes a function of angle. In this way, the thick SHG crystal also acts as a spectrograph. The cylindrical lens maps the wavelengths at different output angles as a linear function of vertical position on the camera. The signal received by the camera is analogous to an SHG FROG experiment where delay is plotted horizontally against wavelength vertically.

The GRENOUILLE was used to monitor the pulse length from the amplifier and the GRENOUILLE was a useful aid to alignment, compressor optimization and for optimizing the delay settings which control the amplifier's Pockel cells. A thin 4% beam splitter (Femtolasers) inserted into the beam after the amplifier allowed live viewing of the FROG trace during the experiment. Figure 4.9 shows a typical GRENOUILLE trace from the Spitfire CPA system.

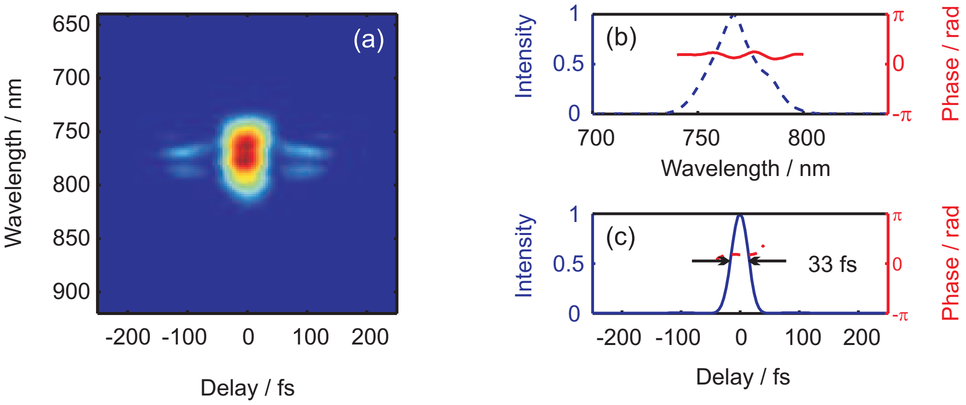

Figure 4.9: (a) The GRENOUILLE trace of a 33 fs pulse from the Spitfire CPA system. (b) The time domain intensity and phase and (c) the frequency domain intensity and phase.

4.3 XUV generation

This section describes the experimental setup that was created for the high harmonic generation experiment. Figure 4.10 shows a schematic layout of this experiment. The hollow capillary waveguide is held within a differentially pumped vacuum system and the laser pulses are coupled into this using a 0.7 m focal length lens via a 1 mm thick fused silica optical window. After the capillary, filters can be inserted to attenuate the fundamental and the XUV beam continues downstream towards the interaction chamber and spectrometer.

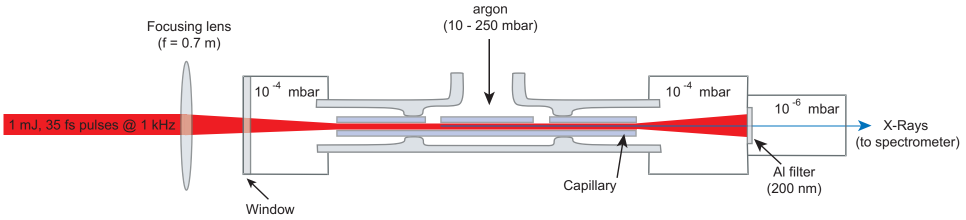

Figure 4.10: Schematic showing the high harmonic generation experimental setup

4.3.1 Hollow waveguide

After leaving the amplifier and passing through a beam splitter to allow a pick-off for pulse measurement with the GRENOUILLE, the beam height is adjusted to match the height of the X-ray generation capillary with a periscope containing a pair of silver mirrors. The laser is then focused with a 0.7 m focal length fused silica lens, into a 150 μm capillary waveguide. Laser pulses energies of up to 850 μJ were coupled into the capillary.

The hollow capillary waveguide was manufactured by the fibre fabrication group of the Optoelectronics Research Center. It is fabricated from fused silica and was drawn from a large precursor using a fibre drawing tower to have an inner diameter of 150 μm and an outer diameter of 1.6 mm. The waveguides used in these experiments were all 70 mm long and had a pair of 300 μm gas inlet holes drilled at a distance of 20 mm from either end.

Waveguide coupling

For a TEM$_{00}$ beam focused on-axis into a hollow waveguide, only the EH$_{1m}$ modes will be excited. Of these modes, the EH$_{11}$ mode has the lowest theoretical loss and the highest peak intensity and therefore it is important to determine the focal length lens required to optimize the coupling into this mode. The spatial profile of the EH$_{1m}$ modes can be approximated by the zero-order Bessel function J_0,

$$E(r) = E_0 J_0 \left(u_m \frac{r}{a} \right), \tag{4.3}$$

where a is the bore diameter, $0 \leq r < a$ and a gaussian beam with a $1/e^2$ waist ω is represented by,

$$E(r) = E_0 \exp\left(-\frac{r^2}{\omega^2} \right). \tag{4.4}$$

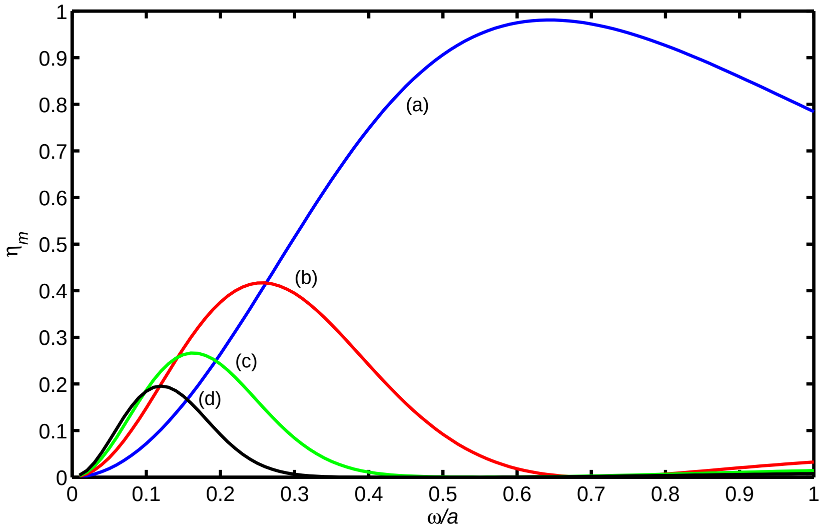

Figure 4.11: Calculated coupling efficiency in a hollow capillary waveguide as a function of the spot size to bore size ratio ω/a for the (a)EH$_{11}$, (b)EH$_{12}$, (c)EH$_{13}$ and (d)EH$_{14}$ modes.

The coupling efficiency of the incident beam to each of the EH$_{1m}$ capillary modes can be then be expressed by the overlap integral [120]

$$\eta = \frac{[\int_0^a \exp(-r^2/\omega^2) J_0\left(u_m \frac{r}{a}\right) r \, \mathrm{d}r]^2}{\int_0^\infty \exp(-2r^2/\omega^2) r \, \mathrm{d}r \, \int_0^a J_0^2\left(u_m \frac{r}{a}\right) r \, dr.} \tag{4.5}$$

Figure 4.11 shows the coupling efficiency for the EH$_{1m}$ modes plotted as a function of the spot-size-to-bore-size-ratio ω/a. It is clear from this that the optimum coupling efficiency into the lowest loss EH$_{11}$ mode occurs for the ratio $\omega/a \cong 0.64$ and for this ratio, $\eta_1 = 98.1\%$ and $\eta_2 = 0.5\%$.

It was experimentally determined that a 700 mm focal length lens produces the highest coupling efficiency. This gives a spot size of 81 μm which is slightly smaller than the optimum spot size suggested by the ratio $\omega/a \cong 0.64$. The reason for this is that the focusing conditions required for maximum coupling into the EH$_{11}$ mode do not correspond to the minimum loss condition for the 150 μm capillary that was used. To calculate the theoretical transmission of a hollow waveguide, it is necessary to account for both the attenuation of and coupling efficiency to each of the waveguide modes. The transmission $P(z)$ of a capillary of length z is given by the sum over all waveguide modes [120],

$$P(z) = \sum_m \exp(-2\alpha z), \tag{4.6}$$

where the attenuation coefficient α is given by [93]

$$\alpha = \left(\frac{u_{nm}}{2\pi}\right)^2 \frac{\lambda^2}{a^3} n, \tag{4.7}$$

where u_{nm} is the mth root of the zero-order Bessel function, λ is the wavelength, n is the real refractive index and a is the bore radius of the capillary. Figure 4.12 shows that for minimum loss, the coupling conditions should be $\omega/a \cong 0.58$, which is consistent with our experimental measurements. The maximum transmission efficiency that was measured was 75%, compared to a theoretical value of 94%.

Using slightly tighter focusing conditions has an additional benefit. It was noted that the transmission efficiency of several of the hollow capillaries used in the experiments was observed to drop over several hundreds of hours of operation, eventually reaching a minimum of $\sim 40\%$. The increased loss was accompanied with an observation that the front entrance of the capillary became increasingly cone shaped and white deposits appeared, probably from ablation of the glass. It is believed that the damage resulted from residual laser power in the glass at the front face of the capillary. This is not unexpected considering that, for a TEM_{00} laser beam, optimized for maximum coupling into the EH_{11} mode with beam waist $\omega = 0.64a$, approximately 0.1% of the laser energy will be incident on the front face of the capillary.

In applications such as this, where precise control over the focal size

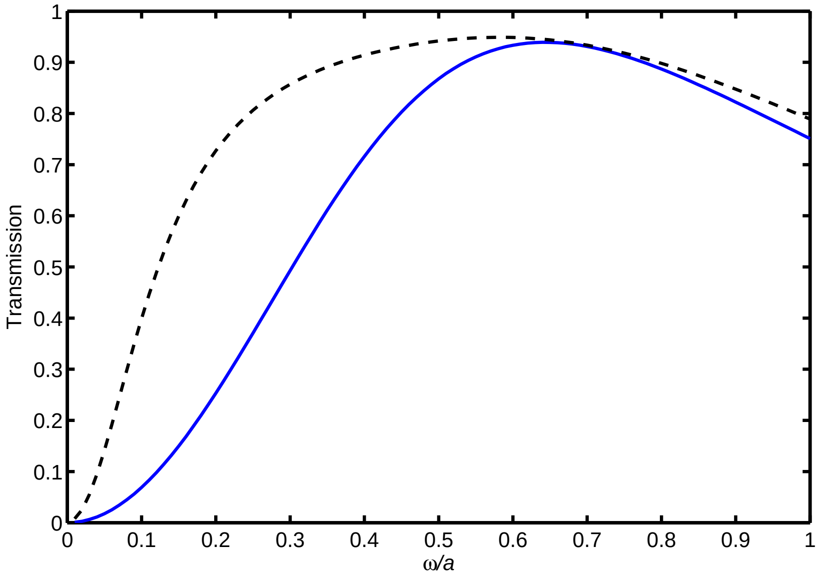

Figure 4.12: Transmission of a 70 mm long, 250 μm bore hollow-glass capillary as a function of the beam waist to bore size ratio ω/a for (solid line) optimum coupling into the EH_{11} mode and (dashed line) minimum loss.

and intensity of laser beams is particularly important, it is necessary to fully characterize the propagation parameters of the beam, including the M^2. The M^2 value provides a measure of the number of times *diffraction limited* the beam is [88]. A theoretically ideal laser with a diffraction limited beam has an M^2 of 1, though few lasers come close to this value. The M^2 allows us to calculate the size of the real beam by multiplying the calculated beam waist at any point by the value of M^2. Hence, M^2 values are extremely important in working out the properties and focusing characteristics of non-diffraction-limited beams. In our group, Praeger has developed a novel technique for measuring the M^2 from the output of the chirped pulse amplifier [121]. The technique relies on multiple reflections between partially transmitting mirrors to measure on a camera the size of the beam as it is passes through a focus. Typical values for the M^2 of the amplified beam measured using this method were ~ 2.

Gas inlet holes

The waveguides used in these experiments had a pair of 300 μm gas inlet holes drilled at a distance of 20 mm from either end of the capillary. These holes define a region of constant gas pressure in the center of the capillary, with the pressure dropping off linearly towards the ends. The shape of this gas profile also prevents high gas pressure building at the entrance of the fibre which may otherwise lead to ionization induced defocusing and a reduction in coupling efficiency [122]. Drilling the capillary was a novel approach by myself which greatly simplifies alignment in contrast to the multi-segment capillaries common previously [86] and has since been used by other groups [79].

The gas inlet holes were drilled in the capillary waveguide using a mechanical micro-machining technique. Diamond tipped, 300 μm drill bits supplied by Lunzer Inc. were used in conjunction with an ultrasonic mill. Lengths of the glass capillary were attached to a metal jig with wax and the holes were drilled in the desired pattern, positioning the capillary using a mechanical stage fitted with digital readout. Cooling fluid is used to prevent the drill from overheating and, typically, each bit drilled 4–8 holes before requiring replacement. The glass capillary was removed from the metal jig by dissolving the wax in Ecoclear at $50°$C. Following this, the capillaries were hand cleaved to length using a ceramic tile and cleaned in an ultrasonic bath containing acetone for 30 minutes to remove loose debris from the drilling and any contamination from grease or cooling fluid.

To aid the connection of gas and vacuum services to the thin and fragile capillary, the capillary is secured into a custom made glass T-piece (figure 4.13) which provides mechanical support to prevent the capillary from bending and provides vacuum sealing between the gas inlet (10–250 mbar) and the high vacuum system ($\sim 10^{-6}$ mbar). The T-piece is coupled to the high vacuum system with O-ring sealed compression fittings (Swagelok

Ultra-Torr) at either end of the T-piece which are sufficiently flexible to allow for alignment of the capillary. The capillary was sealed into the T-piece using a small quantity (20–60 μL) of UV curing acrylic adhesive (Permabond UV7248) which was confirmed to be suitable for vacuum conditions down to 10^{-7} mbar and was preferred to an epoxy resin because it is transparent, index-matched to the glass T-piece and capillary and stable under UV irradiation.

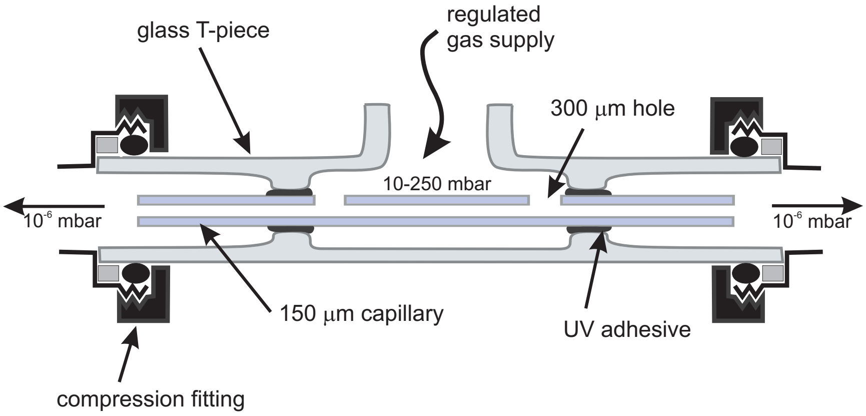

Figure 4.13: The capillary waveguide is sealed into a custom designed glass T-piece to provide mechanical support and to aid the attachment of gas and vacuum services.

Pressure control system

It is important to be able to accurately regulate the pressure inside the capillary. The phase-matching conditions (and hence the harmonics that can be generated) are affected by the pressure and hence we must be able to keep the pressure constant while still allowing control in order to optimize the system. A Tescom ER3000 pressure regulator is used to control the pressure inside the capillary. This computer controlled valve is connected to an RS485 network and controlled with custom written LabView software to monitor and control the pressure using a proportional, integral, differential (PID) control system which allows accurate feedback control and fast re-

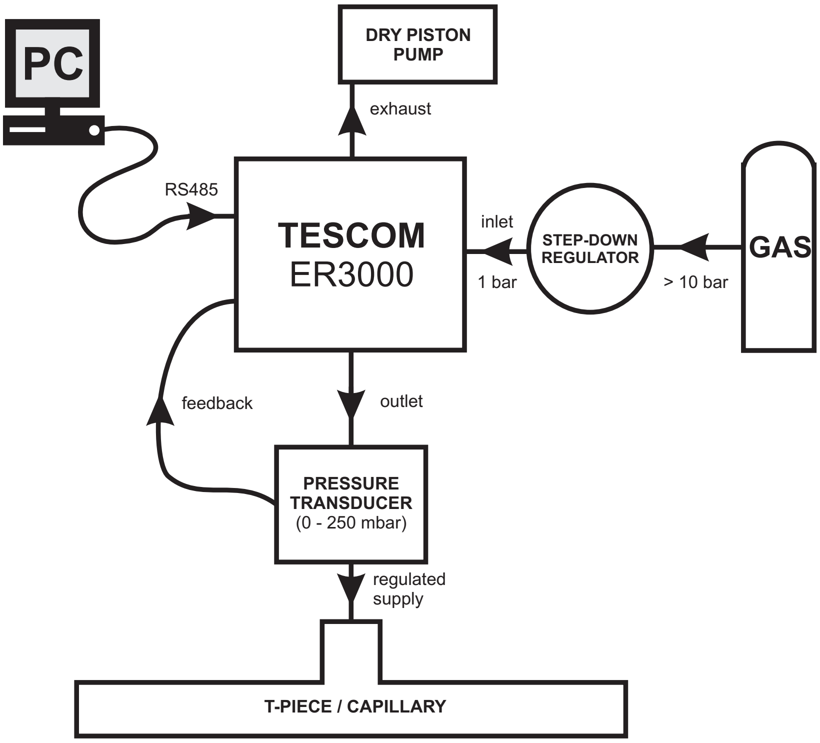

Figure 4.14: The configuration of the pressure control system that regulates the gas pressure inside the capillary waveguide.

sponse. Figure 4.14 shows the configuration of the pressure control system. A short flexible plastic pipe connects the glass T-piece which supports the capillary to the regulated gas supply. At the end of this pipe, a pressure transducer provides feedback to the ER3000 on the capillary gas pressure. The ER3000 inlet valve is connected to the gas supply via a step-down regulator to supply an inlet pressure to the Tescom at 1 bar. The exhaust valve is connected to a 15 m^3 h^{-1} dry piston pump (Leybold Ecodry M15) to allow pressure regulation to sub atmospheric pressures and to ensure a fast response when pressure changes are required.

4.3.2 Optical windows

The vacuum entrance window is 1 mm thick fused silica (Apex Services). At 780 nm, the group delay dispersion of the 1 mm thick fused silica window is 36 $\text{fs}^2\ \text{mm}^{-1}$ which stretches a 30 fs pulse to 30.2 fs. The thickness and diameter are a trade off to provide sufficient strength to support the vacuum while allowing the diameter to be wide enough that the beam can be large while passing through the window to reduce non-linear effects or the possibility of optical damage. Fused silica has a damage threshold of 1 J cm^{-2} for 30 fs pulses [123] and color centers can be formed in the glass at even lower fluence [124]. The window is placed 0.3 m from the input face of the capillary where the beam has expanded to 10 mm and the energy dropped to < 1 mJ cm^{-2}.

4.3.3 High vacuum system

The T-piece is attached to the vacuum tubes which define the laser and X-ray optical axes of the experiment, from laser input window through to sampling chamber and spectrometer (figure 4.15). The T-piece is coupled at either end to a pair of modified vacuum T-pieces using O-ring sealed compression fittings (Swagelok Ultra-Torr). The vacuum T-pieces are mounted on pairs of orthogonal translation stages (Newport UMR) and are coupled to the rest of the high vacuum system via flexible edge welded bellows (Leybold Vacuum). This arrangement allows precision alignment of the capillary with respect to the laser. The vacuum optical axis is connected to a vacuum pumping backbone via further flexible edge welded bellows which provides symmetrical pumping to either end of the hollow capillary. Vacuum pumping is achieved using a 300 litres per second turbomolecular pump (Leybold TW300) which is backed by a 15 $\text{m}^3\ \text{h}^{-1}$ dry piston pump (Leybold Ecodry M15) and achieved ultimate pressures of 10^{-7} mbar or typically 10^{-5} mbar when operating the capillary at pressures of around

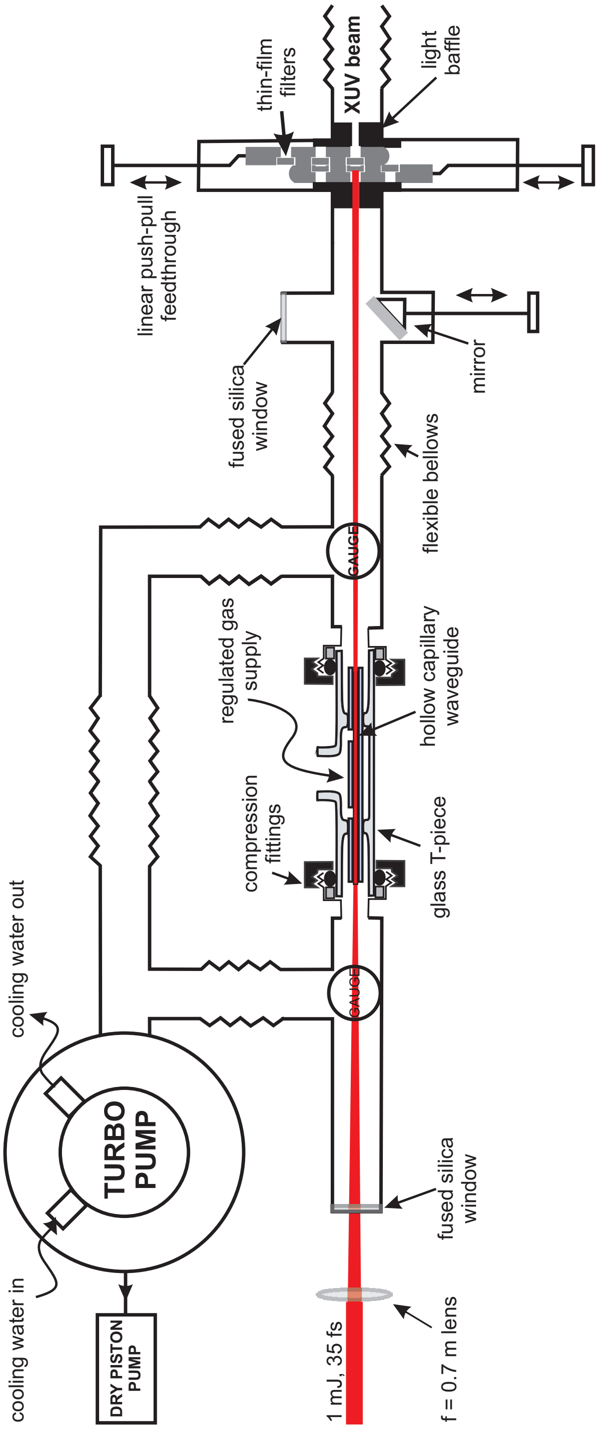

Figure 4.15: High vacuum system

70 mbar.

After the capillary, a mirror on a 45 degree mount can be optionally inserted into the beam using a linear push-pull feedthrough. The mirror reflects the infra-red laser out of the chamber through a fused silica window to allow measurement of the laser power coupled through the capillary and to monitor the quality of the output mode.

4.3.4 XUV filtering

Many XUV detectors are equally sensitive to visible light, therefore it is essential to filter the driving laser which is many orders of magnitude more intense than the XUV. The driving laser can easily swamp the XUV signal on spectrometers and cameras and risks damaging their detectors.

Thin films of materials such as aluminium, zirconium and beryllium can be used to separate the XUV emission and driving laser which are collinear. Aluminium is a particularly useful material in this regard and is widely used as a filter material because of its durable mechanical properties, wide bandpass in the XUV (17–80 nm), and excellent visible light blocking characteristics. In the case of a 150 nm aluminium filter, Powell *et al.* have made detailed measurements of the visible light transmission characteristics of aluminium films using a sensitive spectrophotometer [125] and measured the transmission at 800 nm to be typically $< 10^{-7}$. Pinholes caused by defects in deposition, damage or dust are one of the greatest problems with ultra-thin film filters and their presence can result in a reduction of the expected optical density. It was found that multilayered foils, for example, composed of two 100 nm aluminium layers that were deposited separately, resulted in pinhole free foils for applications requiring very low levels of laser leakage.

The performace of thin films in the XUV can be predicted with reference to photoabsorption measurements tabulated by Henke *et al.* [14] or the comprehensive on-line database at the Center for X-Ray Optics [96]. The filter transmission T in the XUV can be calculated from the tabulated mass absorption coefficient μ using the relationship

$$T = \exp\left(-\rho\mu x\right), \tag{4.8}$$

where ρ is the density of the material and x the thickness. Figure 4.16 shows the energy dependent transmission characteristics for pure aluminium and a number of other materials of interest as XUV filters.

In many cases, the experimentally measured transmission of the filters will be lower than those shown in figure 4.16 because of the build up of oxide layers on the surface of the materials which age the filters. Storing the filters under vacuum or dry nitrogen will reduce their exposure to water and oxygen and slow down the ageing process. Aluminium filters have been shown to age over time as a result of oxide growth on the surface, with oxide layers up to 15 nm forming on the surface [126]. Figure 4.17 compares the transmission through a pure aluminium filter with one contaminated with 15 nm of aluminium oxide on each surface, this shows that for a 150 nm filter, the transmission at 30 nm falls from 70% to 12%; this calculation compares well with observed experimental transmisions measurements.

Thin film filters are mounted onto stainless steel rings and may have a nickel mesh grid for support, however, these reduce the transmission by a further 15% [126] and in the experiments described in this thesis unsupported films of 5 mm diameter, supplied by Lebow Company, were used.

Thin film filters, especially those that are unsupported, must be treated with care because they are extremely fragile and susceptible to damage by small pressure differentials, mechanical stress caused by careless handling or poorly designed mounts, dust and debris or intense laser radiation [127].

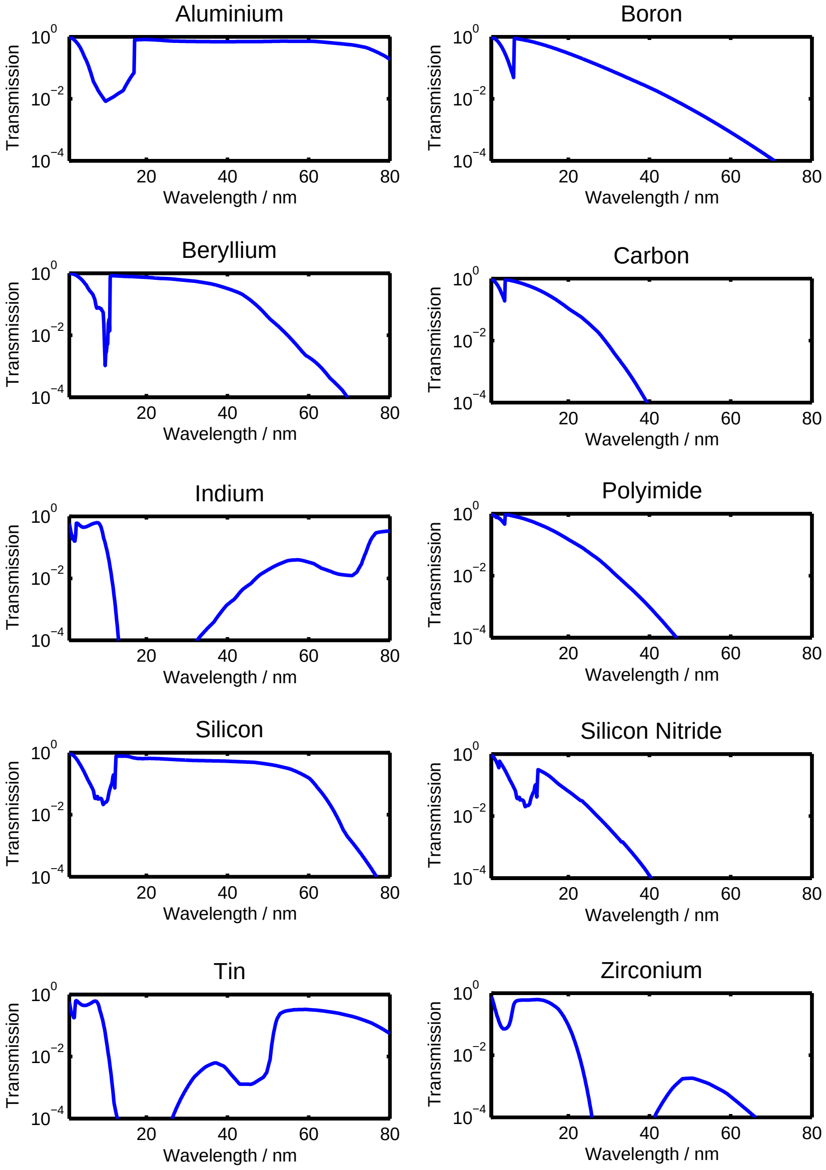

Figure 4.16: The wavelength dependent transmission of 150 nm films for various materials of interest as XUV filters. Data from reference [96].

Careful design of the filter holder (figure 4.18) was required to reduce the possibility of damage to the filters. The filter holder consists of a pair of trays, each of which houses a maximum of five filters, which can be positioned in front of the beam using push-pull linear feedthroughs. The trays

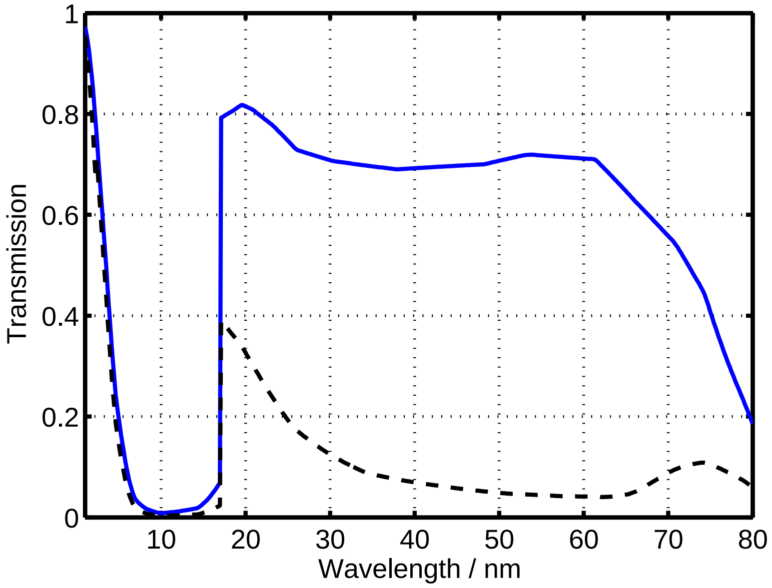

Figure 4.17: The wavelength dependent transmission of an aluminium foil (solid line) compared with an aluminium foil that has 15 nm of aluminium oxide (dashed line). Data from reference [96].

slide between light tight baffles housed within a modified vacuum cross. The baffles prevent scattered light from passing around the sides of the filters and entering the experimental chamber or spectrometer. The filters were placed sufficiently far from the exit of the capillary that the filters were not damaged by the laser (see figure 4.15). In each tray, one filter position is left blank so that the driving laser beam may be used for alignment purposes and to allow a path for gas to flow during pump-down, to prevent the filters from being damaged by the build up of a pressure differential across them.

4.3.5 XUV spectrometer

An XUV spectrometer was placed on the beamline after the experimental chamber and was used for characterizing the XUV beam and as a diagnostic tool. The spectrometer, supplied by Shulz Scientific, was a Rowland cir-

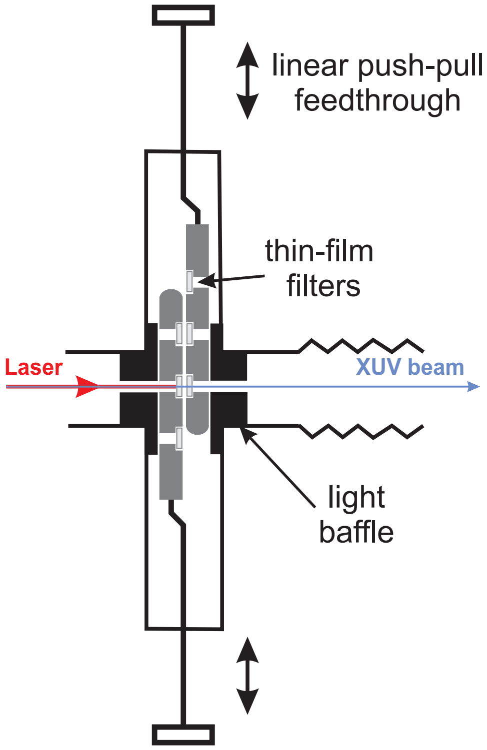

Figure 4.18: The XUV filtering system consists of two trays each housing a maximum of five filters held in a modified vacuum cross which has baffles to reduce the amount of scattered light. A pair of manual linear feedthroughs are used to position the filters in the beam path.

cle geometry, grazing incidence spectrometer with a curved multi-channel plate (MCP) detector. A selection of three concave diffraction gratings gave access to the spectral region 5–60 nm. Full details of the optical design and wavelength calibration of the XUV spectrometer are given in Appendix A.

4.4 Results

This section discusses the results from a series of experiments that were conducted to determine the optimum phase-matching conditions for efficient high harmonic generation as well as examining the spectral and spatial properties of the beam.

4.4.1 Phase-matched generation

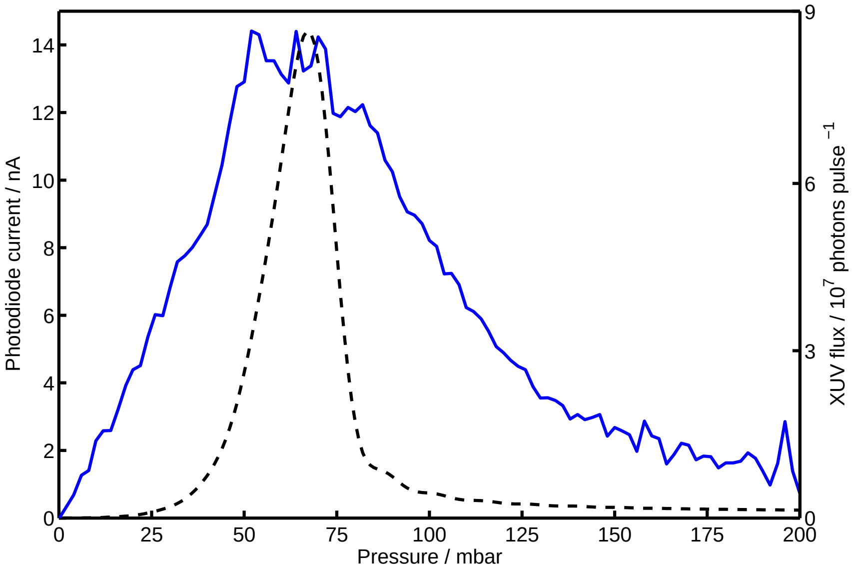

Figure 4.19: (solid line) Total X-ray emission measured with a calibrated photodiode as a function of argon pressure for a 40 fs 600 μJ laser pulse and (dashed line) the theoretical X-ray emission calculated using phase-matching and including the contribution over the 21st-31st harmonics for a capillary filled with a 3 cm region of argon at constant pressure and a 3% ionization fraction.

Figure 4.19 shows the total harmonic flux as a function of argon pressure for a 40 fs, 600 μJ input laser pulse with a 70% coupling efficiency into the capillary, corresponding to a peak intensity of 2×10^{14} W cm^{-2}. A 200 nm thick aluminium filter was used to block the fundamental and the data was recorded using a calibrated XUV photodiode (XUV100C, OSI Optoelectronics) and lock-in amplifier (Stanford Research System SR800). In this instance, optimum phase-matching is obtained for pressures between 50–75 mbar which results in the emission of greater than $(8 \pm 0.4) \times 10^7$ photons per pulse, giving a total conversion efficiency of the order of 10^{-6}. The uncertainty in the experimental value of the photon flux is predominantly caused by fluctuations in the energy and harmonic distribution of the source and was estimated by comparing the range of values recorded over a series of experimental measurements.

Plotted as an overlay in figure 4.19 is the phase matching curve predicted from equations 3.23 and 3.25. This simple model calculates the contribution from each of the harmonics (21–31), for a capillary filled with a 3 cm region of constant gas pressure and a 3% ionization fraction. This theoretical fit matches the position of the peak in the experimental data well but does not fit the general shape of the experimental data very well. The reason for this is that phase-matching is a spatio-temporal problem and for accurate modelling, it is necessary to account for the radial intensity distribution of the laser beam and the time evolution of the pulse and its consequent affect on ionization. In the capillary geometry described in this thesis, it is also necessary to account for the longitudinal pressure distribution in the capillary.

The optimum pressure for phase-matching is dependent upon the harmonic energy and therefore different harmonics will be phase-matched at different argon pressures. Figure 4.20 illustrates the experimentally measured phase-matching curves for the 23rd, 25th and 29th harmonics. There is a clear shift in the optimum phase-matching pressure with the lower harmonics being phase-matched at lower pressure which is consistent with the observation in figure 3.15(a). Phase-matching depends on the ionization fraction η which varies as a function of time throughout the pulse, therefore, harmonics may be phase matched at different pressures as the pulse evolves in time, for example, when $\eta = 2\%$, the optimum phase-matching for 50 eV photons is at 42 mbar, however $\eta = 3\%$ this has shifted to 65 eV. The lower energy harmonics are more strongly affected by argon absorption and therefore build up will be greater at lower argon pressures. Another interesting feature of figure 4.20 is the double peak which is observed particularly strongly for the 23rd harmonic. The second peak at

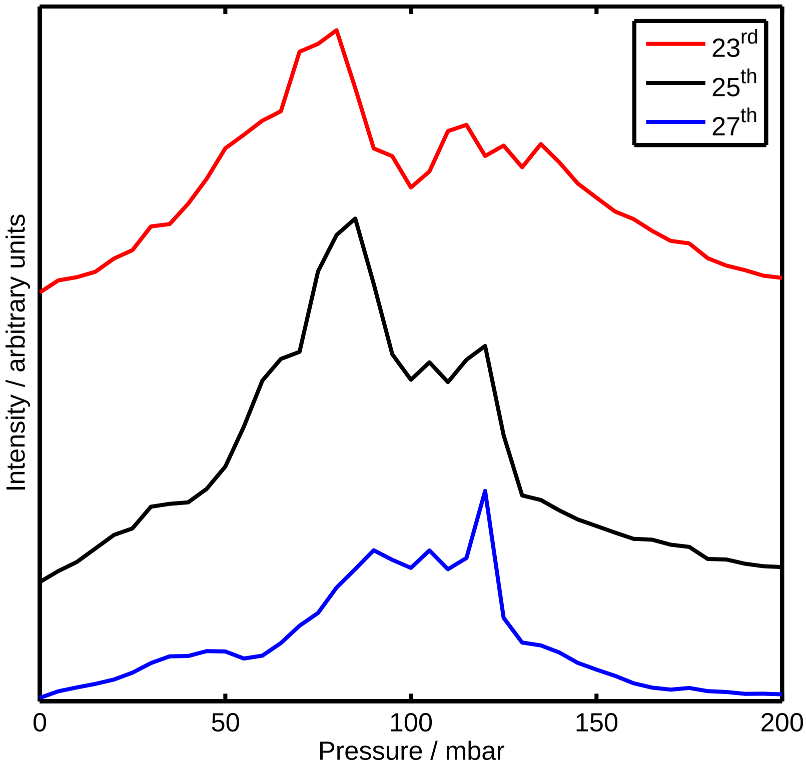

Figure 4.20: Phase-matching curves for the 23rd, 25th and 29th harmonics as a function of argon pressure.

higher pressure results from the capillary's pressure profile (figure 4.21). The capillary has two gas inlet holes which define a region of constant gas pressure in the centre of the capillary, with the pressure dropping off approximately linearly to both ends. When the pressure in the central region is too high to successfully phase match, there exists a region within this pressure gradient that is at the correct pressure for phase-matching. These effects further add to the broadening of the phase-matching curve observed in figure 4.19. The detailed modelling of all of these effects is outside the scope of this thesis and within our group, Rogers is developing a spatio-temporal phase-matching model [97] which accounts for them.

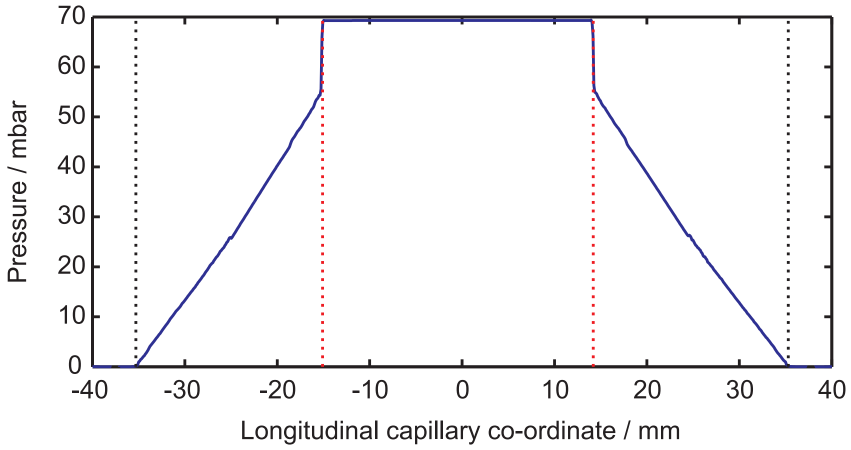

Figure 4.21: The gas pressure profile (solid blue line) within the hollow capillary for an input pressure of 100 mbar as calculated by the computational fluid dynamics package Ansys CFX. The two holes (dashed red lines) define a region of constant gas pressure and outside this region, the pressure drops off linearly to the ends of the capillary (dashed blue lines).

4.4.2 XUV spectrum

Figure 4.22 shows the high harmonic spectrum of argon recorded at a pressure of 80 mbar, for a 40 fs laser pulse of energy 600 μJ. At 80 mbar, emission from the 25th harmonic (31 nm) is optimized, with a photon flux of $\sim 3 \times 10^7$ photons pulse^{-1}, measured by comparison with the total X-ray signal from the calibrated X-ray photodiode.

The recorded argon emission is occurring in a spectral region where argon is strongly absorbing. To calculate the transmission of a gas medium of length L with a non-uniform pressure profile given by $P(z)$, equation 3.24 must be integrated over the pressure profile to give

$$I(z) = I_0 \ \exp\left[-\int_0^L \left(\frac{P(z)}{k_B T}\right) \mu \ dz\right], \tag{4.9}$$

where z is the longitudinal capillary coordinate. In the high harmonic experiments a 150 μm capillary is used, with a pair of 300 μm gas inlet holes drilled 20 mm from either end of the 70 mm capillary. To understand the

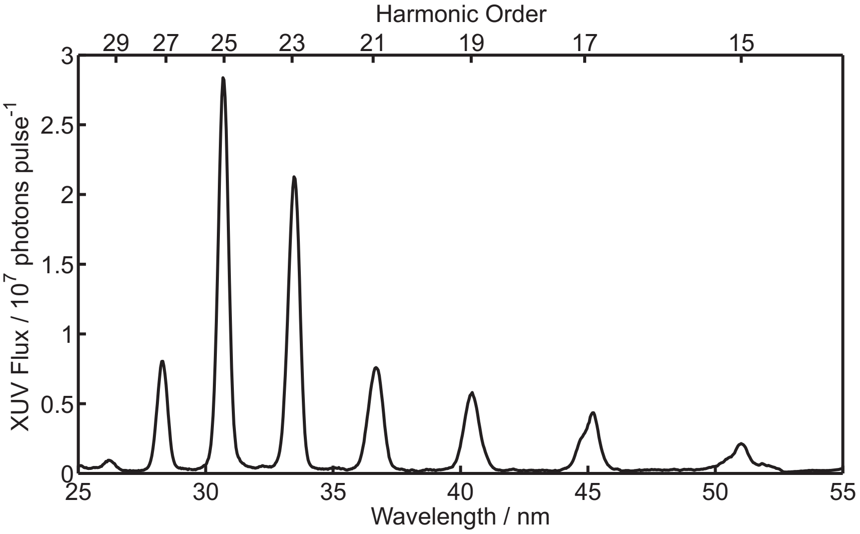

Figure 4.22: A typical XUV spectrum for an argon pressure of 80 mbar, for a 40 fs laser pulse of energy 600 μJ.

absorption processes in the capillary, it is important to understand the pressure profile. The holes define a constant gas pressure region in the centre of the capillary with the pressure dropping off linearly towards the ends. This is confirmed in figure 4.23(b) which shows the pressure profile of a typical 150 μm capillary, with an inlet pressure of 100 mbar, which was calculated in our group by Praeger using the computational fluid dynamics package Ansys CFX. Figure 4.23(a) shows a contour plot of the transmission probability for X-rays generated at each point along the length of a capillary with the pressure profile shown in figure 4.23(b). This shows that X-rays generated near the front of the capillary are much more likely to be reabsorbed and suggests that the 30 mm constant gas pressure region is longer than necessary and that harmonic generation may be enhanced by controlling the pressure profile to reduce the argon pressure outside the generation region.

The full spectral data set for pressures between 10–200 mbar is shown

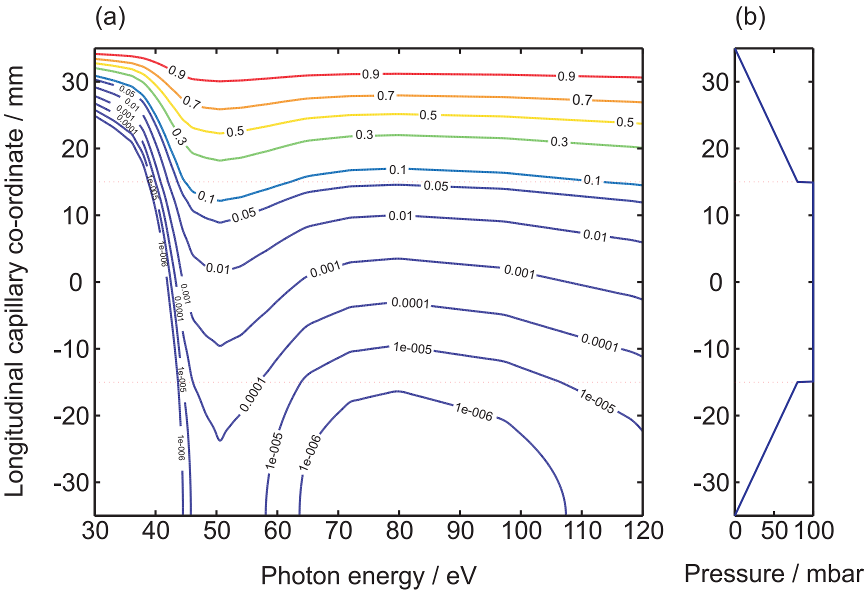

Figure 4.23: (a) The transmission probability for X-rays generated at each point along the length of a capillary with pressure profile (b) calculated by using computational fluid dynamics package Ansys CFX. The input face of the capillary is at the bottom of this graph and the dashed lines indicate the location of the gas inlet holes which define a region of constant gas pressure in the centre of the capillary; outside this region, the pressure drops off linearly to the ends of the capillary.

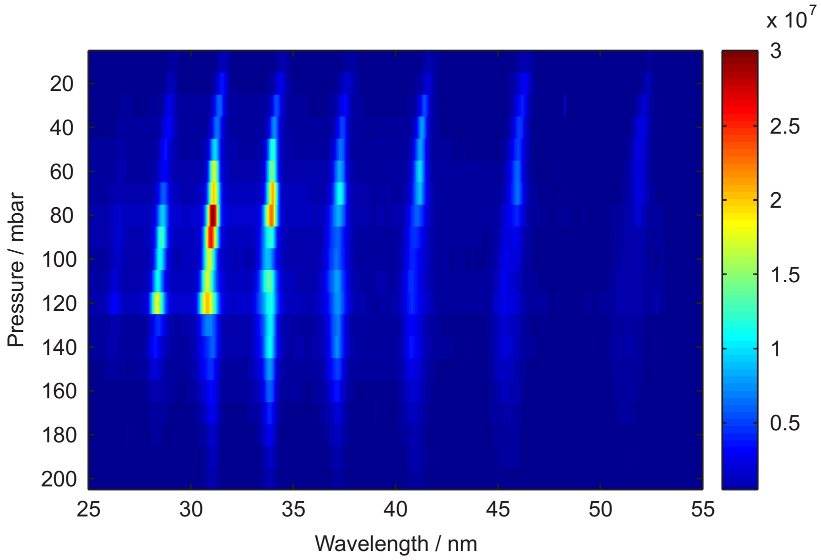

Figure 4.24: The high harmonic spectrum of argon as a function of pressure, for a 40 fs, 600 μJ input pulse. The units of the colour bar are photons per pulse.

in figure 4.24. One particularly interesting feature to note is that the harmonic wavelengths shift as the pressure is changed. This blue shifting is caused by the propagation of the fundamental through the ionized argon and demonstrates that although X-ray generation may only occur from the last few millimeters of the capillary, the first few centimeters of the capillary can act as a pulse shaper and influence the harmonic spectrum that is generated. This effect is discussed in more detail in chapter 5 where it is used to produce programmable frequency shifts of the harmonic spectrum.

According to the cut-off law (equation 3.15), by increasing the laser energy coupled into the capillary, higher harmonics should be generated (figure 3.7) and at higher photon energies, there will be less reabsorption by argon. To examine this proposition, figure 4.25 shows measurements that were made of the harmonic spectrum of argon as a function of the laser energy coupled into the capillary. The solid red line indicates the contour of the highest photon energy that was observed experimentally. It is clear to

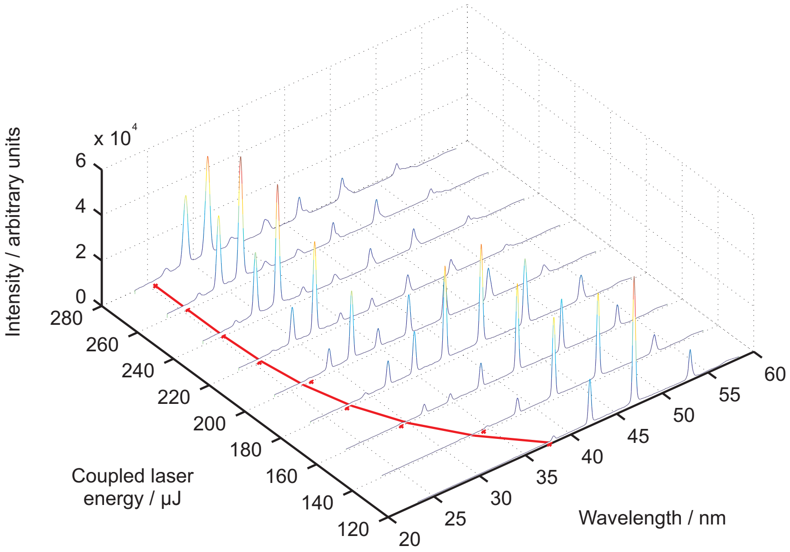

Figure 4.25: The cut-off illustrated by high harmonic spectra of argon, recorded as a function of laser energy coupled into the capillary for a 40 fs pulse. The solid red line indicates the contour of the shortest wavelength observed experimentally.

see from this that as the laser energy is increased, the maximum photon energy observed moves to higher energy. However, at coupled pulse energies above 200 μJ, a plateau is reached and no higher harmonics are observed as the laser energy is increased further. This is not predicted from the cut-off law (equation 3.15) and to explain it, we must invoke phase-matching considerations.

Figure 4.26 shows the harmonic cut-off q_c as a function of laser energy coupled into the capillary. The solid black lines represents the predicted cut-off according to the semi-classical cut-off law (equation 3.15). However, this equation takes no account of the requirements for phase-matching. In figure 4.26, the circles represent the experimental measurement of the harmonic cut-off, taken from the high harmonics spectra in figure 4.25. It is clear from figure 4.26 that the experimentally observed cut-off follows the

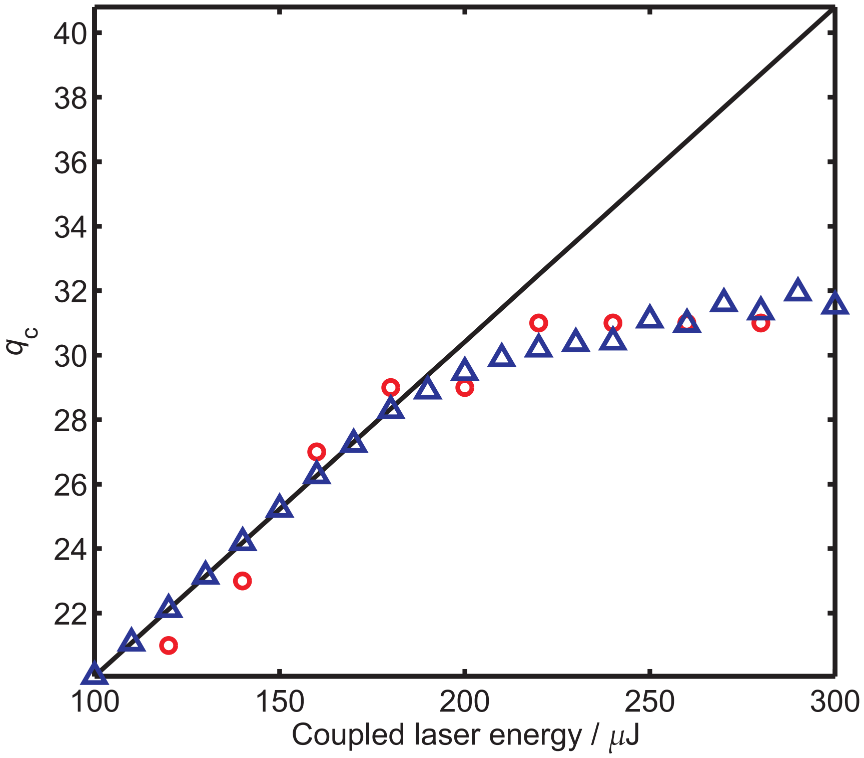

Figure 4.26: The harmonic cut-off q_c as a function of laser energy coupled into the capillary, as given by (solid line) the semi-classical cut-off law (equation 3.15), (circles) experimental measurements and (triangles) the phase-match limited cut-off.

trend of the cut-off law for laser pulse energies up to 200μJ. Beyond this the experimental data diverges from the cut-off law and rapidly saturates at the 31st harmonic.

We can model this behaviour by considering that it is not possible to effectively phase-match the harmonic generation process in argon when the ionization fraction $> 4\%$ [75] (which can be seen by referring to figure 3.15). Using the Keldysh theory, we can calculate the time at which the ionization fraction reaches 4% and hence calculate the maximum value of the field at that instant. If these values are substituted into the cut-off law (equation 3.15) then the maximum photon energy that contributes to the phase-matched process can be calculated. The results of this calculation are illustrated by the blue triangles in figure 4.26 which shows excellent agreement with the experimental data. For input laser energy < 170 μJ, the final ionization level of the pulse is $< 4\%$ and the energy of the entire pulse can potentially contribute to phase-matched generation. However, for pulses with an energy > 180 μJ, the 4% ionization level comes earlier in the pulse and hence, the pulse after this point does not contribute to the phase-matched process. As a result of this, increasing the pulse energy does not significantly increase the harmonic cut-off. Overcoming this ionization induced phase-matching limit is a challenge to scaling the high harmonic generation process to higher photon energies in a capillary. One possible solution to this problem is to use a shorter laser pulse which allows the atom to experience a higher intensity for a given ionization level (see figure 3.12). However, to achieve photon energies in the water window and into the keV energy region, a different approach is required. A technique which has shown promise in this respect is quasi-phase-matching (QPM), a technique borrowed from visible wavelength non-linear optics. Rather than completely eliminating the phase shift between the fundamental and induced harmonics, QPM periodically corrects it. In chapter 6, we discuss a phenomenon that could be exploited to perform QPM.

4.4.3 Spatial profile

Images of the spatial profile of the high harmonic beam were obtained by placing an X-ray CCD camera (Andor Technology DX434) at a distance of approximately 1 m from the output of the capillary. A 200 nm thick, pinhole free aluminium filter was placed between the capillary and camera. Images for argon pressures of 20, 40 and 80 mbar are shown in figure 4.27(a–c), respectively. The observed beam is composed of contributions from the 15th–

29th harmonics, as shown in figure 4.24. The quality of the spatial mode of the XUV is strongly dependent on the phase-matching conditions and the smallest, most uniform spot, shown in figure 4.27(c), is observed at 80 mbar where the harmonic generation process is optimally phase-matched. The radius at $1/e^2$ of the intensity of the beam at an argon pressure of 80 mbar is ~ 1 mm at a distance of 1 m from the output of the capillary. Figure 4.27(d) shows the image of a grid of known dimensions placed behind the aluminium filter. This grid was used to estimate the beam divergence, which is approximately 1 mrad at optimum phase-matching.

4.4.4 Spatio-spectral mapping

Experimental evidence for spectral variation across the spatial profile of the beam has been gathered by a novel technique that was developed within our group [128]. This technique allows us to reconstruct spatially resolved spectral information from an X-ray beam, requiring the image of only a single diffraction pattern. An example of the diffraction pattern, recorded with an X-ray CCD camera (Andor DX434) is shown in figure 4.28(a). The diffraction pattern is created by a nickel wire grid, manufactured by electrodeposition through a lithographic resist mask and consists of 38 μm wires crossing perpendicularly to form an array of 355 μm square holes. The grid is inserted into the X-ray beam, 50 cm from the exit of the capillary with a 200 nm aluminium filter to block the fundamental laser. The diffraction pattern is then recorded a further 1 m downstream.

In our group, Praeger has developed an algorithm, reported in [128], to retrieve the harmonic spectrum from each aperture in the grid. The observed Fresnel diffraction pattern is the coherent sum of all photons passing through the grid, however, the dominant contribution comes from light taking the direct path through an aperture to a point on the screen. This simplifies the retrieval by neglecting the contribution from neighbouring

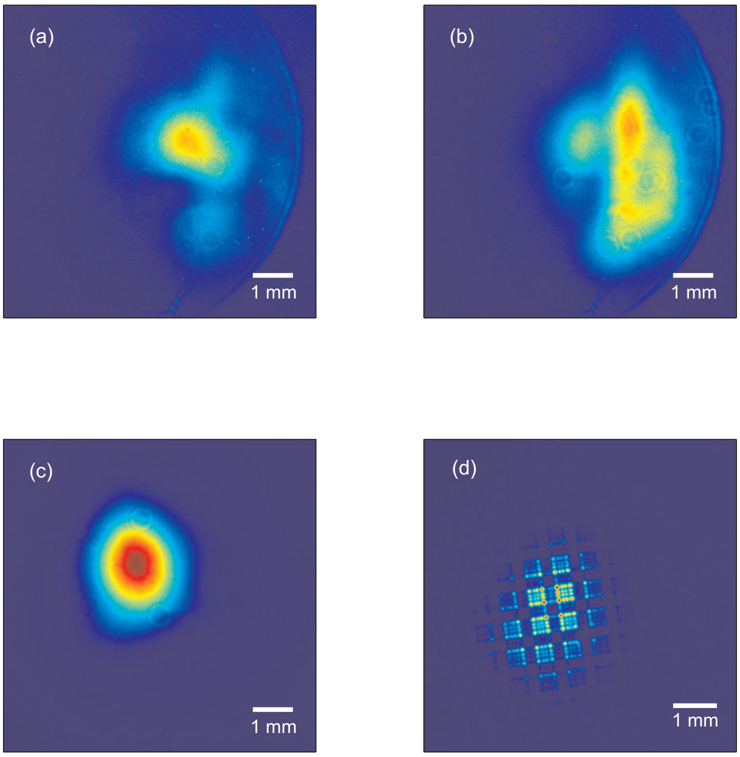

Figure 4.27: Spatial profiles of the XUV beam at (a) 20, (b) 40 and (c) 80 mbar. (d) A grid of known dimensions placed behind the filter gives an estimate of the beam divergence as ~ 1 mrad at phase matching. The edge in the top right of (a)-(c) is caused by the XUV beam clipping on a differential pumping aperture.

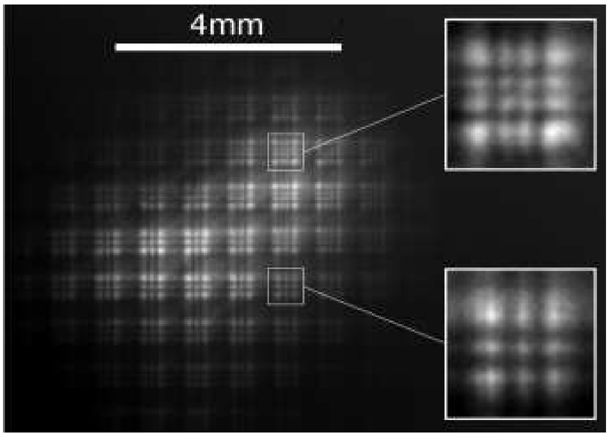

(a)

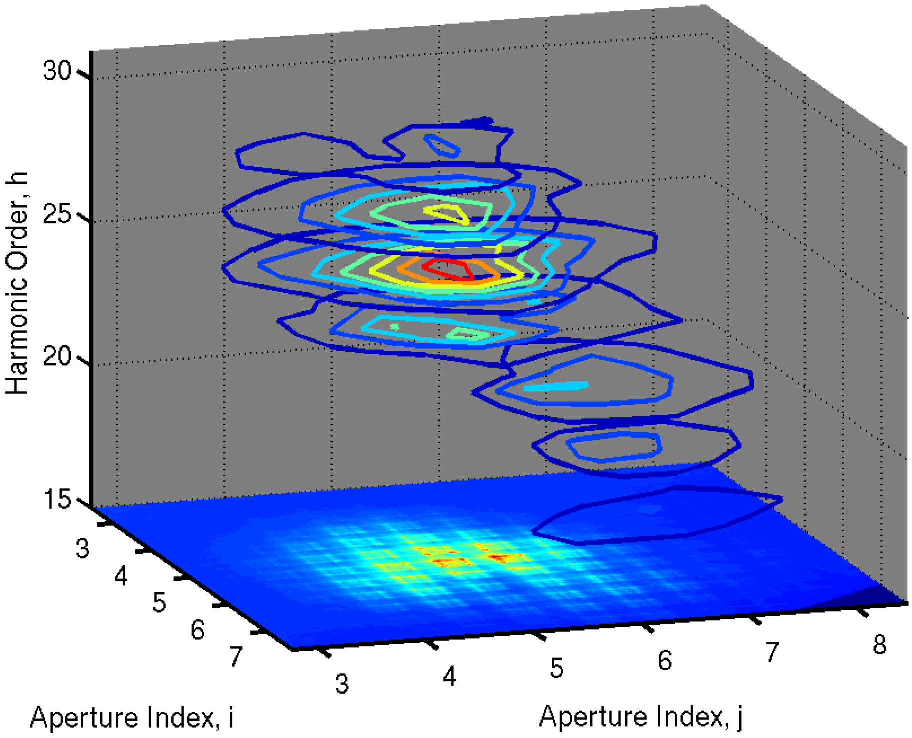

(b)

Figure 4.28: (a) Single image of the diffraction from a fine nickel mesh grid recorded at an argon pressure of 60 mbar and (inset) enlargements of two areas shows a clear difference in the diffraction pattern at different locations across the beam. (b) The reconstruction shows the spatial distribution of individual harmonics within the beam profile. The base plane shows the measured diffraction image. Taken from reference [128].

apertures and considering the diffraction pattern from each aperture separately. The harmonic nature of the beam is used to further simplify the algorithm by considering only the centre wavelength of each harmonic and in the retrieval, each diffraction pattern is calculated separately using Fresnel diffraction theory [129]. An incoherent sum may then be used to add all the diffraction patterns with a weighting factor proportional to the spectral intensity of each harmonic order. The validity of this technique has been demonstrated by comparison with the spectrum recorded with an XUV spectrometer.

An example of the reconstruction is shown in figure 4.28(b) illustrating the spatial distribution of each harmonic within the beam. As might be expected, the highest harmonics are generated towards the centre of the capillary where the laser intensity is highest. Each of the harmonics is approximately cylindrically symmetrical. The lower harmonics exist as annular profiles while the highest harmonics are round. This work is the first time that the spatial and spectral profile of capillary-generated XUV has been mapped, giving useful insight into the generation process that has been previously unavailable.

4.5 Summary

In this chapter, we have discussed in detail the experimental apparatus that has been developed for high harmonic generation and have looked in detail at the spectral and spatial properties of the beam. These results illustrate the critical role phase-matching plays in all aspects of the harmonic generation process and show that spatial and temporal variations of the laser intensity must be considered for a complete understanding of the process. In the next chapter, we will look in further detail at the role ionization plays in the high harmonic generation process.

Chapter 5

Ionization induced effects in a capillary

5.1 Introduction

In the previous chapter, we observed that an increase in the argon pressure was accompanied by a blue shift in the harmonic frequencies. In this chapter, which is partly based on work that was published in Optics Letters [9], it is demonstrated that it is also possible to tune the harmonic wavelengths by changing the intensity and chirp of the driving laser. A tuneable source of coherent X-rays is of significant interest for X-ray spectroscopy and resonant soft X-ray scattering experiments. The wavelength shift arises from a change in the argon ionization level and can be controlled by changing either the average intensity of the laser pulse or by varying the quadratic spectral phase. An ionization dependent blue-shift of the fundamental is observed which is directly imprinted on the harmonic wavelengths. Experiments show that the harmonic tuning is dependent on the non-linear spectral shift of the fundamental laser pulse that are due to the plasma created by ionization, rather than as a direct result of any chirp imposed on the fundamental. In gas jets, ionization induced blueshift effects have been observed and used to tune the harmonic wavelengths [130] by changing the focusing conditions into the gas jet.

The input laser pulse propagates through the gas while simultaneously ionizing it. This has a profound effect on the output X-ray frequencies, which shift in proportion to frequency shifts seen in the pump beam. After propagation through the capillary, we observe a blueshifting of the fundamental laser that is directly imprinted on the harmonics; the amount of blueshift being determined by the degree of ionization caused by the laser pulse. Since the amount of ionization depends on the peak intensity and pulse length, the amount of blueshift also varies as a function of these parameters.

In this chapter an experiment is described that directly measures the non-linear frequency shift of the fundamental laser pulse after it propagates through the capillary and correlates this to the measured tuning of the harmonic frequencies. The ionization level in the capillary is changed either by changing the average intensity of the laser pulse or by stretching the pulse by changing its quadratic spectral phase in a precise and measurable way using an acousto-optic programmable dispersive filter (Dazzler).

5.2 Experimental setup

The experimental setup for generating the high harmonics has been previously described in detail in chapter 4. The spectral phase of the laser pulses were modified in a precisely controlled manner using an acousto-optic programmable dispersive filter (AOPDF) and the laser average power was varied using a half-wave plate and polarizer placed after the amplifier. Laser pulses with energies of up to 600 μJ were coupled into a 70 mm long, 150 μm diameter hollow capillary. The fundamental laser light leaving the capillary was blocked using a 200 nm aluminium filter and the XUV spectra were recorded using the grazing incidence spectrometer and were typically averaged over 1000 X-ray pulses. A mirror can be inserted between the capillary and aluminium filter to send the fundmental pulses, after propagation through the capillary, to the FROG or a spectrometer (Ocean Optics HR4000CG) for characterisation.

5.3 Results and discussion

The wavelength of each harmonic can be tuned by changing the quadratic spectral phase or the laser intensity. Figure 5.1 shows the harmonic spectrum as a function of the quadratic spectral phase (chirp). The numerical values indicate the equivalent group delay dispersion that would produce the actual chirp introduced by the AOPDF. In figure 5.1(a), the pulse energy is kept constant at 0.6 mJ and the chirp introduced increases the pulse length, resulting in a reduction in the peak intensity from 2.9×10^{14} W cm^{-2} to 1.4×10^{14} W cm^{-2}. In figure 5.1(b), the peak intensity is kept constant at $1.15 \times ^{14}$ W cm^{-2} by adjusting the pulse energy between 0.3–0.6 mJ. In both these cases, a shift of almost 50% of the energy separation between the adjacent harmonic is observed.

In figures 5.1(a) and 5.1(b) the wavelength shift is almost symmetrical as the chirp is changed around the zero point. However, it is important to note that the direction of shift with increasing chirp is different in the two cases. In figure 5.1, at constant pulse energy the harmonics at zero chirp are seen to be blue-shifted in comparison to those produced at large values of positive and negative chirp. However, at constant peak intensity the opposite is true and the harmonics produced by the unchirped laser pulses are redshifted relative to those produced by a large input chirp.

Figure 5.2 plots the harmonic wavelength shift as a function of laser pulse chirp at constant pulse energy and for comparison, figure 5.2(b),

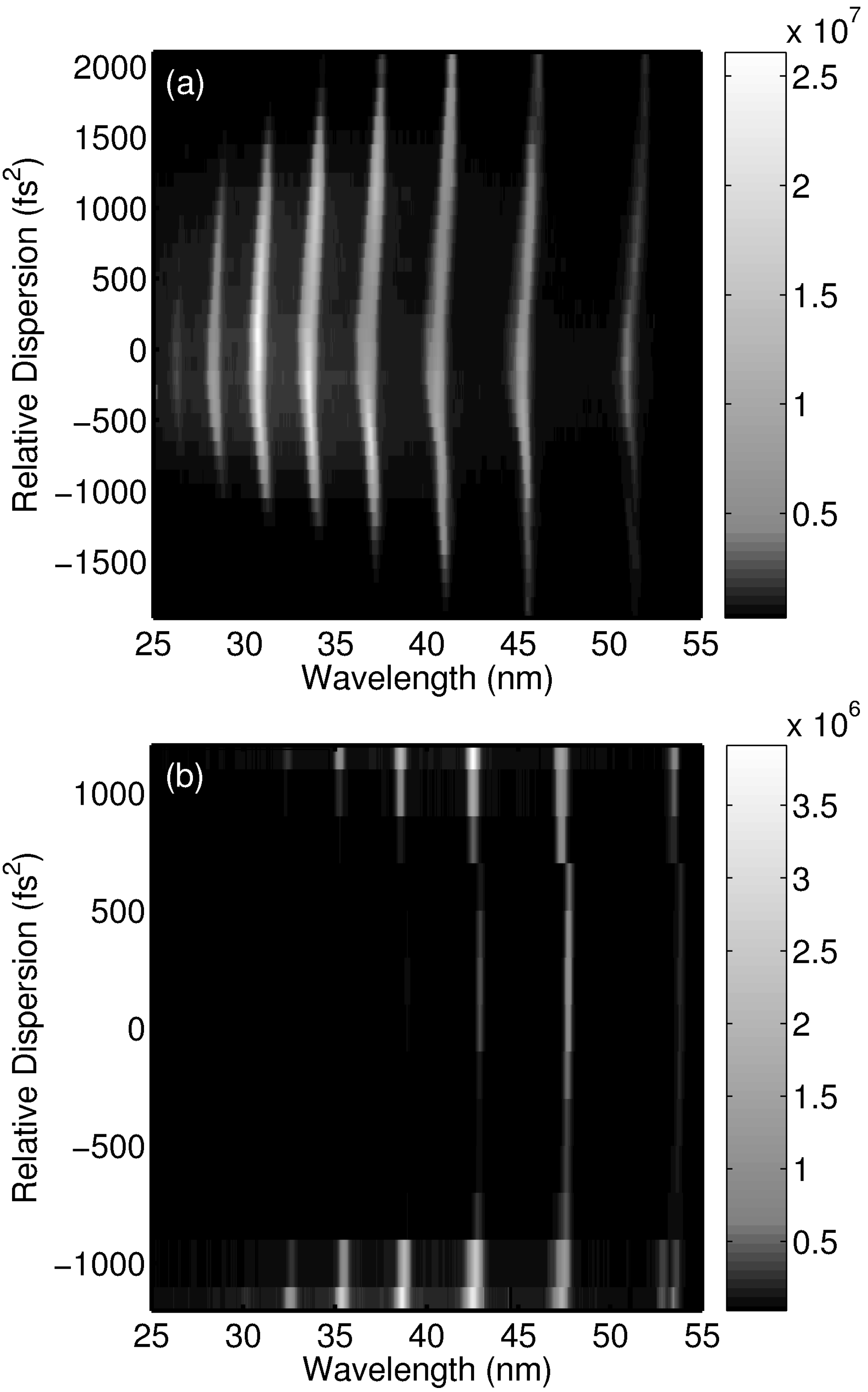

Figure 5.1: XUV spectra as a function of chirp: (a) constant laser pulse energy (0.6 mJ) and (b) constant peak intensity (1.15×10^{14} cm^{-2}). Argon pressure 60 mbar. The units of the colorbar scale are photons per pulse. Taken from reference [9].

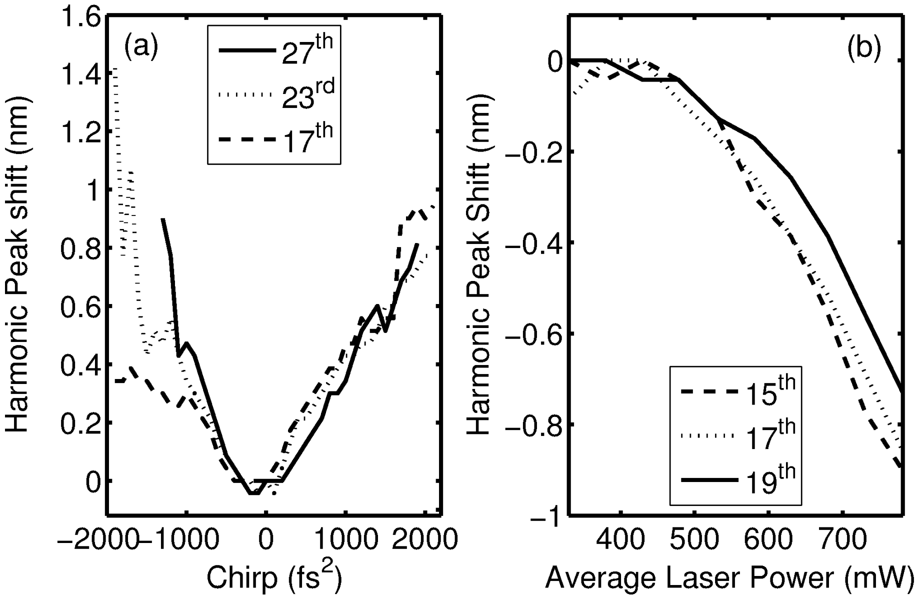

Figure 5.2: Harmonic wavelength shift as a function of (a) chirp and (b) average laser power. Taken from reference [9].

plots the shift as a function of average laser power for an unchirped pulse. Stretching the constant energy pulse by introducing chirp results in a decrease in the degree of ionization, while increasing the average power has the opposite effect, increasing the ionization and hence they have opposite effects on the sign of the wavelength shift shown in figure 5.2.

The wavelength shifts of the harmonics can be understood by examining the pre-capillary and post-capillary laser spectrum shown in figure 5.3. The pre-capillary laser spectrum is shown in figure 5.3(a), and the post-capillary laser spectrum as a function of chirp is shown in figure 5.3(b). The centre wavelength and bandwidth is calculated by gaussian curve-fitting each of these spectra, the results of which are shown in figure 5.3(c) and 5.3(d) respectively. The pre-capillary spectrum is unaffected by the applied chirp and remains at the same centre wavelenth and bandwidth throughout. However, this is not true of the post-capillary laser spectrum which is strongly affected by the chirp, resulting in a clear blueshifting of the centre

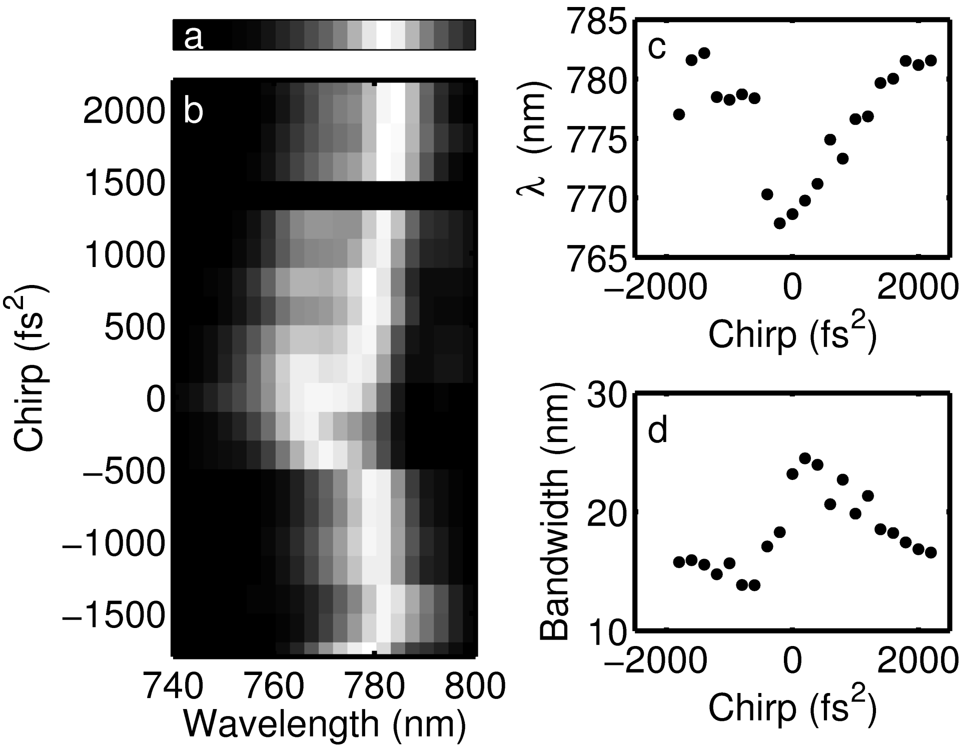

Figure 5.3: Laser spectrum (a) before and (b) after the the capillary and (c) the center wavelength and (d) bandwidth as a function of chirp.

wavelength and an increase in bandwidth for the highest peak intensity. The peak intensity drops with increasing absolute value of the chirp, implying that the blue-shifting and broadening that is observed is due to the increase in the peak power of the pulse.

The shift in the fundamental wavelength shown in figure 5.3(c) can be used to calculate the expected centre wavelengths of the harmonics according to equation 3.1, and compared to the experimentally observed shift in the harmonics. This is illustrated in figure 5.4 where there is very good agreement for the calculated and measured wavelength positions for all harmonic orders which suggests that the shift in the fundamental wavelength is directly imprinted on the harmonic spectrum. In all the results presented thus far, a constant argon pressure of 60 mbar was used, how-

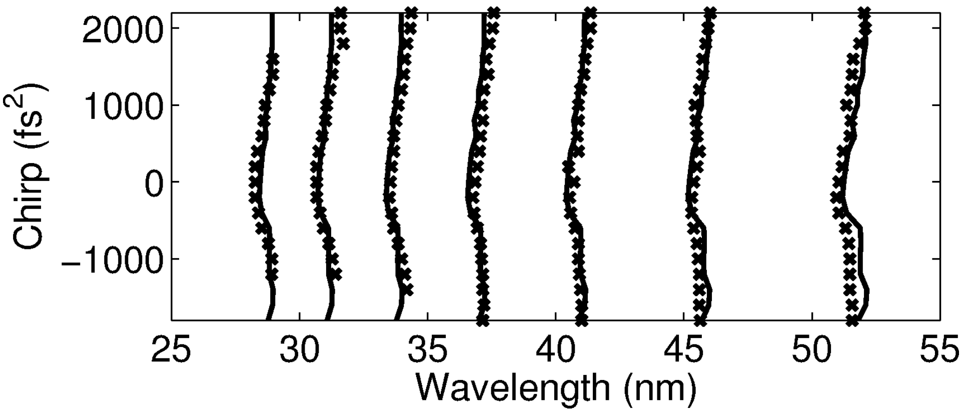

Figure 5.4: Measured (crosses) and calculated (solid line) harmonic wavelength peak position as a function of chirp.

ever blue-shifting can also be observed by increasing the argon pressure which results in an increase in the gas density and a consequent increase in the number of ionization events. Figure 5.5 shows the effect on the laser spectrum of propagation through the capillary as a function of argon pressure. The peak intensity at the centre of the capillary is 2.6×10^{14} W cm^{-2} and the final ionization level on the central axis of the capillary by the end of the pulse is approximately 50% and therefore, the trailing edge of the pulse propagates through a large amount of plasma. The plasma refractive index is a time-dependent quantity related to the evolving plasma density through the pulse. The refractive index decreases as the plasma density increases [131] and this causes a blue shift of the trailing edge of the pulse [132]. The plasma density is related directly to the gas pressure; figure 5.5 shows the output spectrum from the capillary as a function of argon pressure. From this it can be seen that blueshifting can be observed for argon pressures as low as a few tens of millibars and that an increase in the plasma density by raising the gas pressure results in further blue shift. The shift is asymmetric and predominantly to shorter wavelengths. In this way, it is very different from that observed in self-phase modulation which shows a much more symmetrical broadening about the centre

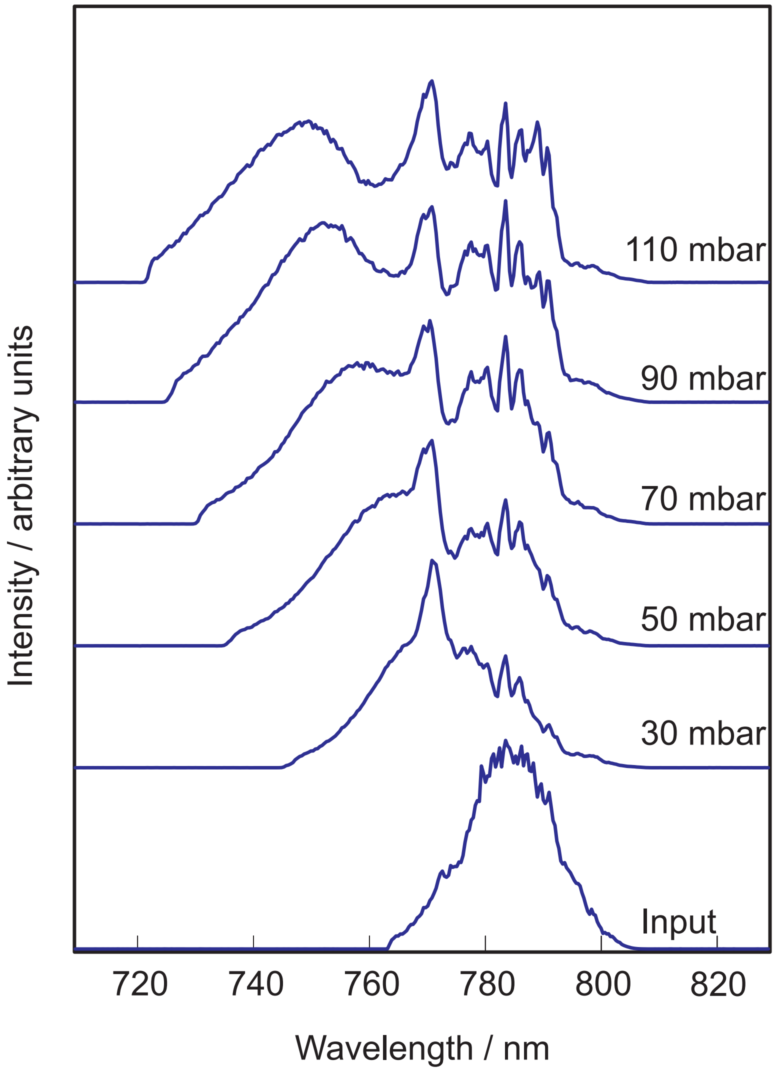

Figure 5.5: The spectrum of a 527μJ, 45 fs laser pulse after propagation through an argon filled hollow capillary at varying argon pressures, showing a distinct blue-shift with increasing pressure. The lowermost spectrum is that of the input pulse shown for comparison.

wavelength [133].

As the pump pulse propagates through the argon filled capillary, it results in harmonic generation. Argon has significant absorption in the energy region from 20–30 nm, having an absorption length of 4.6 mm for an argon pressure of 100 mbar at 25 nm and at wavelengths > 30 nm, the absorption length reduces to a few hundred micrometers. Hence, as has been seen previously in figure 4.23, X-ray generation will predominantly occur over the last few millimeters of the capillary. The pump light generating these X-rays will have travelled through almost the entire gas-filled region of the capillary, and so will be significantly blue-shifted, and will have a very similar spectrum to the pump measured after passing through the whole capillary (5.5) and the effect on the harmonic spectra is to shift all the harmonics to higher energy. Figure 5.6(a) shows the X-ray spectra generated under the same experimental conditions as figure 5.5 and for comparison, figure 5.6(b) shows the harmonic spectrum generated at lower pulse energy. From these figures it is clear that the effects of blue shifting are most evident at higher pulse energy and pressures. An additional feature seen in figure 5.6(a) that is not seen in figure 5.6(b) is significant broadening and splitting of the harmonic peaks, particularly at higher pressures. Figure 5.7 shows the effect of changing pump intensity on the structure of the X-ray spectrum at an argon pressure of 90 mbar. From figures 5.6 and 5.7, it is clear that the effect of changing pressure and peak intensity are not the same even though they both result in a change in the density of the plasma. It appears that the blueshifting, broadening and splitting are more sensitive to intensity than pressure and this may be because a change of pump intensity changes the time during the pulse at which maximum ionization occurs and the change in pressure does not.

Since we published this work, Gaarde *et al.* [134] have published a model showing that the blue-shifting predominantly occurs near the front of the

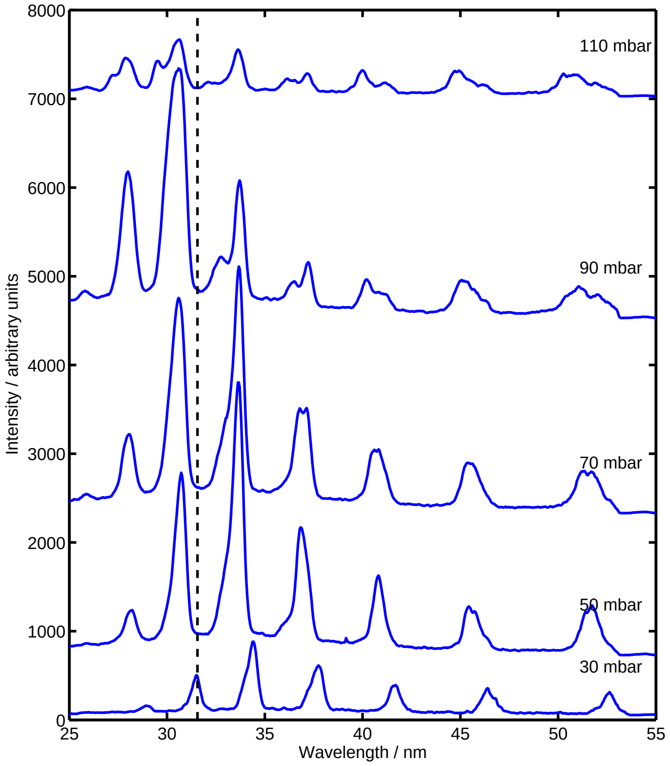

(a)

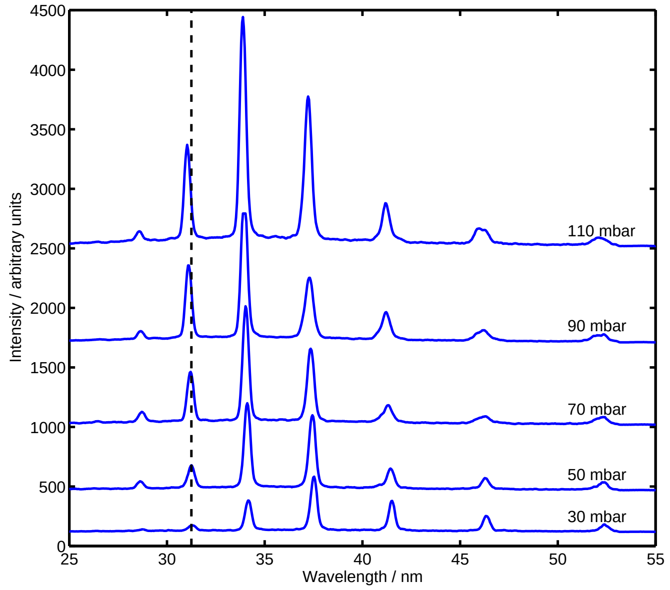

(b)

Figure 5.6: (a) The harmonic spectrum as a function of argon pressure for 45 fs pulse with 445 μJ coupled into the capillary and (b) the harmonic spectrum as a function of argon pressure for 45 fs pulse with 270 μJ coupled into the capillary

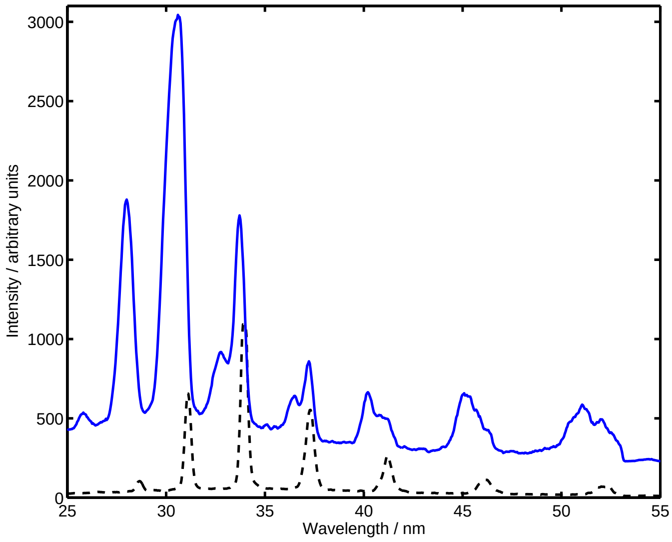

Figure 5.7: The harmonic spectrum at an argon pressure of 90 mbar for coupled laser pulse energy of (solid line) 445 μJ and (dashed line) 270 μJ to illustrate the harmonic splitting at high laser intensity.

interaction region (capillary) before depletion through ionization reduces the intensity of the laser. Their model gives evidence to support the theory that the spectral shaping and harmonic generation can occur in distinctly separate parts of the interaction region.

5.4 Summary

In this chapter we have shown that the ionization produced by the laser pulse propagating through the capillary significantly changes the spectrum of the laser pulse and generated harmonics. Both spectra are shifted to the blue, with the harmonics in this spectral region being shifted by as much as half of their spectral separation which has important applications in X-ray spectroscopy. This work has shown that ionization plays two roles in the harmonic generation process being an important component of phase-matching and influencing the spectral characteristics of the harmonics.

Chapter 6

Mode propagation in a hollow waveguide

6.1 Introduction

In previous chapters, the important role that ionization plays in the high harmonic generation process has been discussed. The fundamental can change significantly in terms of spectrum and intensity as it propagates in the waveguide as it interacts with the ionized gas. In chapter 5 it was seen that this could lead to blue-shifting, broadening and splitting of the harmonics spectrum. In this chapter, we look in more detail at ionization induced losses in the capillary and shows that the spatial distribution of ionization in the capillary may be controlled by altering the coupling conditions into the capillary. A simple model to explain the distribution of ionized argon is developed and correlated with the emission recorded experimentally. This model will prove useful in the optimization of high harmonic experiments and offer us further insight into the phase-matching process. Since completing this work, a similar study has been published by Pfeiffer and Downer [135].

6.2 Capillary modes

It is possible to create a periodic intensity variation in a hollow waveguide by exciting multiple modes in the capillary. Since each mode has a different propagation vector, the superposition of two or more capillary modes results in a beating of the intensity along the propagation axis of the capillary. For a linearly polarized TEM$_{00}$ source, only the EH$_{1m}$ modes will be excited. Figure 6.1 illustrates the intensity distribution in the EH$_{11}$ and EH$_{12}$ modes. Marcatili and Schmeltzer [93] derived expressions for the electric field of the EH$_{1m}$ waveguide modes which, in polar co-ordinates, are given by

$$\begin{aligned} E_{r1m} &= J_0\left(u_1m\frac{r}{a}\right)\cos(n\theta)\cdot\exp\left[i(\gamma z-\omega t)\right], && (6.1)\\ E_{\theta 1m} &= J_0\left(u_1m\frac{r}{a}\right)\sin(n\theta)\cdot\exp\left[i(\gamma z-\omega t)\right], && (6.2)\end{aligned}$$

where a is the waveguide radius, J_0 is the zero-order Bessel function of the first kind; where u_{1m} is given by the solution to the equation $J_0(u_{1m}) = 0$. The complex propagation constant γ is given by

$$\gamma = k\left[1-\frac{1}{2}\left(\frac{u_{1m}\lambda}{2\pi a}\right)^2\left(1-\frac{i(v^2+1)}{2\pi a\sqrt{v^2-1}}\right)\right], \tag{6.3}$$

where $k = 2\pi/\lambda$, u_{1m} is the m^{th} root of the Bessel function of the first kind J_0 and v is the complex refractive index. The imaginary part of equation 6.3 represents attenuation of the light propagating in the waveguide and the real part the phase. Since each capillary mode has a different propagation vector, a superposition of these modes will exhibit a beating along the propagation axis. The beat length L between two modes is given by

$$L = \frac{2\pi}{\Delta_k}, \tag{6.4}$$

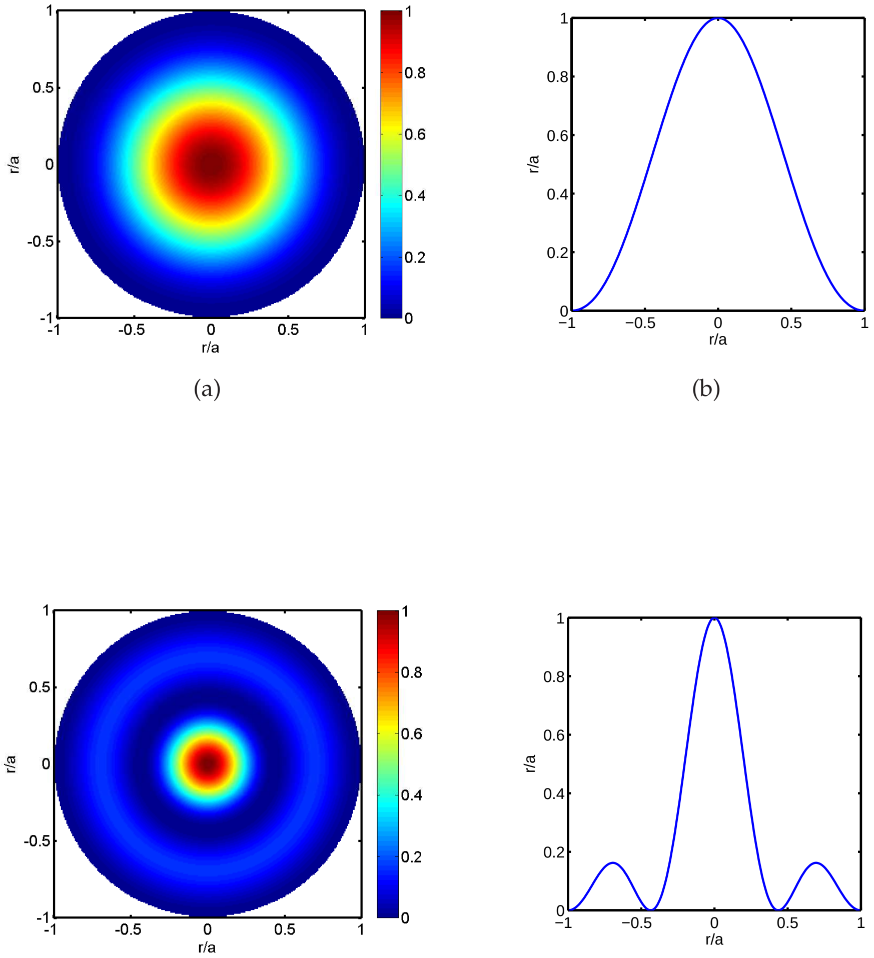

(a) (b)

(c) (d)

Figure 6.1: Intensity distribution of the (a-b) EH11 and (c-d) EH12 capillary modes, normalized to maximum intensity.

where Δ_k is the difference in the wave vectors of the two capillary modes, which for the EH$_{11}$ and EH$_{12}$ modes is given by

$$\Delta_k = \frac{\lambda}{4\pi a^2}\left[u_{12}^2 - u_{11}^2\right]. \tag{6.5}$$

It is fairly straightforward to create a superposition of the two lowest order capillary modes and can be achieved by tailoring the size of the laser's beam waist at the entrance to the capillary. The coupling efficiency of an incident gaussian beam to each of the EH$_{1m}$ capillary modes can be calculated by the overlap integral [120]

$$\eta = \frac{[\int_0^a \exp(-r^2/\omega^2) J_0\left(u_m \frac{r}{a}\right) r \,\mathrm{d}r]^2}{\int_0^\infty \exp(-2r^2/\omega^2) r \,\mathrm{d}r \; \int_0^a J_0^2\left(u_m \frac{r}{a}\right) r \; dr.} \tag{6.6}$$

In chapter 4.3.1 we discussed the focusing conditions necessary for optimum coupling into the EH$_{11}$ mode. In most capillary-based high harmonic generation experiments the intention is to couple the maximum energy into the lowest order EH$_{11}$ mode because the higher order modes are more lossy. We review these conditions again here and compare these to the conditions necessary to couple to a superposition of capillary modes. It can be seen from figure 6.2 that the optimum condition for coupling into the EH$_{11}$ mode is given by $\omega = 0.64a$, where ω is the radius at $1/e^2$ of the intensity of the beam. At this point, 98% of the power is coupled into the EH$_{11}$ mode. If a different spot size is chosen, in particular a smaller spot size, higher order modes will be excited, for example, most efficient coupling into the EH$_{12}$ mode may be achieved for a waist size to bore ratio of $\omega/a = 0.26$, with 42% of the power coupled into the EH$_{12}$ mode.

Figure 6.3(a) shows the radial intensity in a 75 μm radius, 70 mm long capillary, plotted as a function of position along the capillary. The beam-waist-to-bore-ratio $\omega/a = 0.64$ at the entrance of the capillary, which equates to optimum coupling into the EH$_{11}$ mode. Figure 6.3(b) shows the radial

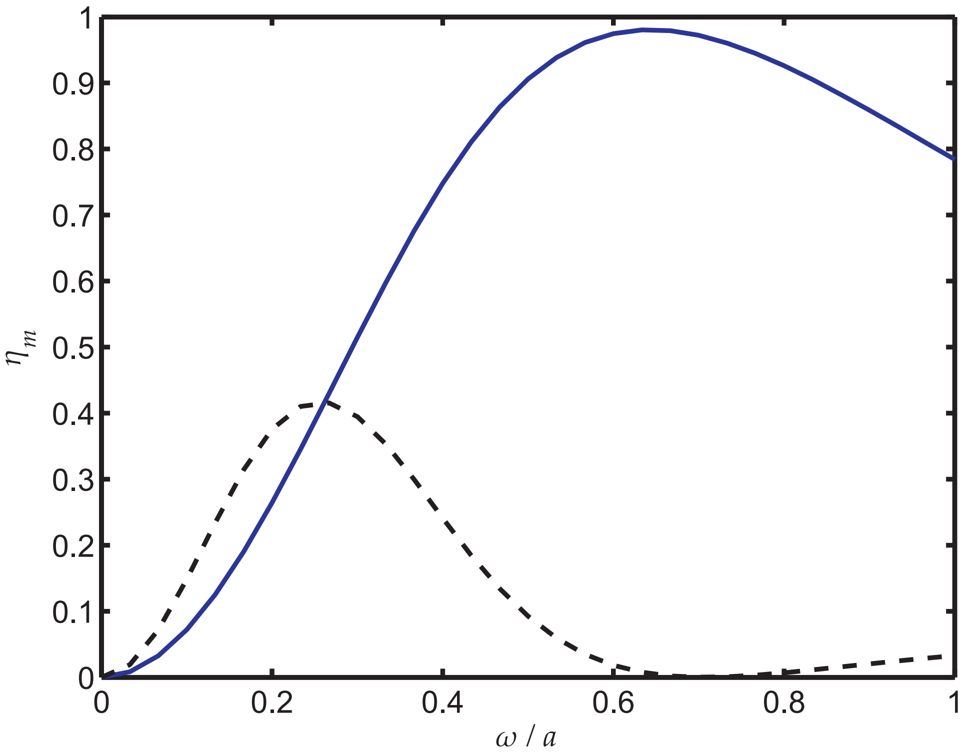

Figure 6.2: Calculated coupling efficiency η of a TEM$_{00}$ beam into (solid line) EH$_{11}$ and (dotted line) EH$_{12}$ modes.

intensity for a superposition of equal proportions of the EH$_{11}$ and EH$_{12}$ modes

$$I(r) = |\mathbf{E}_{11}(r) + \mathbf{E}_{12}(r)|^2, \tag{6.7}$$

where the beam waist to bore ratio $\omega/a = 0.26$, giving optimum coupling into the EH$_{12}$ mode. Constructive interference between the two modes results in a narrow spatial profile which increases the peak intensity. As the beam propagates, the modes acquire a π-phase shift with respect to one another which corresponds to the destructive interference case. In the case of mixing equal proportions of the EH$_{11}$ and EH$_{12}$ modes, the intensity at the centre of the capillary will be zero and the intensity forms a toroidal profile towards the edges of the capillary. The intensity continues to oscillate between these two extremes, resulting in a period intensity modulation along

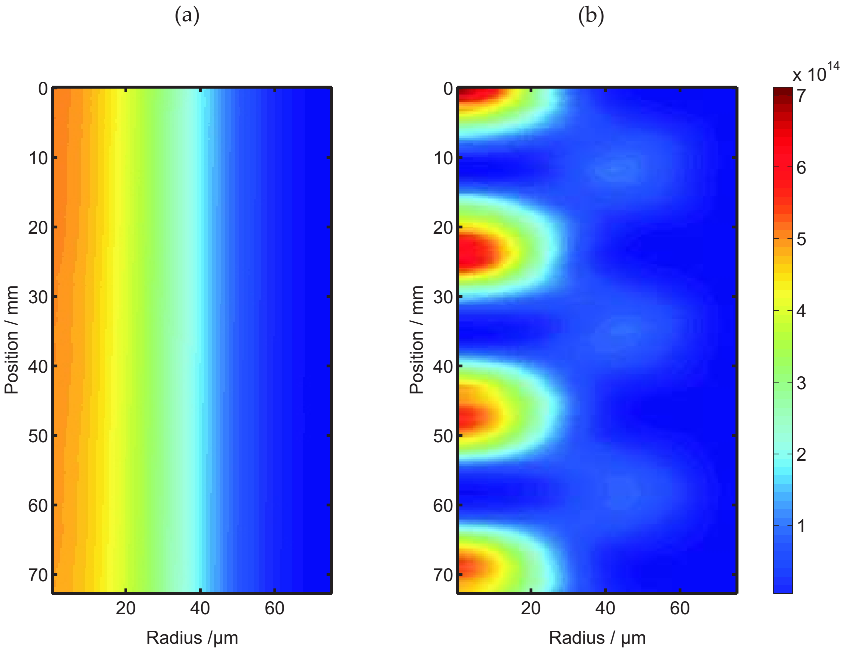

Figure 6.3: Radial intensity distribution of the (a) EH11 compared with (b) a superposition of equal proportions of the EH11 and EH12 modes. The colour map scale is in W cm^{-2} and the plots are normalized by the integrated power.

the propagation axis of the capillary.

6.3 Experimental

The experimental apparatus has been described in detail in chapter 4. Figure 6.4 shows a photograph of the capillary and T-piece arrangement. A 40 fs laser pulse at 1kHz repetition rate was coupled into the capillary using a 0.7 m plano-convex lens. The beam-waist-to-bore ratio of this beam is estimated to be ~ 0.58. The input pulse energy was controlled between 500–840 μJ by inserting reflective neutral density filters into the beam. The coupling efficiency was typically $\sim 45\%$. The visible emission from the ionized argon was characterized using an Acton 300i spectrometer and fig-

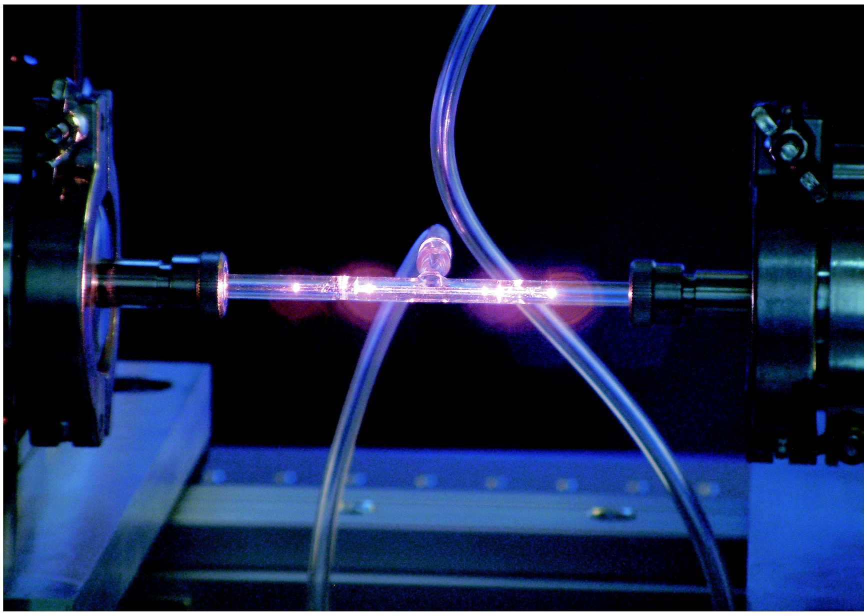

Figure 6.4: Photograph of the T-piece and capillary.

ure 6.5 shows the argon emission spectrum recorded between 400 nm and 580 nm. A 600 nm short band pass interference filter with optical density 3 at the laser wavelength (CVI Technical Optics) was used to attenuate the laser, in combination with a 488 nm or 550 nm narrow band pass filter (10 nm FWHM) to select intense lines corresponding to emission from singly ionized argon or neutral argon respectively [136]. The plasma emission from the side of the capillary was imaged onto a CCD camera (Princeton Instruments Pixis 400) placed parallel to the axis of the capillary.

6.4 Results

Figure 6.6 shows the emission from singly ionized argon using the 488 nm bandpass filter. The observed emission is integrated across the diameter of the capillary and plotted as a function of the position along the capillary axis for argon pressures between 0–200 mbar. Bright and dark fringes are

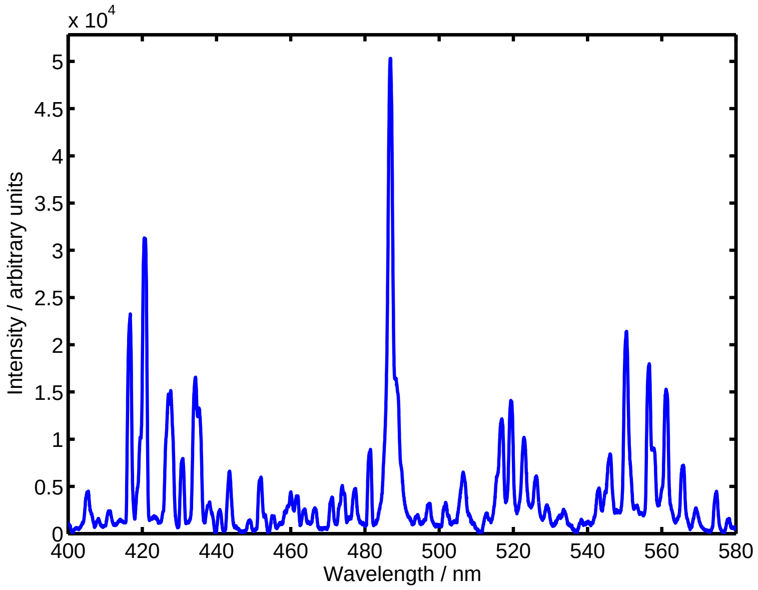

Figure 6.5: Argon emission spectrum

observed along the capillary axis as predicted from figure 6.3. For a 150 μm capillary and a superposition of only the EH_{11} and EH_{12} modes, we would expect a beat length of 23.1 mm. The beat pattern observed experimentally is more complicated and less symmetrical than that predicted in figure 6.3 which can be attributed to contributions from higher order modes which have shorter beat lengths, for example, the EH_{12} and EH_{13} modes have a beat length of 12.8 mm. The emission is shown for a 40 fs pulse for four different pulse energies and is normalized to the maximum signal (from the 840 μJ data). It can be seen that with increasing pulse energy the drop off in intensity of the emission along the capillary axis is more pronounced which can be explained by an increase in the ionization induced loss. Figure 6.10

shows the emission from neutral argon using a 550 nm band pass filter as a function of pressure and position along the capillary axis. Again, bright and dark fringes are observed along the axis of the capillary which are a result of beating between the capillary modes. The beat lengths are sim-

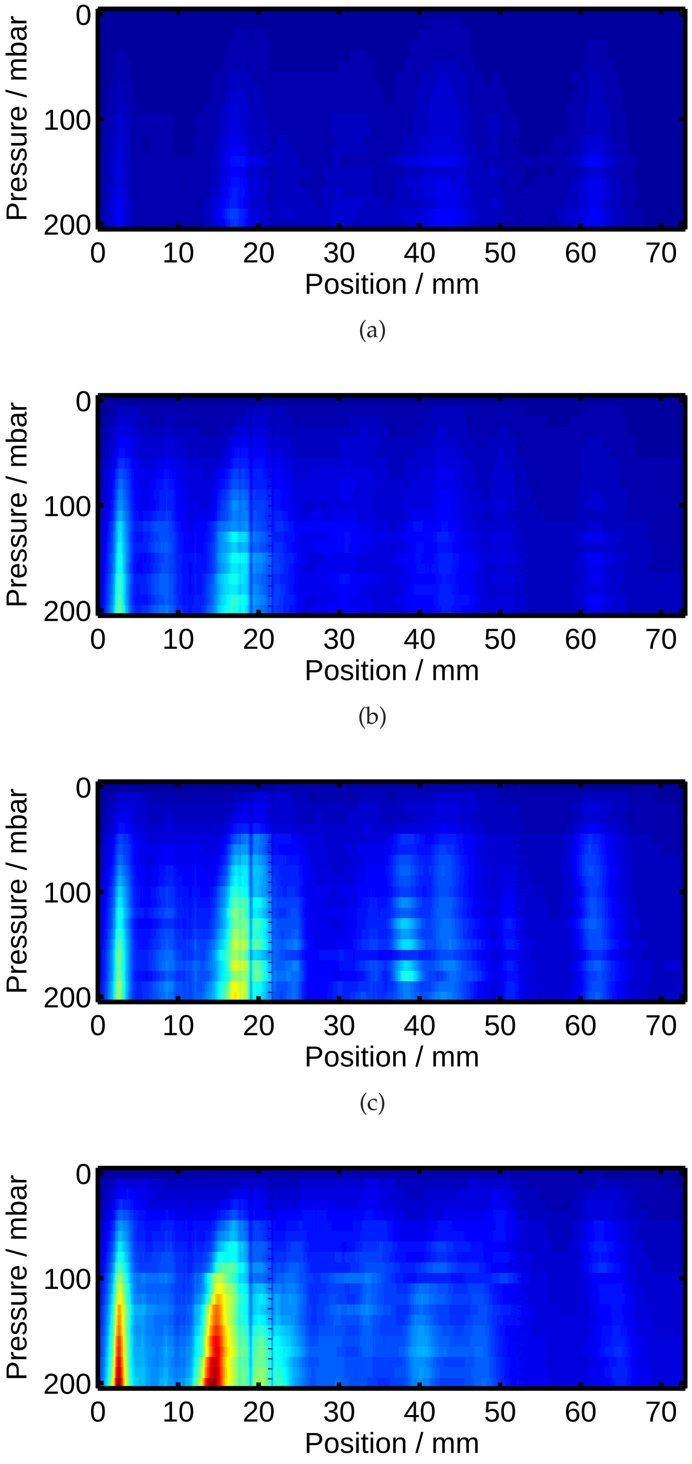

(a)

(b)

(c)

(d)

Figure 6.6: Experimentally measured beating pattern of singly ionized argon (488 nm line) for (a) 572 μJ, (b) 707 μJ,(c) 777 μJ and (d) 840 μJ,

ilar to figure 6.6 and shorter that theoretically predicted which again can be attributed to the presence of higher order modes. The interesting difference to note between these two data sets is that the neutral argon does not show such a pronounced reduction in intensity along the axis of the capillary. More energy will be required to form ionized argon and therefore the emission from the ionized argon will be more sensitive to laser intensity than the emission from neutral argon.

6.5 Simulation

To aid in the understanding of the experimental results a simple model has been developed to model the propagation and ionization in the capillary. The simulation proceeds by defining a gaussian input beam with arbitrary beam waist and calculates the coupling efficiency into each of the waveguide modes from equation 6.6. Each mode is independently propagated a short distance Δz along the longitudinal axis of the capillary, using equation 6.3 to account for the phase advance and attenuation losses of each of the modes. The new spatial profile of each mode is calculated from equation 6.1 and 6.2, and the intensity calculated by a weighted sum of the appropriate contribution A_m from each of the m waveguide modes,

$$I(r,z) = I_0(z)\left|\sum_c A_m \mathbf{E}_{1m}(r,z)\right|^2, \tag{6.8}$$

where I_0 is the peak intensity. As the pulse propagates, it ionizes the gas in the capillary resulting in a decrease in the laser energy. The ionization rate can be calculated from Keldysh theory, integrating the rate over time according to equation 3.10 to find the fraction of atoms η ionized. The energy

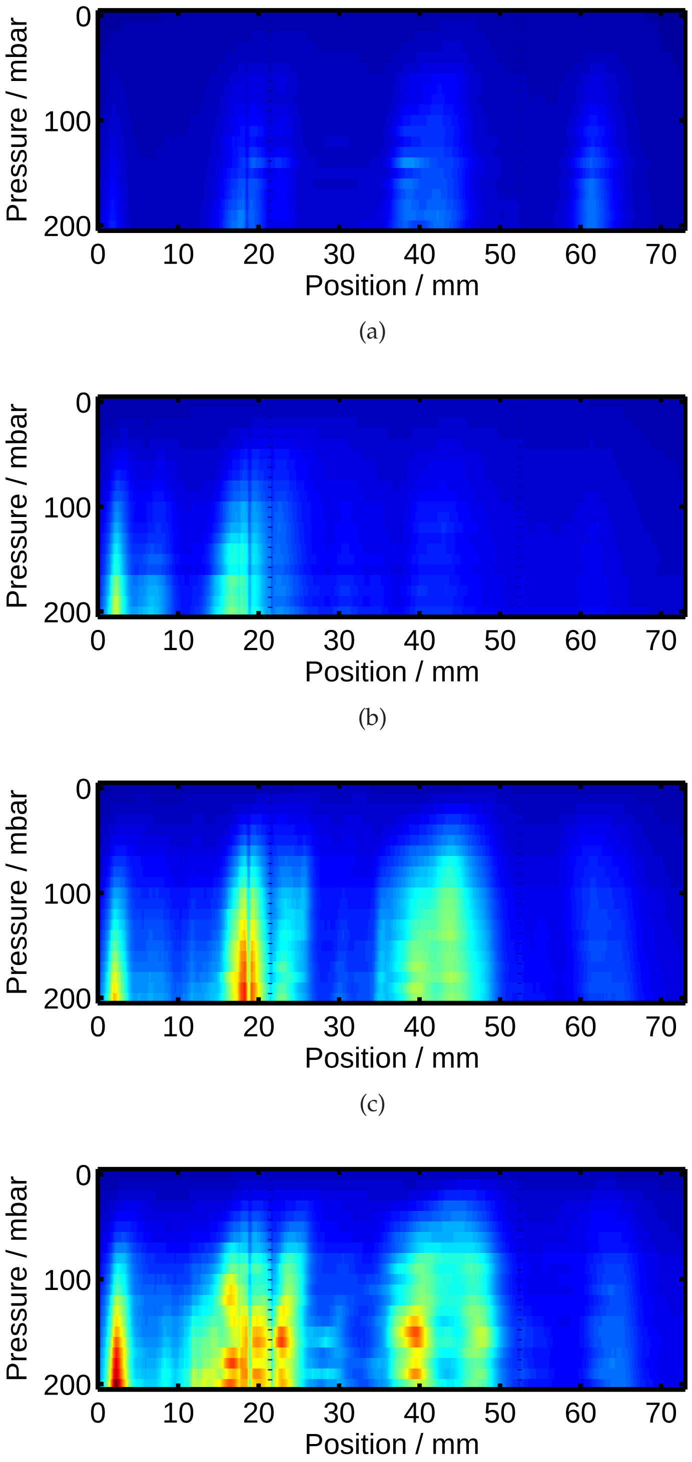

(a)

(b)

(c)

(d)

Figure 6.7: Experimentally measured beating pattern of neutral argon (550 nm line) for (a) 572 μJ, (b) 707 μJ,(c) 777 μJ and (d) 840 μJ,

loss can then be calculated according to,

$$E_I = NI_p e\eta, \tag{6.9}$$

where I_p is the ionization potential of the atom in electron volts, e is the charge on the electron and N is the number of atoms in a ring-shaped volume element, given by

$$N(r, z) = 2\pi r \Delta r \Delta z P N_{atm}, \tag{6.10}$$

where r is the radius of the capillary, Δr is a small step across the capillary's radius, Δz is a small step along the capillary's longitudinal axis, P is the pressure in bar and $\mathrm{N_{atm}}$ is the number density at one bar. The pressure is calculated from a fit to the fluid-dynamics model data shown in chapter 4. This model can be used to describe the ionization induced energy loss as a function of pressure in the capillary. Figure 6.8 shows the theoretical calculation compared to experimental data

Figure 6.9 shows the theoretical prediction of the total number of atoms ionized which is proportional to emission, plotted as a function of argon pressure and axial position along the capillary. The theoretical model uses the same laser parameters as the experiment and includes the $\mathrm{EH_{11}}$ and $\mathrm{EH_{12}}$ modes. There is a reasonable match between theory and experiment clearly showing a beating between the first two capillary modes. The theoretical model shows the drop in emission intensity along the capillary axis as a result of ionization induced losses. The beat length in the model corresponds to the prediction of $\sim$ 23 mm for the $\mathrm{EH_{11}}$ and $\mathrm{EH_{12}}$ modes. The offset of the first beat observed between the experimentally measured results and the theoretical prediction can be explained by introducing an offset in the focusing conditions into the capillary. If the waist of the beam is not placed at the entrance to the capillary, a curved wavefront is coupled

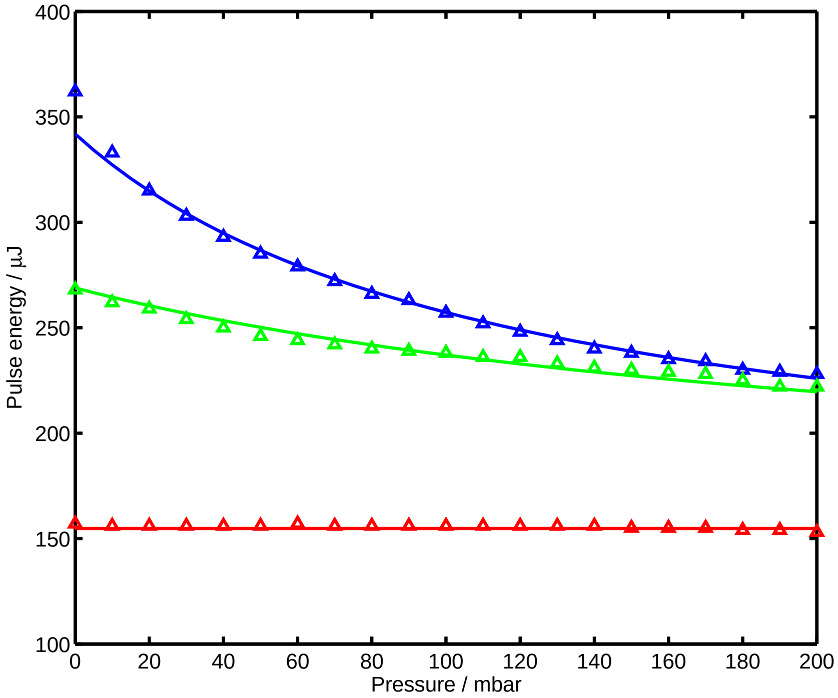

Figure 6.8: Output energy from capillary as a function of argon pressure for 40 fs pulses with energies (a) 777 μJ (b) 572 μJ and (c) 373 μJ.

to the capillary which alters the phase of the coupled capillary modes at the input. Figure 6.10 shows the beating pattern calculated when modes up to the EH_{14} mode are accounted for and it be seen that the intensity pattern becomes more complicated as a result of interference between the large number of modes.

6.6 Summary

In this chapter we have shown that the position of the argon plasma can be manipulated by controlling the coupling into the waveguide. Imaging the plasma emission has a number of interesting applications, including being a sensitive test for alignment where the axial offset of the first beat can be

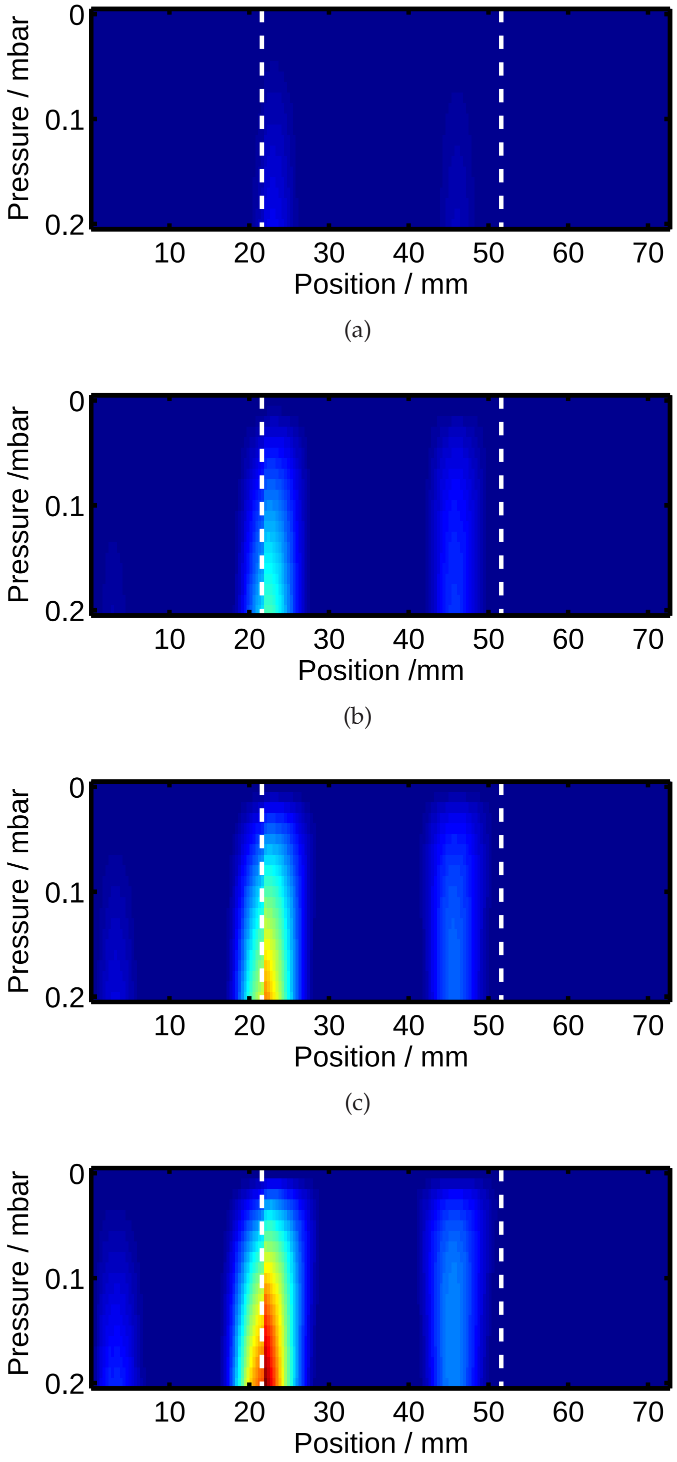

(a)

(b)

(c)

(d)

Figure 6.9: Theoretically calculated beating pattern of singly ionized argon for a 40 fs laser pulse with input pulse energy of (a) 572 μJ, (b) 707 μJ,(c) 777 μJ and (d) 840 μJ. The vertical lines indicate the position of the gas inlet holes.

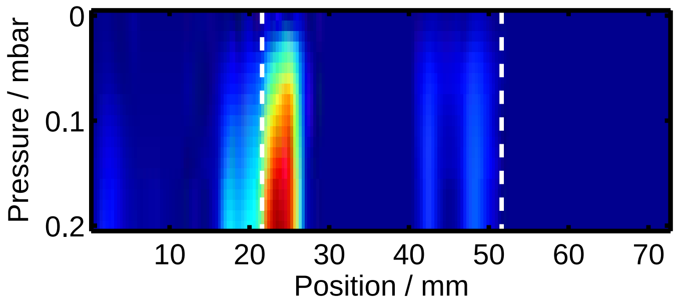

Figure 6.10: Theoretically calculated beating pattern of singly ionized argon (488 nm line) for 840 μJ, 40 fs pulse consisting of 77% EH_{11}, 12% EH_{12}, 8% EH_{13} and 4% EH_{14}.

used to confirm where the focal position of the laser is with respect to the entrance of the capillary.

Further work needs to be done to understand the mechanism of production of the emission from the plasma. If we can correlate the plasma emission to X-ray emission we can use this knowledge to design more intelligent pressure profiles by micro-machining patterns of holes into the capillary. For example, a capillary where multiple holes are placed between the gas inlet hole and the end of the capillary, can create a top hat pressure profile, eliminating the pressure gradient at either end of the capillary and limiting the reabsorption by the argon. Alternatively, placing a single gas inlet hole at the location of the first mode beat should enhance the generation while minimizing the reabsorption by the argon. Further modelling needs to be undertaken to examine the proposition.

Another idea that has been suggested recently [137] is to use the technique to achieve photon energies in the water window and into the kiloelectron volt energy range using a capillary waveguide. The high laser intensities that are required produce levels of ionization in the capillary that make the phase-matching techniques discussed previously ineffective and a different approach to phase-matching is required. A technique which has shown promise is quasi-phase-matching (QPM), a technique borrowed from visible wavelength non-linear optics. Rather than completely eliminating the phase shift between the fundamental and induced harmonics, QPM periodically corrects it. A novel scheme by Gibson *et al.* demonstrated the principle of QPM to generate harmonics in the water window, by periodically modulating the diameter of the waveguide to create an intensity modulation [138]. However such waveguides, by their nature, have a fixed modulation period and are relatively difficult to make; it would be extremely attractive to be able to tune the period to optimize the process, possibly allowing the selection of a particular harmonic. To achieve this, a beat length that is less than the coherence length of the harmonic generation process is required which requires either a much smaller diameter capillary or a superposition of very high order modes. Selective excitation of higher order capillary modes can be achieved by shaping the phase profile of the input beam; a spatial light modulator has recently been used by Pfeifer *et al.* to excite specific fibre modes in a hollow waveguide [4]. This chapter has demonstrated a method of modulating the intensity in a capillary without physically modifying the capillary. The success of this scheme will depend on the effect of non-linear mode mixing in the capillary. To extend the harmonic cut-off sufficiently to generate high harmonics into the water window, a high intensity pump will be required which will result in a high plasma density in the capillary. This plasma may result in the desired mode beating pattern being destroyed by non-linear mode mixing as a result of self-focusing and de-focusing in the capillary; further work will be required to understand the role of mode-mixing.

Chapter 7

Focusing X-rays

7.1 Introduction

The high harmonic source, described in detail in chapter 4, emits a low divergence (< 1 mrad) beam which can be directly applied to scattering, spectroscopy or fluorescence experiments with no further focusing. However, the beam size at the sample is currently > 1 mm and this limits us to fairly large, millimeter sized samples containing many atoms, molecules or nanoparticles. To extend the applicability of the source to small samples, from 10 nm to 100 μm in size and towards the single molecule regime, it becomes advantageous to focus the X-ray source. This overcomes the decrease in solid angle of the X-ray source as the sample size decreases relative to the beam [139] and allows us to achieve very high X-ray intensities at the sample, reducing the exposure time required and potentially allowing single shot experiments and time-resolved measurements. In addition, a micro-focused source offers the possibility of high spatial resolution X-ray microscopy where a resolution down to 15 nm can be achieved using zone plate lenses [140], and since the XUV photon energy is well matched to the K and L-edges of many elements (see chapter 1) the differential absorption provides a natural contrast for elemental mapping, such as mapping calcium concentrations in bone [141] or for chemical bond mapping by scanning across the absorption edges where the XANES (X-ray Absorption Near-Edge Structure) resonances allow different bonding states of the element to be identified [142].

This chapter begins with a discussion of the refractive index at X-ray wavelengths, which can be used to explore the effects of wave propagation, reflection and refraction at XUV wavelength. These concepts need to be fully understood in order to design XUV optics. The phenomenon of total external reflection will be obtained from this theory, which is used as the basis of the tapered capillary optics that have been developed for focusing the X-rays from our high harmonic source. A detailed ray-tracing model was developed and the theoretical results from this are compared with the experimental results obtained from the tapered capillaries that were fabricated. It is shown that the feedback from these comparisons will allow intelligent design of the next-generation of fibre tapers.

7.2 X-ray interactions with matter

In the XUV region, the primary interactions with matter are photoabsorption and Rayleigh scattering. At an atomic level, these phenomena are accurately described using the complex atomic scattering factor [14]

$$f = f^{'} - if^{''}, \tag{7.1}$$

which is the factor by which one must multiply the amplitude scattered by a single free electron to yield the total amplitude coherently scattered by a particular atom. It is assumed that the individual atoms scatter independently and therefore that the interaction of X-rays with condensed matter may be calculated by summing the interaction over the individual elements, that is, it is assumed that the scattering is unperturbed by the condensed state of the system. This assumption breaks down for energies near the absorption edges where the specific chemical state is important and direct experimental measurements must be made [14].

The atomic scattering factors are based upon a combination of experimental measurements and theoretical calculations. Numerous compilations of data exist, with one of the most complete being provided by Henke *et al.* [14], an up-to-date version of which is maintained by Gullikson [96]. This data includes values for $f^{'}$ and $f^{''}$ for all elements from hydrogen to uranium, and for photon energies from 40 eV to 30 keV.

The experimental measurements primarily comprise of photoabsorption measurements made from thin films or gases of the element [14, 143] which gives direct access to the imaginary part of the atomic scattering factors allowing the real part to be calculated through Kramers-Kronig relations [12, 14, 143]. Alternatively, angle-dependant reflectance measurements can be made and the atomic scattering factors determined through least-squares fitting of the Fresnel equations [144,145]. It is also possible to make direct measurements of the real part of the atomic scattering factors with careful interferometric measurements [146,147]. Elements such as carbon [144], silicon [144,145,148], molybdenum [144,149], tungsten [144] and aluminium [148] which are of technological importance in areas such as multilayered mirror coatings and filters have been studied in detail and a wide amount of carefully measured data exists. For other elements there is little or no published experimental data making it necessary to rely heavily on theoretical calculations and extrapolations across Z [96].

7.2.1 X-ray refractive index

It is possible to describe the optical properties of X-rays interacting with a condensed matter system by familiar optical constants, such as the complex refractive index, n, which can be derived from the atomic scattering factors.

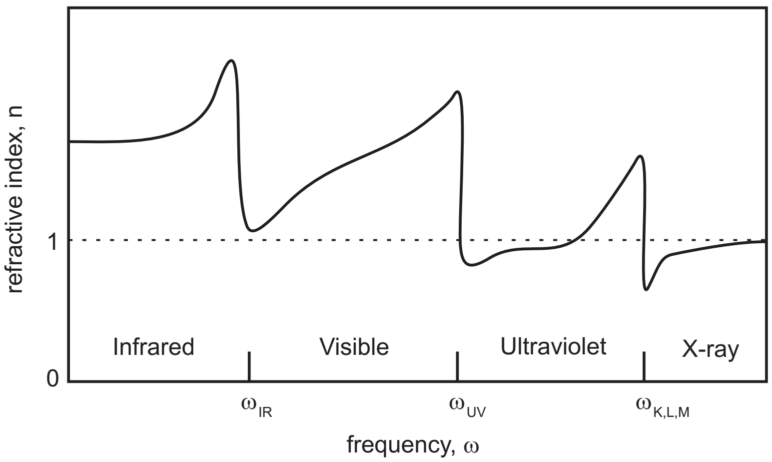

Figure 7.1: The refractive index shows strong variations near the infrared, ultraviolet and X-ray resonances. At short wavelengths, far above all atomic resonances, the refractive index tends towards unity. (Adapted from reference [119].)

The refractive index of a medium shows a strong frequency dependance, especially near the resonant frequencies ω, this is shown schematically in figure 7.1 [119]. As a result, waves of different frequencies propagate at different phase velocities. For visible light, where the frequency $\omega < \omega_{\mathrm{UV}}$, the refractive index of a medium is greater than unity, and typically ~ 1.5 for many transparent materials. A consequence of the low phase velocity propagation in the visible are the common phenomena of reflection and refraction at angled interfaces, focusing by lenses, and total internal reflection [12].

However, in the XUV region we are operating at energies greater than the atomic resonances and the refractive index is slightly less than unity. This gives rise to the interesting phenomenon of *total external reflection*, which we will exploit to create X-ray focusing optics, whereby reflection at glancing incidence occur with little or no absorption loss. Total external reflection is discussed in detail in section 7.2.3.

Since the refractive index deviates from unity by only a small amount, it is common to write it in the following form:

$$n = 1 - \delta + i\beta, \tag{7.2}$$

where δ and β are small values close to zero which describe the refractive index decrement and the attenuation coefficient of the medium respectively [12]. The refractive index n for a homogeneous material of density ρ, consisting of N elements with weight fractions w_q irradiated with light of wavelength λ may be calculated from its relation to the atomic scattering factors by the expression

$$n = 1 - \delta + i\beta = 1 - \frac{N_A r_e \rho \lambda^2}{2\pi} \sum_{q=1}^{N} \frac{w_q}{A_q} f_q, \tag{7.3}$$

where N_A is Avagadro's number, $r_e = e^2/4\pi\epsilon_0 mc^2$ is the classical electron radius, h is Planck's constant, c is the velocity of light, A_q is the atomic weight and f_q the atomic scattering factor of the element q [12, 14].

From equation 7.3 we can quickly write down expressions for δ and β

$$\delta = \frac{N_A r_e \rho \lambda^2}{2\pi} \sum_{q=1}^{N} \frac{w_q}{A_q} f_q^{'} \tag{7.4a}$$

$$\beta = \frac{N_A r_e \rho \lambda^2}{2\pi} \sum_{q=1}^{N} \frac{w_q}{A_q} f_q^{''}, \tag{7.4b}$$

where $f^{'}$ and $f^{''}$ are the real and imaginary parts of the complex atomic scattering factor f defined in equation 7.1.

The typically small values for δ and β are demonstrated by figure 7.2 which shows the refractive index for silica (SiO_2). We can see from this that for lower photon energy, the values of δ and β are larger and that as photon energy increases, δ and β decrease and hence the refractive index approaches unity.

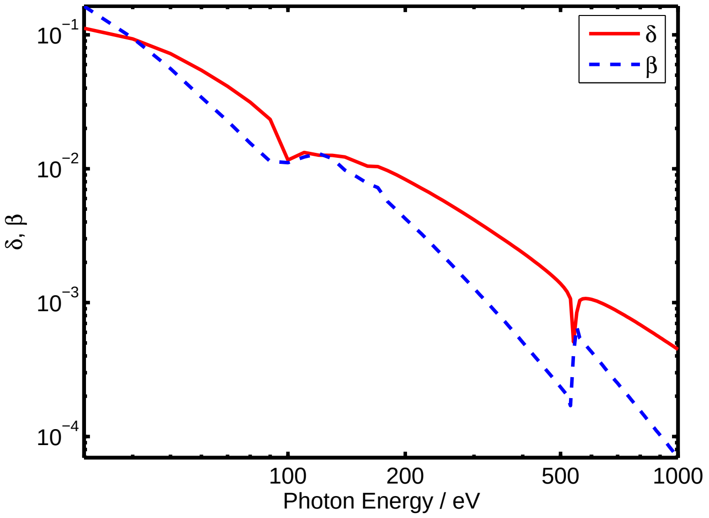

Figure 7.2: Values for δ and β from the complex refractive index of SiO_2 with mass density $\rho = 2.2$ g cm^{-3} at photon energies between 30 eV and 1keV. Data from reference [14] and calculated according to equation 7.4.

7.2.2 X-ray propagation and absorption

Using equation 7.3, it is possible to derive expressions for the phase variation and absorption during propagation. Consider a plane wave of the form

$$\mathbf{E}(\mathbf{r}, t) \;=\; \mathbf{E}_0 e^{-i(\omega t - \mathbf{k}\cdot\mathbf{r})}, \tag{7.5}$$

propagating in a material with initial amplitude $\mathbf{E}_0$ and having complex dispersion relation

$$\frac{\omega}{k} = \frac{c}{n} = \frac{c}{1-\delta+i\beta}. \tag{7.6}$$

By rearranging and substituting equation 7.6 into equation 7.5, we can obtain

$$\mathbf{E}(\mathbf{r}, t) = \underbrace{\mathbf{E}_0 e^{(-i\omega(t-r/c))}}_{\text{vacuum propagation}} \underbrace{e^{(-i(2\pi\delta/\lambda)r)}}_{\text{phase shift}} \underbrace{e^{(-(2\pi\beta/\lambda)r)}}_{\text{decay}}, \tag{7.7}$$

where the the first exponential factor describes the propagation of the wave in vacuum, the second factor represents the phase shift due to propagation in a medium and the third factor represents the decay of the wave in the medium because of absorption [12].

Expressions for the absorption length l_{abs} can be derived in terms of the imaginary part of the complex refractive index, β [12]

$$l_{\text{abs}} = \frac{\lambda}{4\pi\beta}, \tag{7.8}$$

or in terms of the imaginary part of the complex scattering factor f''

$$l_{\text{abs}} = \frac{1}{2n_a r_e \lambda f''}. \tag{7.9}$$

The attenuation length is the length over which the intensity of a wave drops to $1/e$ of the incident value. Most materials are highly absorbing to EUV and soft X-rays and, as an example, the absorption length of aluminium for 40 nm radiation is just 400 nm.

The experimentally observed absorption of thin films is given by the Beer-Lambert Law [126]

$$\frac{I}{I_0} = e^{-\rho\mu r}, \tag{7.10}$$

where ρ is the mass density, μ is the absorption coefficient and r is the foil thickness. The macroscopically observed absorption by thin films μ and the imaginary (absorptive) part of the atomic scattering factors f'' are related by [12]

$$\mu = \frac{2N_A r_e \lambda}{A} f'', \tag{7.11}$$

where N_A is Avagadro's number, and A is the atomic mass of the medium.

If it is assumed that the absorption of a material may be represented as a sum of the absorption of the individual atomic components, it follows from equation 7.11 that the absorption coefficient μ for a homogeneous material consisting of N elements with weight fractions w_q, irradiated with light of wavelength λ may be calculated from its relation to the imaginary part of the atomic scattering factor $f^{''}$ by the expression

$$\mu = 2N_A r_e \lambda \sum_{q=1}^{N} \frac{w_q}{A_q} f_q^{''}, \tag{7.12}$$

where r_e is the classical electron radius. Substituting values of μ into equation 7.10 enables the calculation of the X-ray intensity transmitted by arbitrary materials, such as thin-film filters.

Equation 7.11 is exploited in the calculation of the real part of the atomic scattering factors $f^{'}$ by measuring the absorption of radiation through thin foils (or gases) of the element of interest for a broad range of photon energy, typically using a broad range sychrotron source and monochromator [12]. From these measurements, the absorption coefficient μ may be calculated from equation 7.10 which leads to the imaginary part of the atomic scattering factors by simple rearrangement of equation 7.11.

In principle δ may be determined by measuring the phase shift using an interferometer. From equation 7.33 it can be see that the phase of a wave is shifted by propagation through a medium and we can write the relative phase shift $\Delta\phi$ compared to propagation in a vacuum as [12],

$$\Delta\phi = \frac{2\pi\delta}{\lambda} \Delta r, \tag{7.13}$$

where Δr is the propagation distance. By knowing the material thickness Δr and measuring the phase shift $\Delta\phi$, which manifests itself as shifts in the fringe pattern when the reference beam and object beam are recombined, one can calculate δ from equation 7.13 and therefore also deduce the real part of the atomic scattering factor from equation 7.4. In reality, interferometry at soft X-ray wavelengths is challenging because of high material absorptions, and the need for optically flat mirrors and beam splitters which is particularly challenging at X-ray wavelengths. However, this approach has been used to measure the real component of the refractive index [146, 147] and Rosfjord *et al.*, recently used this technique to measure the real part of the refractive index for silicon and ruthenium across the EUV and soft X-ray region. An alternative approach to calculating δ is through the Kramers-Kronig relations [12,14,143] which relate the real and imaginary parts of the atomic scattering factors.

7.2.3 Total external reflection

As a consequence of the refractive index for soft X-rays being so close to unity, the reflection coefficients for most angles of incidence are very small. The exception to this rule occurs for grazing incidence reflections and it will be shown that any polarization of light can experience a near total reflection, and discuss how this can be exploited to focus X-rays. *Total external reflection* is the X-ray analogue of total internal reflection in the visible. We can begin to understand total external reflection by considering Snell's Law for a medium of refractive index $n \approx 1 - \delta$, assuming for the moment that $\beta = 0$,

$$\sin \phi_r = \frac{\sin \phi_i}{1 - \delta}, \tag{7.14}$$

where ϕ_i and ϕ_r are the angle of incidence and angle of refraction respectively with respect to the surface normal. In contrast to visible light which will be bent towards the surface normal ($\phi_r < \phi_i$) when entering a medium of higher refractive index, for X-rays, with the real part of the refractive index less than unity, Snell's law shows that light will be refracted in the opposite direction, away from the surface normal. At glancing incidence, when ϕ_i approaches $\pi/2$, the refraction angle ϕ_r can equal $\pi/2$ and hence the refracted wave propagates along the surface without penetrating into the medium. The limiting condition is called the *critical angle*, $\phi_i = \phi_c$ and occurs for $\phi_r = \pi/2$, hence $\sin\phi_r = 1$ and from equation 7.14,

$$\sin\phi_c = 1 - \delta \tag{7.15}$$

Given that the phenomenon occurs only for angles close to 90^o, it is convenient to define an angle, θ, such that:

$$\phi + \theta = \frac{\pi}{2}, \tag{7.16}$$

and hence the critical angle (7.15) is rewritten,

$$\begin{aligned}\sin(\pi/2 - \theta_c) &= 1 - \delta \\ \cos\theta_c &= 1 - \delta.\end{aligned}$$

Since δ is small and therefore $\cos\theta_c$ is close to unity, θ_c is also very small and we can make the second-order small angle approximation [150]

$$1 - \frac{\theta_c^2}{2} + \ldots = 1 - \delta,$$

solving for θ_c gives

$$\theta_c = \sqrt{2\delta}, \tag{7.17}$$

as the solution for the critical angle for total external reflection X-rays [151]. Referring to equation 7.4, we can see that

$$\theta_c = \sqrt{2\delta} = \sqrt{\frac{n_a r_e \lambda^2 f'}{\pi}}, \tag{7.18}$$

where the atomic density n_a varies only slowly among the natural elements [12], meaning that the critical angle is strongly dependent on

$$\theta_c \propto \lambda\sqrt{Z}, \tag{7.19}$$

where Z is the atomic number and to a first order approximation is equal to f' [12]. Equation 7.19 suggests that the largest critical angle will be obtained for long wavelengths and higher Z materials, such as gold. In the next section it will be shown that absorption β also has a strong influence on the choice of material and obviously, the availability and mechanical properties of the material will affect its experimental suitability. From figure 7.2 we can see that for 40 nm radiation, δ = 0.0988 for SiO_2 and therefore the critical angle according to equation 7.17 is 0.45 radians. However, at 1keV, where δ = 4.47$\times 10^{-4}$, the critical angle has decreased to only 0.030 radians.

In the next section we will extend the above description to provide a complete explanation which accounts for the absorptive losses caused by the field penetration into the lossy medium and it will be seen that such losses prevent the reflection from being total at all angles.

7.2.4 Reflection coefficients

For XUV incident on the boundary between two homogeneous media (Figure 7.3) which are characterized by the refractive indices, $n_1 = 1$ and $n_2 = 1 - \delta + i\beta$, the amplitude of the reflected wave $\mathbf{k}_r$ may be calculated from the modified Fresnel formulae given by,

$$R_{\|} = \frac{n_2^2 \cos\theta_i - \sqrt{n_2^2 - \sin^2\theta_i}}{n_2^2 \cos\theta_i + \sqrt{n_2^2 - \sin^2\theta_i}}, \tag{7.20}$$

$$R_{\perp} = \frac{\cos\theta_i - \sqrt{n_2^2 - \sin^2\theta_i}}{\cos\theta_i + \sqrt{n_2^2 - \sin^2\theta_i}}, \tag{7.21}$$

for polarization components parallel with and perpendicular to the plane of incidence, respectively.

Figure 7.4 shows reflectivity curves as a function of the parameter β/δ for radiation incident on an interface with a material of refractive index

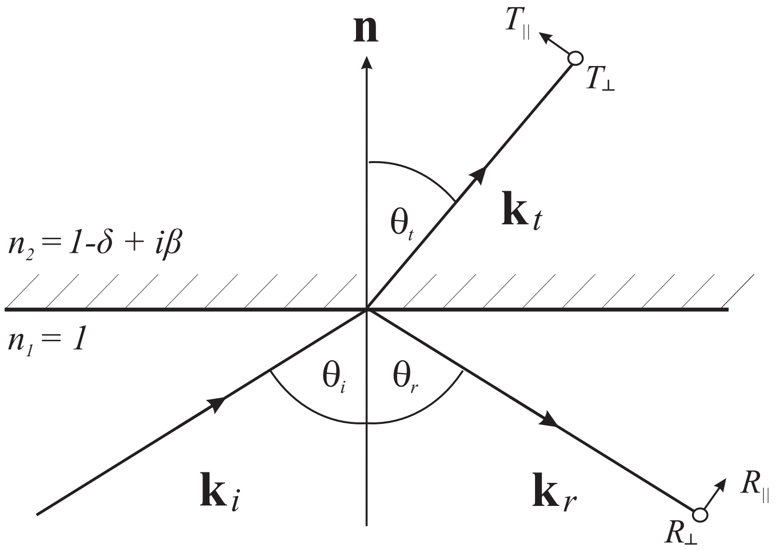

Figure 7.3: Refraction and reflection of a plane wave.

$n = 1-\delta+i\beta$, calculated from equation 7.20 or 7.21. From this, it can be seen that where the attenuation β is negligible, the reflectivity curve displays a sharp cut-off at the critical angle θ_c as discussed in section 7.2.3. This is typically the case for hard X-rays. However, when $\beta \neq 0$, absorption causes a rounding of the reflectivity curve until no sharp angular dependance of the reflectivity at the critical angle is discernable; this is typically the case for EUV and soft X-ray wavelengths.

7.3 X-ray optics

As a consequence of the small difference between the vacuum and material refractive indices discussed in section 7.2.1, the use of refractive optics, so common in the visible region, is difficult. The weak refraction effect result in extraordinarily long focal lengths, while high material absorption means the losses can be impossibly high. These problems have been solved in part by several groups who have recently fabricated successful refractive optics for hard X-rays (~ 5-40 keV) by drilling arrays of small holes

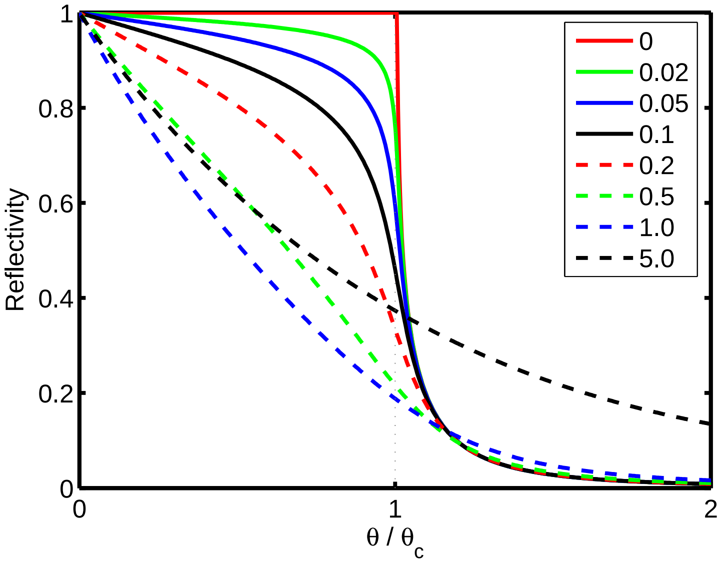

Figure 7.4: The dependance of reflectivity on θ/θ_c for values of β/δ.

in low-Z materials, such as lithium, beryllium and aluminium [152–154]. The use of low-Z materials minimizes the material absorption coefficient. In these compound refractive lens arrays, the holes act like a series of concave lenses, with the number of holes determining the focal length of the lens. In this way, a sequence of fifteen 250 μm holes in aluminium can give a compound lens of focal length 1m [153]. Paradoxically, although the refractive index variation for EUV and Soft X-Ray radiation is larger than in the hard X-Ray regime, with absorption lengths of the order of 1 μm at 30 nm, refractive optics are not a realistic option.

As a result of the difficulties presented by refractive optics at X-ray wavelengths, diffractive optics such as zone plates and curved reflective optics based on grazing incidence reflection or normal incidence multilayered optics are more commonly used for focusing both soft and hard X-rays. In the following sections we briefly review these different techniques and discuss their relative merits.

7.3.1 Zone plates

Zone plates are circular transmission gratings, with alternating symmetrical rings of opaque and transparent material. They are capable of forming a real image at the highest spatial resolution currently available and have found applications in X-ray microscopes at a number of synchrotrons [12]; recent work undertaken at the Advanced Light Source (ALS) by Chao *et al.* demonstrated a spatial resolution better than 15 nm [140]. Zone plates are typically fabricated by electron beam lithography followed by gold plating [155], a process made difficult by the requirement for accurately placed small features, with the outermost ring requiring a width comparable with the desired spatial resolution. The zone plates are formed on a transparent substrate, such as a thin silicon nitride membrane. Zone plate efficiencies are fairly low because of low diffraction efficiency and absorption from the supporting substrate; the zone plates fabricated by Chao [140] are 4% efficient. Currently, zone plates offer small apertures because of the difficulty of manufacturing large zone plates.

7.3.2 Multi-layered mirrors

Multi-layered interference coatings can be formed by alternatively depositing layers of two materials with different refractive index. The individual thickness of each layer is such that the reflections from each interface add in phase at the top of the stack. Individual layers are 1–10 nm thick which requires precision vacuum deposition techniques such as evaporation or sputtering. The response of the stack is strongly wavelength selective and for incident X-rays of wavelength λ, the stack has peak reflectivity at angle θ according to the Bragg equation,

$$n\lambda = 2d \sin\theta, \tag{7.22}$$

where n is an integer representing the order of the reflection, which for multilayered mirrors is typically first order, $n = 1$. In contrast to grazing incidence optics, multi-layered mirrors can offer efficient near normal incidence operation but over only a narrow spectral bandwidth. Efficiencies of $>$65 % have been achieved with molybdenum–silicon [96] multi-layers operating at 13.2 nm. The efficiency will always be less than 100 % because of material absorption within the multi-layers and is also limited by the surface roughness of the mirror substrate, interfacial roughness and interpenetration of the layers.

Multi-layered coatings can be applied to curved substrates for focusing and imaging applications. Mashiko *et al.* have used this technique to fabricate an off-axis parabolic mirror with a silicon carbide–magnesium multilayer capable of selectively focusing the 27th harmonic (29.6 nm) with an efficiency of 40% to a spot size of 1 μm

7.3.3 Grazing incidence optics

In section 7.2.3, we saw that it is possible to reflect EUV and X-ray radiation with high efficiency by glancing incidence reflection. This principle is widely used to focus X-rays using ellipsoidal or torroidal mirrors, the Kirkpatrick-Baez mirrors and tapered capillary optics. Currently, they do not offer as high spatial resolution as zone plates, however, well designed grazing incidence optics have the potential for efficient, high quality, aberration free focal spots with long working distances that do not depend on the photon energy of the beam. However, all these methods are limited by difficulties in fabricating the required optical profiles with minimal slope errors and sub-nanometer surface roughness.

For focusing mirrors, ellipsoidal surfaces are preferable to toroidal and spherical surfaces since these minimize aberrations at the expense of being more difficult to polish, particularly at higher energies which place more stringent requirements on surface finish. An alternative method which was one of the earliest devised methods to focus X-rays but which is still widely used today is the Kirkpatrick-Baez mirror [156] which employs a pair of orthogonal, concave mirrors at grazing incidence. This arrangement allows real imaging, is easier to construct than a single ellipsoidal mirror and by using a pair of mirrors, offers a straightforward technique for compensating for asymmetric beams (such as those produced by some synchrotrons) which require a different focal length mirror for each of the transverse directions.

Originally, cylindrical mirrors were used resulting in strong spherical aberration caused by the shallow incidence angles. For aberration-free imaging, an elliptical profile is essential, however, it is difficult to polish an elliptical mirror to the smoothness required for X-ray applications and a number of different fabrication techniques have been demonstrated. Liu *et al.* have demonstrated a differential coating techniques which selectively deposits films onto a well polished cylindrical mirror substrate [157]. Elliptically bent mirrors [158] perform controlled bending of flat substrates, such as silicon, offering an accurate elliptical profile which is much easier to achieve than from polished rigid substrates. Recently, Matsuyama *et al.* [159] demonstrated 30 nm spatial resolution from a Kirkpatrick-Baez mirror X-ray fluorescence microscope which is only a factor of two worse than the spatial resolution offered by the best zone plates.

7.3.4 Capillary optics

A further category of grazing incidence optics is the glass capillary optics which have been widely used on synchrotrons to transport and focus X-rays [160]. These devices rely on the grazing incidence reflection from the inner surface of a hollow capillary typically formed from glass. Carefully designed capillary optics offer close to 100 % transmission, can easily be designed to work across large energy bandwidths and are relatively compact. However, they can be hard to manufacture and require excellent control over the surface roughness of the material.

A review of the literature reveals a number of capillary profiles that are being used for focusing X-rays, as well as the simple straight capillary tubes which are used as X-ray waveguides to reduce the divergence loses when transmitting beams a long distance from the source [161]. Of the tapered profiles, three main types can be distinguished which are summarized in figure 7.5. Early devices tended to have conical profiles (figure 7.5(a)) since these were easiest to fabricate, however, they produce a strongly divergent beam with a focal spot located very close to the exit of the capillary. In a conical capillary, not all rays follow identical paths with the incident angle of the photons affecting the number of reflections it will make within the capillary. This reduces the efficiency of conical tapered capillaries, disperses short pulses and adds extra components to the spatial mode from the tapered capillary.

As fabrication technology has improved, ellipsoidal and paraboloidal capillary profiles have been developed. It can be seen from figure 7.5(c) that light emanating from a point source S placed at one of the focal points of an ellipsoidal device will be refocused on the point F. However it is apparent that photons emanating from a region S′ outside the point source S will not be refocused on the point F and can lead to multiple reflections within the device. In contrast, a paraboloidal capillary (figure 7.5(b)) focuses parallel rays to a focal point F, however, a divergent beam may undergo multiple reflections within the device. The real X-ray beam is neither perfect point source nor parallel beam and hence the ideal capillary optics where all rays undergo only a single reflection depends on the beam waist, the distance from the waist and the divergence of the beam. The single reflection capillary offers the advantages of long working distances, transmission close

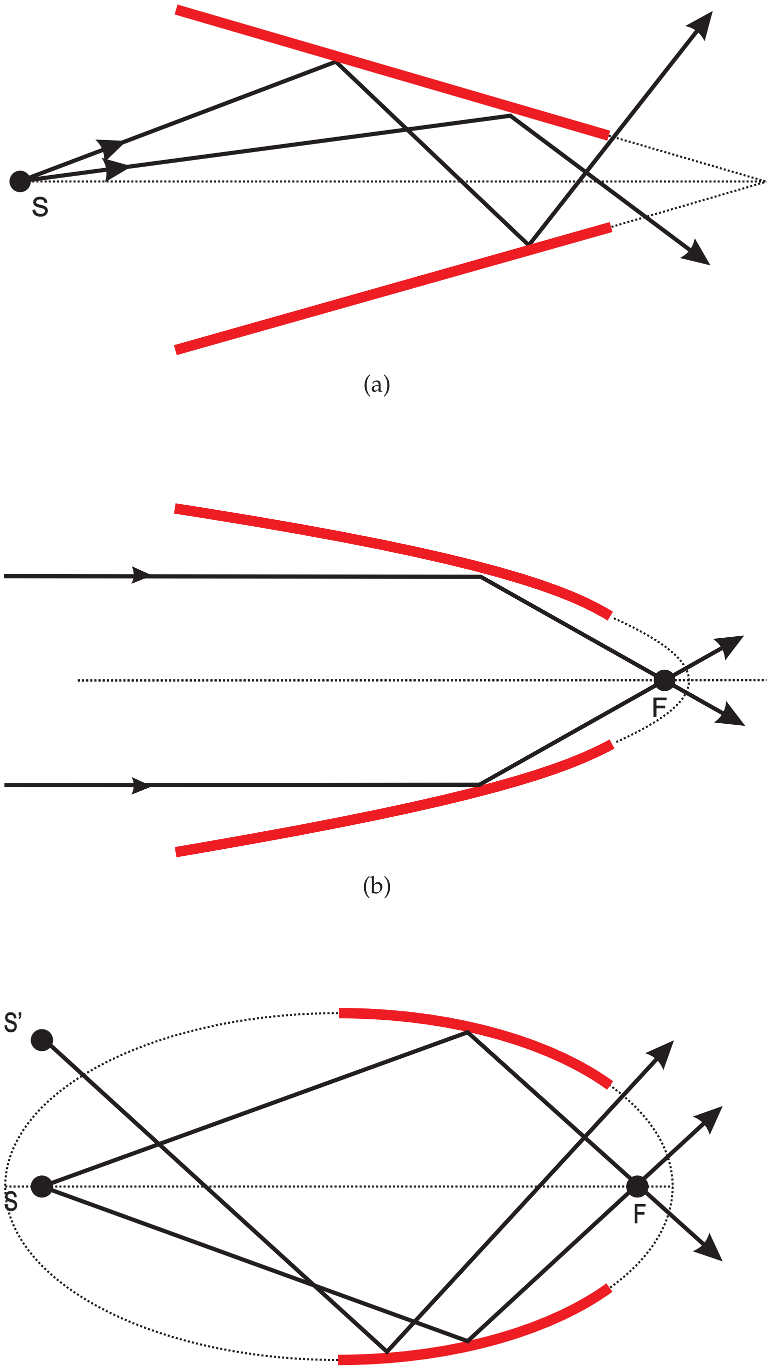

(a)

(b)

(c)

Figure 7.5: (a) conical, (b) parabolic and (c) elliptical tapered capillary profiles

to unity, and a perfectly formed capillary where all path lengths are equal will not disperse a short pulse [160].

It is possible to bundle a large number of capillaries together to form polycapillary lenses which offer a better collection solid angle. However, polycapillary lenses are not suited to work with short pulses because the photon trajectories through the outer part of the bundle are significantly longer than the center of the bundle thereby stretching the pulse.

7.4 Modelling

Ray-tracing can be used to understand the operation of tapered capillary focusing devices to aid their manufacture and for interpreting the experimental results. It can be used to optimize the throughput and minimize the number of reflections.

A thorough treatment of the propagation of X-rays through a tapered capillary requires the use of a wave model. Such models have been developed by Dabagov [162] and Kukuhlevsky [163] for simple one-dimensional waveguides and involve analytical solutions to the Huygens-Fresnel equation. For more complicated structures, most modelling has been limited to ray-tracing simulations that work within the geometrical approximation. A number of these models assume that the tapered capillary can be represented by a simple two-dimensional [164] cross-section and therefore cannot be used to understand the effects of misalignment or bending of the capillary. The most comprehensive model has been developed by Vincze [161] which can model arbitrary shaped capillaries in three-dimensions. I extend the work of Vincze, developing a fully three-dimensional model that models the X-ray source as a gaussian beam and accounts for the phase of the X-rays which is missing from Vincze's model.

In the limit where the wavelength can be considered small in comparison to the tapered capillary, geometrical optics can be used as an approximate solution for the problem of wave propagation [129]. In geometrical (or ray) optics, a wave field can be described as a series of rays where the propagation of those rays in different media described according to geometrical laws. We can calculate the complex amplitude **E** of a monochromatic wave field with wavelength λ traveling in a medium of fixed refractive index as a function of position **r** in space given by

$$\mathbf{E}(\mathbf{r}) = A(\mathbf{r})e^{ik_0\mathcal{S}(\mathbf{r})}, \tag{7.23}$$

where $k_0 = 2\pi/\lambda$ is the wavevector, λ is the wavelength and $k_0\mathcal{S}(\mathbf{r})$ is the phase of the wave. $\mathcal{S}$ is called the *eikonal*, where the constant phase surfaces

$$\mathcal{S}(\mathbf{r}) = \text{constant} \tag{7.24}$$

can be considered to represent the geometrical wave-fronts. We represent the rays as straight lines and calculate their position **r** at a point n as

$$\mathbf{r}_{n+1} = \mathbf{r}_n + s\mathbf{u}_n, \tag{7.25}$$

where **u** is a unit vector representing the direction of propagation of the ray and s is the optical path length and is equivalent to $\mathcal{S}(\mathbf{r})$ given by equation 7.23. By using equations 7.23 and 7.25 it is possible to describe the complex amplitude of the field for any arbitrary point in space.

7.4.1 Gaussian X-ray source

The point of origin $\mathbf{r}_0$ and direction of propagation $\mathbf{u}_0$ of the rays are selected according to the desired characteristics of the source. The high harmonic source is generated by a gaussian laser beam and can be satisfactorily modeled as a gaussian beam. The key features of a gaussian beam are

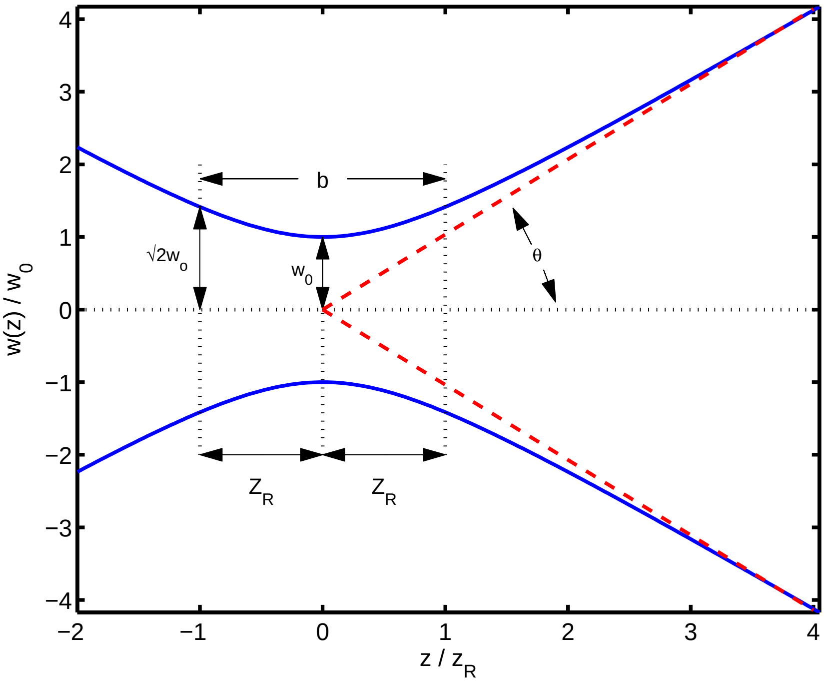

Figure 7.6: The key features of a gaussian beam, including the beam waist w_0, confocal parameter b, Rayleigh range Z_R, and far-field divergence angle θ

illustrated in figure 7.6. Given a suitable statistical distribution of rays distributed in transverse position and angle, it is possible to model the propagation of a gaussian beam in free space or as it is interacts with optical elements. By propagating each ray through the system using the laws of geometrical optics, the *distribution* of the rays will follow the laws of a gaussian beam even though individual rays will not [165]. In this way, we can mimic the propagation behavior of a gaussian beam without needing to invoke wave theory.

The point of origin $\mathbf{r}_0$ is selected according to a two-dimensional gaussian probability distribution function,

$$\mathbf{r}_0(x,y) = \exp -(2x^2/x_0^2 + 2y^2/y_0^2), \tag{7.26}$$

where x_0 and y_0 are the $1/e^2$ radius of the intensity at the beam waist in the x and y transverse directions respectively. Similarly, an initial angular distribution is generated from a gaussian angular distribution function,

$$f(\theta_x, \theta_y) = \exp -(2\theta_x^2/\theta_{x0}^2 + 2\theta_y^2/\theta_{y0}^2), \tag{7.27}$$

where θ_{x0} and θ_{y0} are the far field divergence angle of the beam measured at the $1/e^2$ radius of the intensity in the x and y transverse directions respectively. From this, an initial propagation vector is formed by,

$$\mathbf{u}_0 = \begin{bmatrix} \sin(\theta_x) \\ -\sin(\theta_y) \\ \cos(\theta_x) \end{bmatrix}. \tag{7.28}$$

Figure 7.7(a) shows the two-dimensional intensity distribution generated by propagating 10^6 rays distributed according to the gaussian spatial and angular distributions in equations 7.26 and 7.27, where the intensity is proportional to the number of rays passing through each picture element (pixel). The shape of this image shows qualitative agreement with the expected shape of a gaussian beam, as shown in figure 7.6. Figure 7.7(b) shows a plot of the $1/e^2$ intensity contour, which corresponds to the beam radius, extracted from figure 7.7(a). This shows excellent quantitative agreement with the beam waist w calculated from the analytical expression for a gaussian beam given by [88]

$$w(z) = w_0\sqrt{1 + \left(\frac{z}{z_R}\right)^2}, \tag{7.29}$$

where w_0 is the beam waist and z_R is the Rayleigh length, given by $z_R = \pi\, w_0^2/\lambda$.

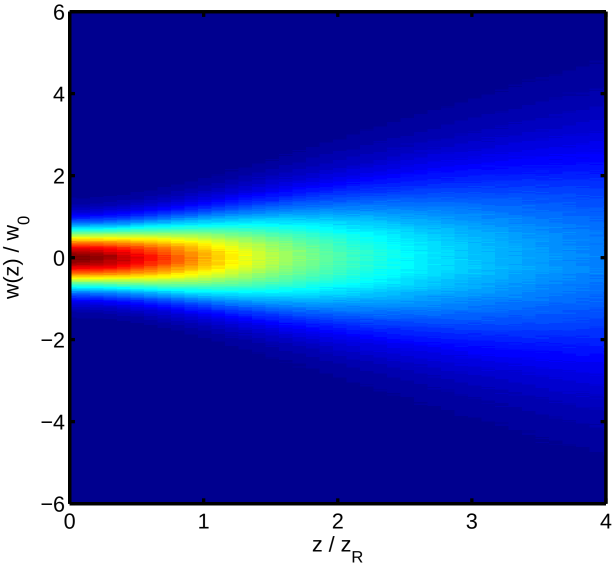

(a)

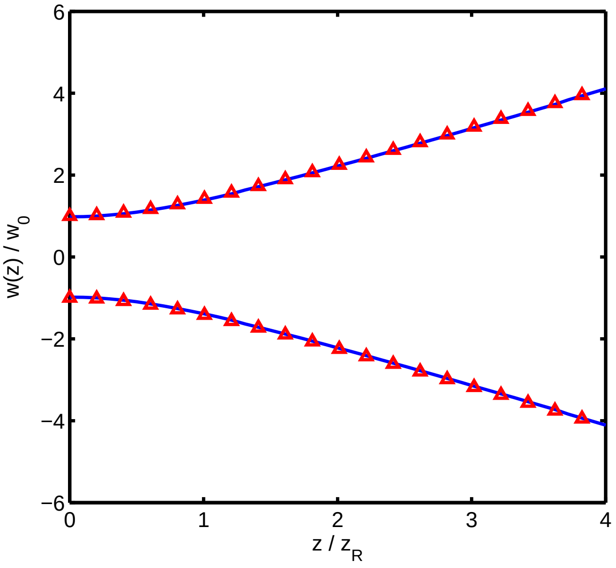

(b)

Figure 7.7: (a) The two-dimensional intensity distribution generated by propagating 10^6 rays distributed according to a gaussian spatial and angular distributions; (b) a plot of (triangles) the $1/e^2$ contour from (a) compared with the (solid line) analytical expression for the beam waist of a gaussian beam.

7.4.2 Tapered surface

We define the shape of the tapered capillary as a parametric surface **S** as a function of the two parameters z and ϕ such that

$$\mathbf{S}(z, \phi) = \mathbf{A}(z) + R(z)[\hat{\mathbf{\imath}} \sin(\phi) + \hat{\mathbf{\jmath}} \cos(\phi)], \tag{7.30}$$

where **A**(z) is a vector function that describes the shape of the capillary's central axis and allows us to include distortions such as bends and twists to the shape of the capillary. R(z) is a scalar function describing the radius of the capillary as a function of z about the axis **A** and $\hat{\mathbf{\imath}}$ and $\hat{\mathbf{\jmath}}$ are unit vectors parallel to the x and y axes respectively [161].

For a paraboloidal capillary, the function $F(z)$ is given by

$$F(z) = p_0 \left[1 - \left(\frac{z - d_t}{l + d_s}\right)\right]^{1/2}, \tag{7.31}$$

where p_0 corresponds to the radius at the entrance of the capillary, d_t the distance from the source to the taper entrance and d_s the distance from the taper exit to the camera and are defined in figure 7.8. Alternatively, $F(z)$ may be determined from experimental measurements of the capillary dimensions.

7.4.3 Ray trajectories

Given the initial origin and direction of propagation determined previously, we can calculate the position of the ray at any point in space according to equation 7.25 and calculate the first intersection between each ray and the surface of the taper by evaluating the point where equations 7.25 and 7.30 are equal

$$|\mathbf{r}_n + s\mathbf{u}_n - \mathbf{A}(z_n + s u_{z,n})| = R(z_n + s u_{z,n}). \tag{7.32}$$

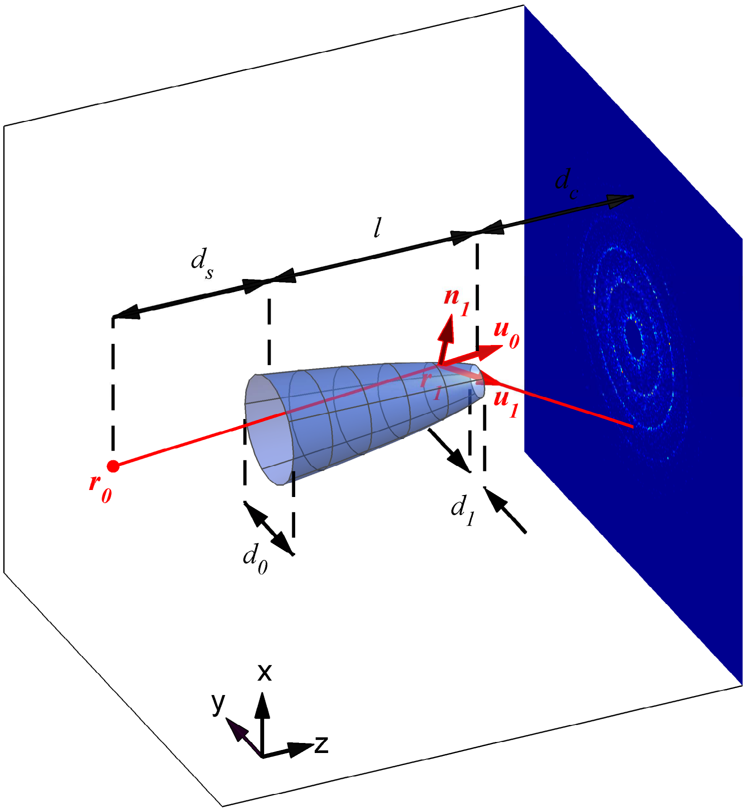

Figure 7.8: In the simulation, a tapered capillary with input diameter d_0, output diameter d_1 and length l is located a distance d_t from an extended X-ray source. Photons originate from an initial point, $\mathbf{r}_0$, with an initial propagation vector $\mathbf{u}_0$, defined by gaussian probability distribution functions. The first reflection occurs at the point $\mathbf{r}_1$, where the vector normal to the surface, $\mathbf{n}_1$ leads to the calculation of the new propagation vector $\mathbf{u}_1$. The rays are traced through any subsequent reflections and their location, $\mathbf{r}_s$ calculated on a camera at distance d_s from the capillary exit.

Depending on the form of function R, there can be several possible solutions for s, however, only the first positive root of equation 7.32 is the physically meaningful since this corresponds to the first intersection between the ray and tapered surface. Furthermore, equation 7.32 can only be solved analytically when $R(z, \phi)$ is of a limited number of types and for more complex expressions, equation 7.32 is solved numerically. In the simulation, the Matlab® function `fminbnd` is used to find values of s, the ray path length, which satisfy equation 7.32. This algorithm is based on a golden section search with parabolic interpolation. This is a simple linear search algorithm that does not require derivative information, is quick to converge given sensible boundaries and is extremely robust. In a golden section search, the minimum of a function is found by successive bracketing. Initially, a function f is bracketed by a triplet of points (a, b, c), such that $f(b) < f(a)$ and $f(b) < f(c)$. It is now known that the function has a minimum in the interval (a, c). The function is then evaluated at an intermediate point x to find a new, smaller bracketing interval in the interval (a, b) or (b, c). For example, choosing the later case, $f(x)$ is evaluated and if $f(b) < f(x)$, the new bracketing triplet of points is (a, b, x), otherwise, if $f(b) > f(x)$, the new interval is (b, x, c). In the generic case of a smooth function, the function should be parabolic about the minimum and a parabola fitted through the triplet of points should take us directly to the minimum or at least very close to it. This can act to speed up the convergence and the algorithm iterates between parabolic steps and golden sections to minimize the function. The process is repeated until the distance between the two outer points of the triplet is acceptably small [166].

Given the co-ordinates of the first ray intersection $\mathbf{r}_1$ with the inner capillary surface, it is necessary to calculate the new direction of propagation $\mathbf{u}_1$,

$$\mathbf{u}_1 = \mathbf{u}_0 - 2\mathbf{n}_1(\mathbf{n}_1\mathbf{u}_0), \tag{7.33}$$

where $\mathbf{n}_1$ is the normal unit vector of the inner surface of the capillary at the point $\mathbf{r}_1$.

7.4.4 Surface normal

The surface normal is calculated by taking partial derivatives of the surface parameterizations giving vectors which define tangent planes to the surface. Given that these are not zero or parallel, the vector cross product of these partial derivatives defines a vector which is mutually perpendicular to the two vectors, that is, the surface normal $\mathbf{n}$ where

$$\mathbf{n} = \frac{\partial \mathbf{S}}{\partial z} \times \frac{\partial \mathbf{S}}{\partial \phi}. \tag{7.34}$$

We can use the determinant to calculate a numerical value for the cross product in equation 7.34 [167],

$$\mathbf{n} = \frac{\partial \mathbf{S}}{\partial z} \times \frac{\partial \mathbf{S}}{\partial \phi} = \left(\begin{vmatrix} \frac{\partial S_y}{\partial z} & \frac{\partial S_z}{\partial z} \\ \frac{\partial S_y}{\partial \phi} & \frac{\partial S_z}{\partial \phi} \end{vmatrix}, - \begin{vmatrix} \frac{\partial S_x}{\partial z} & \frac{\partial S_z}{\partial z} \\ \frac{\partial S_x}{\partial \phi} & \frac{\partial S_z}{\partial \phi} \end{vmatrix}, \begin{vmatrix} \frac{\partial S_x}{\partial z} & \frac{\partial S_y}{\partial z} \\ \frac{\partial S_x}{\partial \phi} & \frac{\partial S_y}{\partial \phi} \end{vmatrix} \right). \tag{7.35}$$

and this can be converted to the unit surface normal $\hat{\mathbf{n}}$ by dividing by the vector's length,

$$\hat{\mathbf{n}} = \frac{\mathbf{n}}{|\mathbf{n}|}. \tag{7.36}$$

7.4.5 Reflected intensity

The angle of incidence of the photon relative to the plane of incidence is calculated from the expression

$$\theta = \arcsin(\mathbf{n}_1 \mathbf{u}_1) \tag{7.37}$$

and this can be used to calculate the reflected intensity

$$I_1 = I_0 R(\theta), \tag{7.38}$$

where $R(\theta)$ are the Fresnel coefficients and I_1 is the incident intensity. In the simulation, the initial intensity I_0 of all photons is defined as unity. The high harmonic source is polarized but we neglect this in the calculation of the Fresnel coefficients and use expressions for unpolarized light. This is a reasonable assumption since, at shallow angles of incidence, the Fresnel coefficients for s- and p-polarized fields are equivalent.

7.4.6 Simulation

The trajectory of each ray is calculated using equations 7.33 and 7.32 until the ray has escaped from the capillary. In contrast to other simulations [161], the photon is not thrown away if the angle of incidence of the ray exceeds a pre-defined angle because in the XUV region, there is no definite critical angle and any reflection produces a finite probability of reflection (see figure 7.4). Once the co-ordinates of the final reflection inside the taper have been determined, these are stored along with the propagation vector and the process is repeated until the desired number of photons have been simulated. In a typical simulation, good results are seen with $10^5 - 10^6$ rays. I have written code in Matlab® based on the procedure described above and simulations were run on the Southampton University Iridis2 cluster, typically requiring one hour of processor time for a simulation of 10^6 rays.

7.4.7 Camera

The output from the simulation is an array containing the co-ordinates of the final reflection inside the capillary and the final direction of propagation. From this, we can build an image at any point in space to visualize the output from the capillary. The virtual camera is a two-dimensional histogram of photon arrivals at discrete 'pixels' in space within a plane perpendicular to the axis of the taper (see figure 7.8). We can perform a coherent sum of the total E-field E_t at each pixel position (x,y)

$$E_t(x,y) = \sum E(x,y), \tag{7.39}$$

where $E(x,y)$ are the individual E-field components of each ray calculated according to

$$E(x,y) = \sqrt{I}e^{ikz}, \tag{7.40}$$

where k is the wavevector, z is the total path length of each ray and I is the intensity calculated according to equation 7.38. The total intensity is then calculated by [129]

$$I(x,y) = E_t(x,y) \cdot E_t(x,y)^\star, \tag{7.41}$$

where $E^\star$ is the complex conjugate.

7.5 Experimental

7.5.1 Fabrication

Tapered capillary optics are commonly fabricated by the controlled heating and stretching of a capillary precursor. Once the desired taper shape has been determined, for example by use of the ray-tracing model described above, the next step is pulling such a taper from the bulk fiber. The first tapered capillary optics were fabricated by relatively crude techniques. Bilderback *et al.* heated lead glass capillaries in a vertical tube furnace with a weight attached to the end. By heating the capillary the glass would soften and the weight would elongate the capillary until it separated forming a sharp point [168]. Such capillaries showed far from optimal performance, since the precise shape could not be controlled and varied randomly between capillaries. Bilderback *et al.* went on to devise a computer controlled capillary puller capable of repeatable fabrication of capillaries with a desired profile [169].

The dependence of taper shape on the tapering conditions has been studied by Birks *et al.* for the manufacture of fibre tapers for use in optical fibre components, such as directional couplers, beam expanders and nano-wires [170]. They demonstrate a taper fabrication technique which is capable of producing any reasonable taper shape.

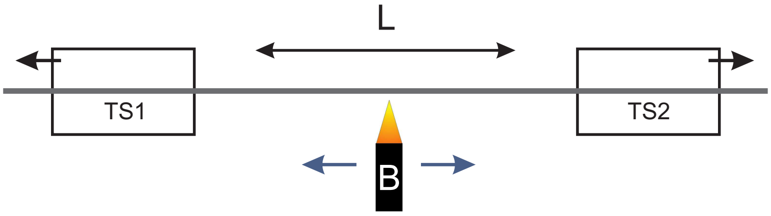

Figure 7.9: A schematic representation of the traveling-burner, tapered capillary fabrication system. A fibre is attached to translation stages TS1 and TS2, which slowly move apart stretching the fibre. A small burner B oscillates with constant speed over a distance L. During fabrication, L can be varied to control the precise taper shape. (Adapted from [170].)

The fibre tapers were fabricated by Gilberto Brambilla of the Optoelectronics Research Centre (ORC) and a schematic of the experimental setup is shown in figure 7.9. The model assumes the glass will be heated uniformly within the hot zone L without heating the fibre in the surrounding area. It is also important that the size of the heated region is controllable and variable during the tapering procedure. To achieve this we use the travelling burner technique [170] where a point heat source based on a oxygen-butane burner travels at a constant speed in an oscillatory manner along the distance L, so that in each cycle, every element in L is heated uniformly. If the burner's speed is large compared to the elongation of the taper, a time-averaged hot zone is setup which satisfies the model. The length of the hot-zone is easily changed during fabrication by varying the travel of the burner and the precise taper shape may be determined by computer control of this parameter according to the expressions developed by Birks *et al.* [170]

The tapered capillary used in the experimental work described in this thesis was manufactured by Chiral Photonics Inc following a fire which destroyed the ORC's fabrication facilities and as a result of this a very limited number of tapered capillaries were available. The tapered capillaries were manufactured from a hollow capillary pre-cursor with an inner diameter of 100 μm. This was the largest size precursor it was possible to taper using this technique because of the need to ensure the fibre is heated uniformly. The capillary profile was characterized using an Olympus optical microscope equipped with a 20x magnification objective. The capillary was placed on a linear translation stage with micrometer adjustments to allow measurements over the entire length. Images of the capillary were captured with a video camera and the dimensions measured with the ImageJ software package. A graticule (Agar Scientific) was used to calibrate the profile.

Figure 7.10 illustrates the measured profile of the tapered capillary. The root mean squared error (RMSE) of the capillary profile is 369 nm, calculated from a parabolic fit of equation 7.31 to the measured capillary profile. The tapered capillary has had 23 mm removed from the tapered end because the pulling process failed to successfully track the parabolic profile beyond this point.

7.5.2 Alignment

Taper alignment was carried out in a 600 mm diameter cylindrical vacuum chamber placed at the end of the XUV beam line. A schematic of the experimental setup is shown in figure 7.12. The XUV beam is filtered from

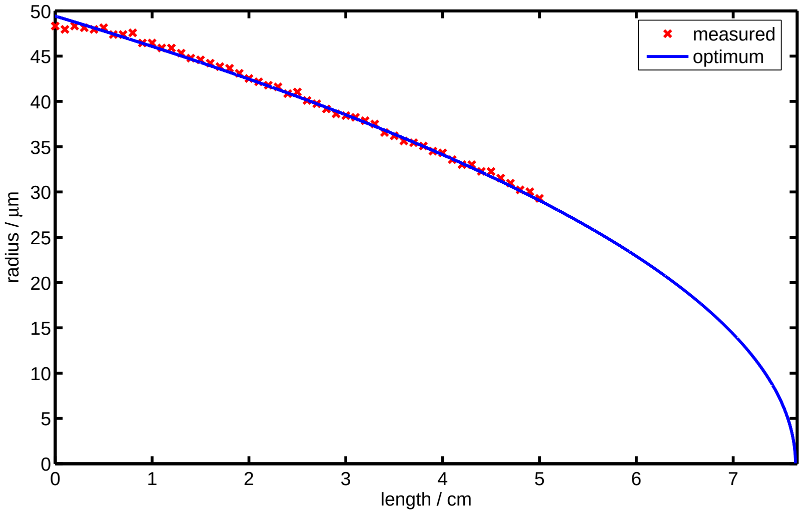

Figure 7.10: The measured tapered capillary profile (crosses) compared to an ideal profile (solid line) for a parabolic taper with parameters $p_0 = 49.4\ \mu$m, $l = 5.3$ cm, and $d_p = 2.3$ cm.

the infra-red using a 200 nm aluminium filter, as described in chapter 4, and enters the chamber through an iris that can be adjusted from outside the chamber. The XUV beam was $\sim$ 1 mm at the entrance to the chamber (measured at $1/e^2$ of the maximum intensity) and the iris prevents stray light from passing around the sides of the taper. The tapered capillary is held on a V-groove on a five-axis translation stage. The capillary is aligned by monitoring the beam profile and maximizing the X-ray throughput on a CCD camera. Once aligned, the beam profile of the focused X-ray beam can be measured as a function of distance from the capillary exit by translating the X-ray CCD camera on a linear translation stage.

7.6 Results and discussion

Figure 7.12 shows the output recorded from a tapered capillary with a profile similar to that shown in figure 7.10. In figure 7.12(a), the camera is placed very close to the tip of the tapered capillary and the spot is approx-

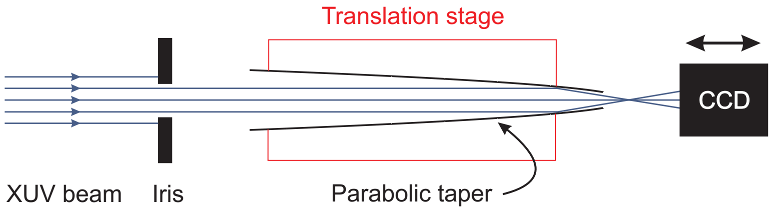

Figure 7.11: The experimental setup for characterizing and testing tapered capillaries. The capillary is held on a V-groove on a five-axis translation stage. An iris prevents stray light from reaching the CCD camera which records the image of the beam leaving the taper.

imately 64 μm measured at the full-width at half maximum intensity. The size of this spot corresponds to the size of the exit aperture of the capillary. As the camera is moved away from the end of the taper, it can be seen that the beam profile consists of a bright central spot surrounded by rings of lower intensity. At a distance of about 13 mm from the end of the tapered capillary, the central spot gets smaller and is focused while the surrounding ring structure continues to expand. Within the geometrical approximation of our model, the different parts of the beam can be explained by considering photons that have taken different trajectories through the capillary. The small central spot arises from single reflection photon trajectories and is the component of the beam with the lowest divergence. The surrounding rings results from photons that have undergone two or more reflections and the diffuse background is a result of photons that have passed straight through the tapered capillary, undergoing no reflections. Figure 7.13 shows a graphic illustration of two possible photon trajectories that can arise: rays can pass straight through the tapered capillary without interacting (indicated by the blue rays) or rays can make one or more reflections on the inner wall of the taper (indicated by the red rays). The rays that pass straight through the taper contribute to the background surrounding the central bright spot and explain why the output at the exit of the taper in approximately the same size as the exit aperture. The camera does not have

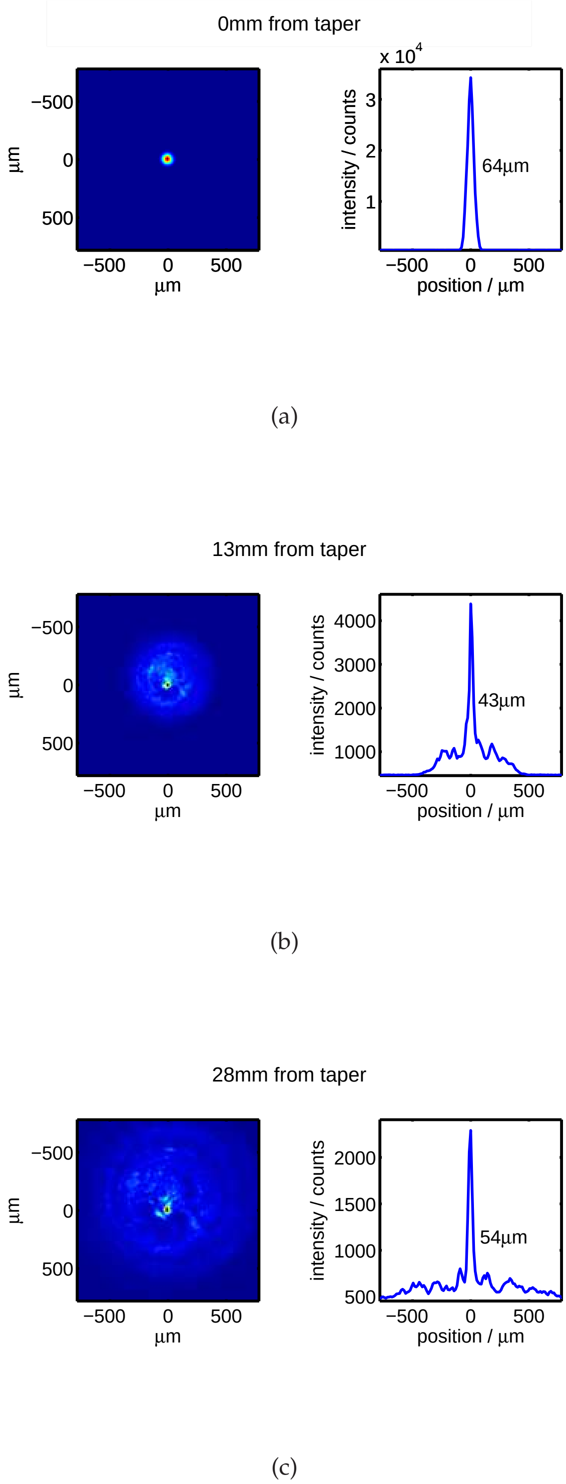

(a)

(b)

(c)

Figure 7.12: The output of the tapered function at (a) 0 mm, (b) 13 mm and (c) 28 mm from the end of the tapered capillary. The text indicates the full-width at half maximum intensity of the bright central spot.

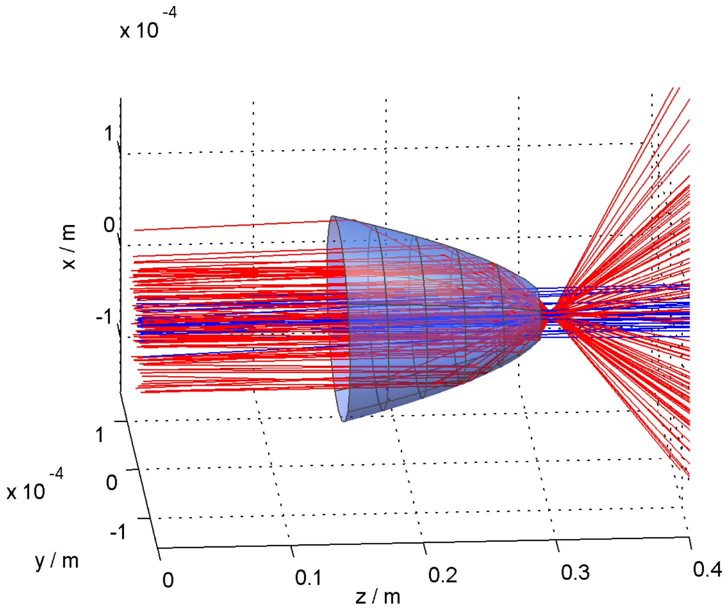

Figure 7.13: Graphic example of the raytracing process. The blue rays pass straight through the taper while the red rays make at least one reflection from the tapered capillary wall and are focused.

sufficient resolution to resolve the difference between the brighter central spot and the diffuse rings around the outside.

As well as the diffuse background caused by rays that do not interact with the taper, rays that make multiple reflections with the wall of the taper can result in a beam that propagates in multiple rings. This can be seen clearly in the data in figure 7.14 which shows a slice through the centre of the beam as it propagates away from the taper. In this example, at short distance < 1 mm the spot is confined to a small central area and no rings are observed. As the beam propagates, the beam splits up into multiple rings and this is a direct result of the different photon trajectories that exist in the tapered capillary. The central spot corresponds to one reflection, and the first ring to two reflections and hence the n^{th} ring corresponds to the $n+1^{th}$ reflection, with rings becoming increasingly divergent with each additional reflection. In the example shown in 7.14, most photons undertake

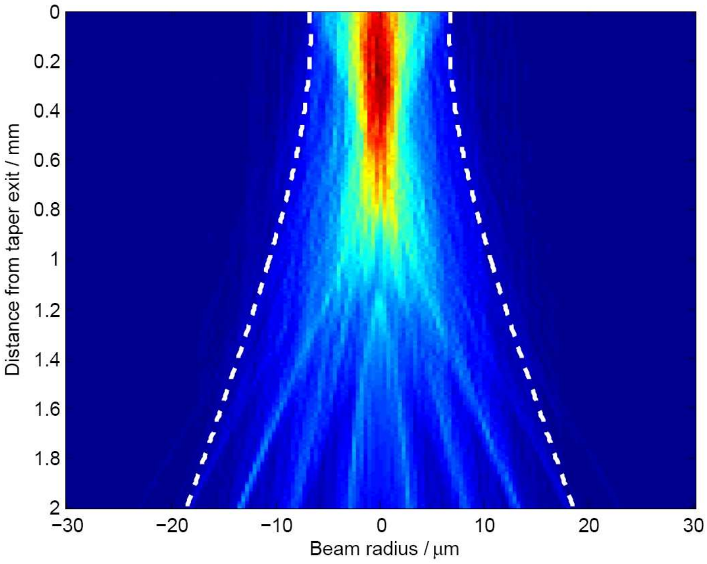

Figure 7.14: Slice through the centre of a simulation of light propagating from a parabolic tapered capillary showing how the spatial profile of the beam changes as it propagates.

a single reflection but as many as seven reflections occur for some photons.

We can see this ring structure clearly in the experimental data in figure 7.15. This data was recorded in our group by Mills and shows the image of the tapered capillary at a distance of 45 mm from the exit of the capillary. The ring structure has been enhanced by changing the length of exposure across the beam.

Using the ray tracing model gives us a good understanding of the focusing properties of tapered capillaries and will allow us to optimize future designs to best match the high harmonic beam.

7.7 Summary

Tapered capillaries show promise as XUV focusing optics and this chapter has demonstrated experimental results from an early design of tapered capillary. The model that has been developed explains a number of the fea-

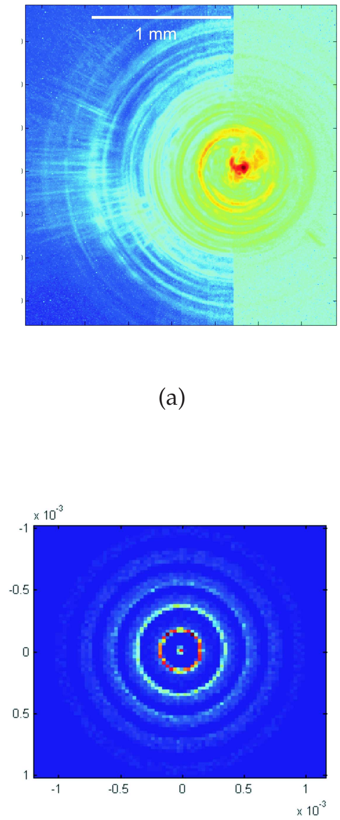

(a)

(b)

Figure 7.15: (a) The experimentally measured output from the tapered capillary at a distance of approximately 45 mm from the output of the capillary. The image is composed of slices taken at different integration times to enhance the contrast of the weak ring structure. (b) Theoretical prediction of the output given by the raytracing model.

tures of the experimentally measured images and will be used to refine the shape in future fabrication attempts.

A novel application for tapered capillary optics is the direct generation of high harmonics inside the tapered capillary. This could be achieved by drilling holes in the taper wall to inject gas as in the current experiment. The taper may have the added advantage of separating the laser from the XUV since the laser mode will become very lossy as the waveguide is tapered down in diameter, though work will need to be done to see whether this results in damage to the tapered capillary.

Chapter 8

Conclusions and future work

This thesis has described the design and construction of a capillary based high harmonic source. This source has demonstrated excellent efficiency, generating $> 10^7$ photons per pulse for the 25th harmonic in a beam with low divergence and excellent spatial mode quality.

This work has shown that ionization plays two roles in the harmonic generation process being an important component of phase-matching and influencing the spectral characteristics of the harmonics. From this, a technique for frequency shifting the harmonics was developed that is able to shift the harmonics by as much as 50% of the energy separation between adjacent harmonics. This was achieved by exploiting the effects of ionization in the capillary which result in a frequency shift of the fundamental. It was shown that this can be controlled in a precise and variable way using an acousto-optic programmable dispersive filter to apply specific amounts of second order dispersion to the fundamental. This frequency-agile source could be used in the future for X-ray spectroscopy or resonant scattering experiments with the source tuned to match particular resonances for element specific mapping.

As well as having an effect on the fundamental, we have shown that the harmonic generation process is sensitive to the level of ionization. For high energy pulses, it has been demonstrated that ionization limits the harmonics that can be efficiently phase matched, limiting the maximum photon energy that is observed irrespective of the increased laser pulse energy. To further understand the effects of ionization, a fully three-dimensional phase-matching model is being developed by Rogers and a paper describing this model is currently being prepared. This model shows that by accounting for the variation of ionization radially across the capillary and in time during the pulse, excellent agreement can be achieved with experimental data.

We have shown that it is possible to control the spatial distribution of ionization in the capillary by exploiting the mode beating which occurs between different capillary modes and we have developed a simple method for imaging and modelling this process. By considered design of the pressure profile to enable a high gas pressure at the peak of the beat but nowhere else in the capillary, it is expected that we can enhance the intensity of the generated harmonics. Praeger has recently designed micro-structured capillaries that are capable of precisely controlling the gas profile in the capillary.

Finally we have looked at the theory behind focusing XUV using tapered capillary optics and shown a few first experimental results. The model that was developed will be used to derive the optimum shape for the design of future capillary optics. The first scattering experiments using this source have begun, looking at the scattering from arrays of beads and non-repetitive objects formed on silicon nitride membranes with a focused ion beam mill, taking us closer to our ultimate goal - single isolate molecule scattering.

Appendix A

XUV Spectrometer

The XUV spectrometer, introduced in chapter 4 and used in experiments throughout this thesis, was a Rowland circle geometry grazing incidence spectrometer, supplied by Shulz Scientific. This appendix details the optical design and procedures that were developed for wavelength calibration of the spectrometer.

A.1 Optical Design

If a concave grating is placed on the tangent of a circle with diameter equal to the radius of curvature of the grating, a point lying on the circle at the entrance slit will be focused to another point at the detector on the opposite side of the circle. This circle is commonly called the Rowland circle [171].

Figure A.1 illustrates the optical design of the XUV spectrometer. The XUV beam passes through a 100μm entrance slit and onto a concave gold grating with 1 m radius of curvature, both of which are placed on the Rowland circle. The grating has high efficiency at grazing incidence and disperses the XUV across a microchannel plate (MCP) detector. The MCP is curved along the Rowland circle resulting in linear wavelength calibration and sharply focused spectral lines. X-ray photons interact with the 12 μm

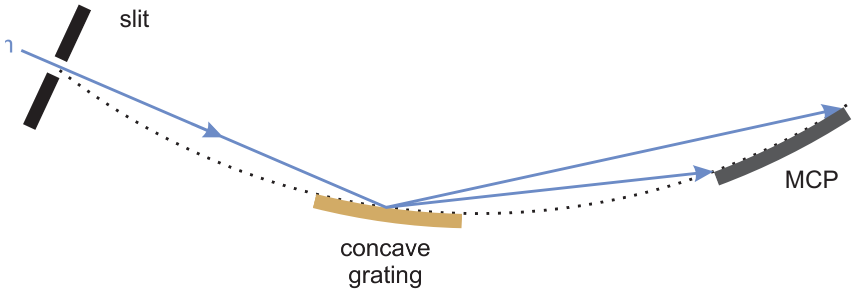

Figure A.1: Rowland circle grazing incidence XUV spectrometer. The dashed line indicates the Rowland circle.

channels to produce a cascade of electrons which are accelerated by a potential difference of ~ 1 kV (Iseg SHQ 122M) applied across the plate. The electron signal from the MCP is imaged on to a phosphor plate to produce visible light which is recorded with a cooled CCD camera (Princeton Instruments Pixis 400).

A.2 Wavelength Calibration

The MCP is placed in a fixed position around the Rowland circle and therefore the wavelength region of interest is selected according to the groove spacing d of the grating. Three gratings, whose properties are summarized in table A.1, were available giving access to the wavelength region 5–60 nm. The wavelength of a spectral line may be calculated by its position on the Rowland circle,

$$n\lambda = d\left[\sin(\alpha) + \sin\left(\frac{x}{R}\right)\right], \tag{A.1}$$

where n is the diffraction order, λ is the wavelength of the spectral line, α is the angle of incidence, R is the radius of curvature of the grating and x is the length of the arc between the center of the grating and the position of the spectral line along the Rowland circle [172].

Experimentally, only the relative positions of spectral lines can be mea-

Table A.1: Grating line density and corresponding wavelength range

Grating (lines mm^{-1})	Wavelength range (nm)
1200	5 - 15
600	10 - 30
300	20 - 60

sured because it is not possible to measure x directly. Therefore, identifying the lines requires us to assume that some are already known and for this, two approaches can be taken. The first approach is a numerical method which exploits the fact that the high harmonic spectrum consists of the odd harmonics of the driving laser. The second approach uses spectral lines from a helium discharge to accurately calibrate the spectrometer.

A.2.1 Numerical Calibration

Since the fundamental wavelength is an integer multiple of the harmonic wavelength, the wavelength separation between the harmonics exist in a unique ratio. In principle, by measuring these ratios the harmonics can be identified. By rearranging equation A.1 the theoretical position x of each harmonic on the detector can be calculated. If this is done for all possible sequences of harmonics and a least squares fit performed between the theoretical and measured positions it is possible to quickly calculate which sequence of harmonics the data represents. This technique works reasonably well for harmonics generated at lower laser intensities, since it assumes that the harmonics exist in simple ratios and that the center wavelength is well defined. However, in chapter 5 where it was seen that the ionization induced blue-shifting that occurs at high laser intensity can significantly change the spectrum of the driving laser and cause a shift in the harmonic peaks. This leads to significant ambiguity in the wavelength calibration

Table A.2: Emission lines from a helium discharge

Species	Wavelength (nm)	Reference
He II	24.3027	[173]
He II	25.6317	[173]
He II	30.3781	[173]
He I	52.2213	[174]
He I	53.7030	[175]
He I	58.4334	[175]
He I	59.1412	[175]

and prompted the development of an XUV calibration source so that the wavelength could be independently verified.

A.2.2 XUV Calibration Lamp

For an absolute wavelength calibration, a discharge in helium was used to produce a range of emission lines in the XUV region of the spectrum. Table A.2 summarizes some of the important lines that can be used for wavelength calibration that arise from the neutral (He I) and singly-ionized (He II) species.

The calibration lamp (figure A.2) was a water-cooled, cold-cathode DC capillary discharge source [171] based on a design by Morris [176]. The discharge was confined to a Pyrex capillary approximately 10 cm in length with a bore of 1 mm. A hollow electrode, which doubles as the gas inlet, was placed at the entrance of the capillary. A needle valve was used to regulate the pressure of helium gas supplied to the capillary and the lamp was pumped by a small rotary pump (Leybold Trivac D25B). The electrode and capillary were held in a boron nitride tube which had excellent thermal properties and was a good electrical insulator. The voltage across the discharge tube was increased using a variable supply until the discharge

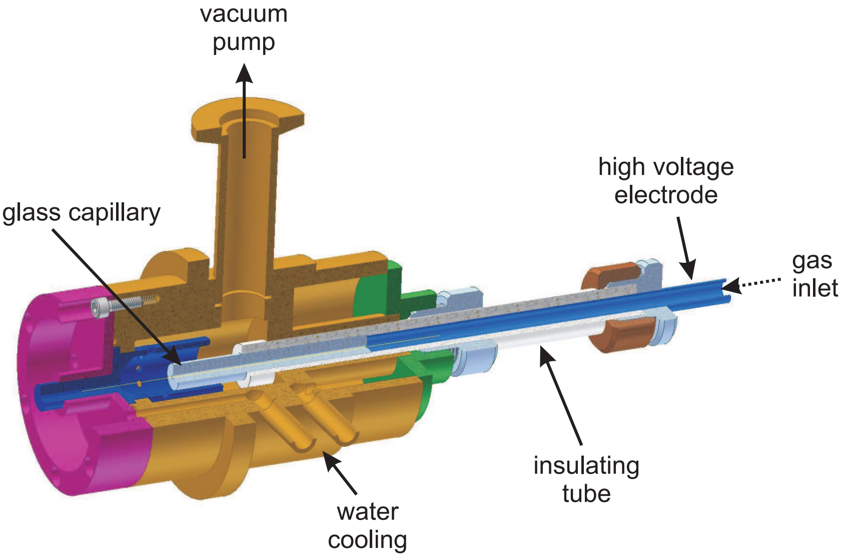

Figure A.2: The water-cooled cold cathode capillary discharge source.

‘strikes’. The striking potential, ∼ 2 kV, was typically much greater than the operating potential, ∼ 600 V, necessary to maintain the discharge.

Helium discharge spectra (figure A.3(a)) were acquired with the XUV spectrometer using the 300 lines/mm grating. Curve-fitting the peaks with a mixed Gaussian-Lorentzian function using the fityk software package gave the center position of each peak. These peak positions were then plotted against their corresponding wavelength assignment, taken from table A.2, to give a calibration curve for the spectrometer (figure A.3(b)).

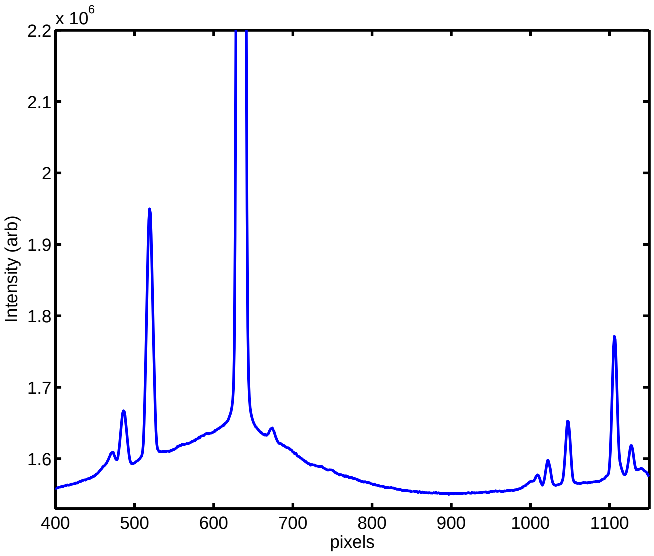

(a)

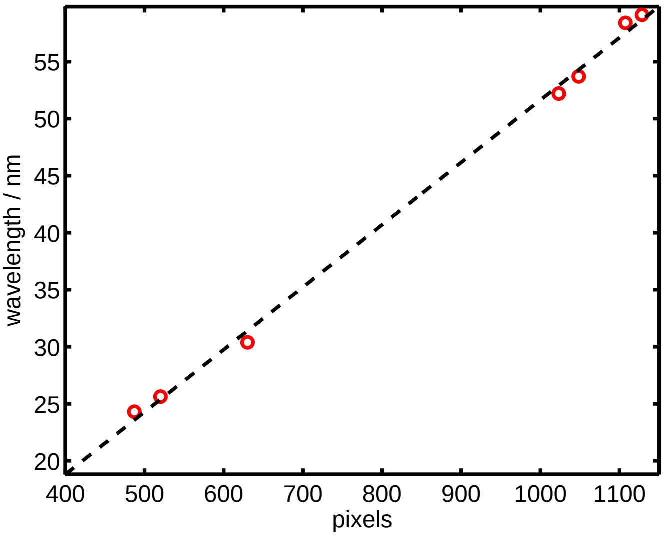

(b)

Figure A.3: (a) The helium discharge spectrum acquired with the XUV spectrometer and 300 lines mm^{-1} grating, and (b) a typical spectrometer wavelength calibration curve.

References

[1] Roentgen WC. “On a new kind of rays”. *Nature*, 53:274, 1896.

[2] Schawlow AL and Townes CH. “Infrared and optical masers”. *Physical Review Letters*, 112(6):1940–1949, 1958.

[3] Maiman TH. “Stimulated optical radiation in ruby”. *Nature*, 187(4736):493–494, 1960.

[4] T. Pfeifer, C. Spielmann, and G. Gerber. “Femtosecond X-ray science”. *Reports on Progress in Physics*, 69:443–505, 2006.

[5] J. Evans. “Brilliant opportunities across the spectrum”. *Physical Chemistry Chemical Physics*, 8:3045, 2006.

[6] “FLASH: The free-electron laser in Hamburg”. Technical report, DESY, 2007.

[7] E. Plonjes, J. Feldhaus, and T. Moller. “Taking free-electron lasers into the X-ray regime”. *Physics World*, 16(7):33–37, 2003.

[8] G. Sansone, E. Benedetti, F. Calegari, C. Vozzi, L. Avaldi, R. Flammini, L. Poletto, P. Villoresi, C. Altucci, R. Velotta, S. Stagira, S. De Silvestri, and M. Nisoli. “Isolated single-cycle attosecond pulses”. *Science*, 314(5798):443–446, 2006.

[9] C. A. Froud, E. T. F. Rogers, D. C. Hanna, W. S. Brocklesby, M. Praeger, A. M. de Paula, J. J. Baumberg, and J. G. Frey. “Soft X-ray

wavelength shift induced by ionization effects in a capillary". *Optics Letters*, 31(3):374–376, 2006.

[10] J. Seres, P. Wobrauschek, C. Streli, V.S. Yakvlev, E. Seres, F. Krausz, and C. Spielmann. "Generation of coherent keV X-rays with intense femtosecond laser pulses". *New Journal of Physics*, 8(251), 2006.

[11] J.A. Bearden. "X-Ray wavelengths". *Reviews of Modern Physics*, 39(1):78–124, 1967.

[12] D. Attwood. *Soft X-rays and extreme ultraviolet radiation: Principles and applications*. Cambridge University Press, first edition, 1999.

[13] J-F. Adam, J-P. Moy, and J. Susini. "Table-top water window transmission X-ray microscopy: Review of the key issues, and conceptual design of an instrument for biology". *Review of Scientific Instruments*, 76:091301, 2005.

[14] B. L. Henke, E. M. Gullikson, and J. C. Davis. "X-ray interactions - photoabsorption, scattering, transmission, and reflection at E=50-30,000 Ev, Z=1-92". *Atomic Data and Nuclear Data Tables*, 54(2):181–342, 1993.

[15] D. Gabor. "A new microscopic principle". *Nature*, 161:777, 1948.

[16] G. Faigel and M. Tegze. "X-ray holography". *Reports on Progress in Physics*, 62:355, 1999.

[17] R.W. Gerchberg and W.O. Saxton. "Phase determination from image and diffraction plane pictures in the electron microscope". *Optik*, 35:237–246, 1972.

[18] J. R. Fienup. "Phase retrieval algorithms - a comparison". *Applied Optics*, 21(15):2758–2769, 1982.

[19] S. Eisebitt, J. Luning, W.F. Schlotter, M. Lorgen, O. Hellwig, W. Eberhardt, and J. Stohr. "Lensless imaging of magnetic nanostructures by X-ray spectro-holography". *Nature*, 432:885, 2004.

[20] T. Araki, A. Harald, J.M. Stubbs, D.C Sundberg, G.E. Mitchell, J.B. Kortright, and A.L.D. Kilcoyne. "Resonant soft X-ray scattering from structured polymer nanoparticles". *Applied Physics Letters*, 89:124106, 2006.

[21] P.D. Hatton, S.B. Wilkins, T.A.W. Beale, T.K. Johal, D. Prabhakaran, and A.T. Boothroyd. "Resonant X-ray scattering - a new probe of charge, spin and orbital ordering in the manganites". *Journal of Magnetism and Magnetic Materials*, 290-291:891, 2005.

[22] D. I. Svergun. "Restoring low resolution structure of biological macromolecules from solution scattering using simulated annealing". *Biophys. J.*, 76(6):2879–2886, 1999.

[23] Jonathan M. Dugan and Russ B. Altman. "Using surface envelopes for discrimination of molecular models". *Protein Sci*, 13(1):15–24, 2004.

[24] R. Neutze, R. Wouts, D. van der Spoel, E. Weckert, and J. Hajdu. "Potential for biomolecular imaging with femtosecond X-ray pulses". *Nature*, 406(6797):752–757, 2000.

[25] R. Neutze, G. Huldt, J. Hajdu, and D. van der Spoel. "Potential impact of an X-ray free electron laser on structural biology". *Radiation Physics and Chemistry*, 71:905–916, 2004.

[26] M.H. Vos and J-L. Martin. "Femtosecond processes in proteins". *Biochimica et Biophysica Acta*, 1411:1–20, 1999.

[27] L.A. Peteanu, R.W. Schoenlein, Q. Wang, R.A. Mathies, and C.V. Shank. "The first step in vision occurs in femtosecond: Complete blue and red spectral studies". *Proceedings of the National Academy of Sciences of the United States of America*, 90:11762–11766, 1993.

[28] A. Rousse, C. Rischel, and J-C. Gauthier. "Colloquium: Femtosecond X-ray crystallography". *Reviews of Modern Physics*, 73:17–31, 2001.

[29] A.M. Lindenberg, Y. Acremann, D.P. Lowney, P.A. Heimann, T.K. Allison, T. Matthews, and R.W. Falcone. "Time-resolved measurements of the structure of water at constant density". *The Journal of Chemical Physics*, 122:204508, 2005.

[30] N. Chayden and J. Helliwell. "Protein crystallography: the human genome in 3-D". *Physics World*, (May):43, 1998.

[31] M.L. Pusey, Liu Z-H, W. Tempel, J. Praissman, D. Lin, B-C. Wang, J.A. Gavira, and Ng J.D. "Life in the fast lane for protein crystallization and X-ray crystallography". *Progress in Biophysics and Molecular Biology*, 88:359–386, 2005.

[32] A.S. Moffat. "Opening the door to more membrane protein structures". *Science*, 277(5332):1607–1608, 1997.

[33] W.E. Moerner. "A dozen years of single-molecule spectroscopy in physics, chemistry and biophysics". *Journal of Physical Chemistry B*, 106:910–927, 2002.

[34] E.A. Lipman, B. Schuler, O. Bakajin, and W.A. Eaton. "Single-molecular measurement of protein folding kinetics". *Science*, 301:1233–1235, 2003.

[35] S. Weiss. “Measuring conformational dynamics of biomolecules by single molecule fluorescence spectroscopy”. *Nature Structural Biology*, 7:724–729, 2000.

[36] W. Clegg. *Crystal structure determination*. Oxford University Press, 1998.

[37] J. Miao, H.N. Chapman, J. Kirz, D. Sayre, and K.O. Hodgson. “Taking X-ray diffraction to the limit: macromolecular structures from femtosecond X-ray pulses and diffraction microscopy of cells with synchrotron radiation”. *Annual Reviews of Biophysics and Biomolecular Structure*, 33:157–176, 2004.

[38] Z. Dauter. “Current state and prospects of macromolecular crystallography”. *Acta Crystallographica D*, 62:1–11, 2006.

[39] D. Sayre, H. N. Chapman, and J. Miao. “On the extendibility of X-ray crystallography to noncrystals”. *Acta Crystallographica Section A*, 54:232–239, 1998.

[40] J. W. Miao, P. Charalambous, J. Kirz, and D. Sayre. “Extending the methodology of X-ray crystallography to allow imaging of micrometre-sized non-crystalline specimens”. *Nature*, 400(6742):342–344, 1999.

[41] “Protein data bank”. http://www.rcsb.org/pdb/home/home.do.

[42] J. Miao, K.O. Hodgson, and D. Sayre. “An approach to three-dimensional strucutres of biomolecules by using single-molecule diffraction images”. *Proceedings of the National Acamdemy of Science*, 98:6641–6645, 2001.

[43] G. Webster and R. Hilgenfeld. "Perspectives on single molecule diffraction using the X-ray free electron laser". *Single Molecules*, 3(1):63–68, 2002.

[44] J.M. Berg, J.L. Tymoczko, and L. Stryer. *Biochemistry*. W.H. Freeman, fifth edition, 2002.

[45] International Human Genome Sequencing Consortium. "Initial sequencing and analysis of the human genome". *Nature*, 409:860–921, 2001.

[46] E. Pennisi. "Bioinformatics - Gene counters struggle to get the right answer". *Science*, 301(5636):1040–1041, 2003.

[47] M. Mann and O. N. Jensen. "Proteomic analysis of post-translational modifications". *Nature Biotechnology*, 21(3):255–261, 2003.

[48] A. Wlodawer. "Rational approach to AIDS drug design through structural biology". *Annual Reviews in Medicine*, 53:595–614, 2002.

[49] R. Henderson. "Cryoprotection of protein crystals against radiation damage in electron and X-ray diffraction". *Proceedings of the Royal Society of London: Biological Science*, 241:6–8, 1990.

[50] J. Hajdu. "Single-molecule X-ray diffraction". *Current Opinion in Structural Biology*, 10(5):569–573, 2000.

[51] J.C. Solem and G.C. Baldwin. "Microholography of living organisms". *Science*, 218:229–235, 1982.

[52] K.J. Gaffney and H.N. Chapman. "Imaging atomic structure and dynamics with ultrafast X-ray scattering". *Science*, 316:1444–1448, 2007.

[53] R.P. Millane. "Phase retrieval in crystallography and optics". *Journal of the Optical Society of America A*, 7:394–411, 1990.

[54] J. Miao and D. Sayre. "On possible extensions of X-ray crystallography through diffraction-pattern oversampling". *Acta Crystallographica Section A*, 56:596–605, 2000.

[55] J. Miao, D. Sayre, and H.N. Chapman. "Phase retrieval from the magnitude of the Fourier transforms of nonperiodic object". *Journal of the Optical Society of America A*, 15:1662–1669, 1998.

[56] J.H. Sheldin and J.R. Fienup. "Numerical investigation of the uniqueness of phase retrieval". *Journal of the Optical Society of America A*, 7:412–427, 1990.

[57] J. Miao, T. Ishikawa, E.H. Anderson, and K.O. Hodgson. "Phase retrieval of diffraction patterns from noncrystalline samples using the oversampling method". *Physical Review B*, 67:174104, 2003.

[58] J. Miao, K.O. Hodgson, T. Ishikawa, C.A. Larabell, M.A. LeGros, and Y. Nishino. "Imaging whole Escherichia coli bacteria by using single-particle X-ray diffraction". *Proceedings of the National Academy of Science*, 100:110–112, 2003.

[59] S. Marchesini, H.N. Chapman, S.P. Hau-Riege, A. Noy, M.R. Howells, U. Weierstall, and J.C.H. Spence. "X-ray image reconstruction from a diffraction pattern alone". *Physical Review B*, 68:140101, 2003.

[60] J.R. Fienup. "Reconstruction of a complex-valued object from the modulus of its Fourier transform using a support constraint". *Journal of Optical Society of America A*, 4:118–123, 1987.

[61] H. N. Chapman, A. Barty, M. J. Bogan, S. Boutet, M. Frank, S. P. Hau-Riege, S. Marchesini, B. W. Woods, S. Bajt, H. Benner, R. A. London, E. Plonjes, M. Kuhlmann, R. Treusch, S. Dusterer, T. Tschentscher, J. R. Schneider, E. Spiller, T. Moller, C. Bostedt, M. Hoener, D. A. Shapiro,

K. O. Hodgson, D. Van der Spoel, F. Burmeister, M. Bergh, C. Caleman, G. Huldt, M. M. Seibert, Frnc Maia, R. W. Lee, A. Szoke, N. Timneanu, and J. Hajdu. "Femtosecond diffractive imaging with a soft X-ray free-electron laser". *Nature Physics*, 2(12):839–843, 2006.

[62] H.N. Chapman, A. Barty, S. Marchesini, A. Noy, S.P. Hau-Riege, C. Cui, M.R. Howells, R. Rosen, H. He, J.C.H. Spence, U. Weierstall, T. Beetz, C. Jacobesen, and D. Shapiro. "High-resolution ab initio three-dimensional X-ray diffraction microscopy". *Journal of the Optical Society of America A*, 23:1179–1200, 2006.

[63] M.A. Tito, K. Tars, K. Valegard, J. Hajdu, and C.V. Robinson. "Electrospray time of flight mass spectrometry of intact NS2 virus capsids". *Journal of the American Chemical Society*, 122:3550–3551, 2000.

[64] M. van Heel, E.V. Orlova, G. Harauz, H. Startk, P. Dube, F. Zemlin, and M. Schatz. "Angular reconstitution in three-dimensional electron microcopy: historical and theoretical aspects". *Scanning Microscopy*, 11:195–210, 1997.

[65] G. Huldt, A. Szoke, and J. Hajdu. "Diffraction imaging of single particles and biomolecules". *Journal of the Structural Biology*, 144:219–227, 2003.

[66] J.F. Hergott, M. Kovacev, H. Merdji, C. Hubert, Y. Mairesse, J.P. Breger, P. Agostini, B. Carré, and P. Salières. "Extreme-ultraviolet high-order harmonics pulses in the microjoule range". *Physical Review A*, 66:021801–3, 2002.

[67] Z. H. Chang, A. Rundquist, H. W. Wang, M. M. Murnane, and H. C. Kapteyn. "Generation of coherent soft X-rays at 2.7 nm using high harmonics". *Physical Review Letters*, 79(16):2967–2970, 1997.

[68] A. McPherson, G. Gibson, H. Jara, U. Johann, T.S. Luk, I.A. McIntyre, K. Boyer, and C.K. Rhodes. "Studies of multiphoton production of vacuum-ultraviolet radiation in the rare gases". *Journal of the Optical Society of America B*, 4:595–601, 1987.

[69] M. Ferray, A. L'Huillier, X.F. Li, L.A. Lompre, G. Mainfray, and C. Manus. "Multiple-harmonic conversion of 1064 nm radiation in rare gases". *Journal of Physics B: Atomic, Molecular and Optical Physics*, 21:31–35, 1998.

[70] R.W. Boyd. *Nonlinear Optics*. Academic Press, second edition, 2003.

[71] P.B. Corkum. "Plasma perspectives on strong-field multiphoton ionization". *Physical Review Letters*, 71:1994–1997, 2003.

[72] M. Protopapas, C.H. Keitel, and P.L. Knight. "Atomic physics with super-high intensity lasers". *Reports of Progress in Physics*, 60:389–486, 1997.

[73] B.H. Bransden and C.J. Joachain. *Physics of Atoms and Molecules*. Benjamin Cummings, second edition, 2003.

[74] V. S. Popov. "Tunnel and multiphoton ionization of atoms and ions in a strong laser field (Keldysh theory)". *Physics-Uspekhi*, 47(9):855–885, 2004.

[75] A.R. Rundquist. *Phase-matched generation of coherent, ultrafast X-rays using high harmonics*. PhD thesis, Washington State University, 1998.

[76] C. Lynga, M.B. Gaarde, C. Delfin, M. Bellini, T.W. Hansch, A.L. L'Huillier, and C.G. Wahlström. "Temporal coherence of high-order harmonics". *Physical Review A*, 60:4823–4830, 1999.

[77] Z. H. Chang, A. Rundquist, H. W. Wang, I. Christov, M. M. Murnane, and H. C. Kapteyn. "Generation of coherent, femtosecond, X-

ray pulses in the ”water window””. *Ieee Journal of Selected Topics in Quantum Electronics*, 4(2):266–270, 1998.

[78] E. A. Gibson, A. Paul, N. Wagner, R. Tobey, S. Backus, I. P. Christov, M. M. Murnane, and H. C. Kapteyn. “High-order harmonic generation up to 250 eV from highly ionized argon”. *Physical Review Letters*, 92(3), 2004.

[79] D. Gaudiosi, B. Reagan, T. Popmintchev, M. Grisham, M. Berrill, O. Cohen, B.C. Walker, M. Murnane, H. Kapteyn, and J.J. Rocca. “High-order harmonic generation from ions in a capillary discharge”. *Physical Review Letters*, 96:203001, 2006.

[80] M. Lewenstein, P. Balcou, M.Y. Ivanov, A. L’Huillier, and P.B. Corkum. “Theory of high-harmonic generation by low-frequency laser fields”. *Physical Review A*, 49(3):2117, 1994.

[81] P. Balcou, P. Salieres, A. L’Huillier, and M. Lewenstein. “Generalized phase-matching conditions for high-harmonics: The role of field-gradient forces”. *Physical Review A*, 55(4):3204–3210, 1997.

[82] E. A. Gibson. *Quasi-phase matching of soft X-ray light from high-order harmonic generation using waveguide structures*. PhD thesis, Colorado School of Mines, 2004.

[83] C. de Lisio, R. Altucci, C. an Bruzzese, F. De Filippo, S. Solimeno, M. Bellini, and P. Foggi. “Harmonic generation in an ionzied gas medium with a 100-femtosecond, high repetition rate laser source at intermediate intensities”. *Applied Physics B*, 64:323–330, 1997.

[84] Ch. Spielmann, N.H. Burnett, S. Sartania, R. Koppitsch, M. Schnurer, C. Kan, M. Lenzner, P. Wobrauschek, and F. Krausz. “Generation of coherent X-rays in the water window using 5-femtosecond laser pulses”. *Science*, 278:661, 1997.

[85] Y. Tamaki, J. Itatani, Y. Nagata, M. Obara, and K. Midorikawa. "Highly efficient, phase-matched high-harmonic generation by a self-guided laser beam". *Physical Review Letters*, 82(7):1422, 1999.

[86] A. Rundquist, C. G. Durfee, Z. H. Chang, C. Herne, S. Backus, M. M. Murnane, and H. C. Kapteyn. "Phase-matched generation of coherent soft X-rays". *Science*, 280(5368):1412–1415, 1998.

[87] M. Schnurer, Z. Cheng, S. Sartania, M. Hentschel, G. Tempea, T. Brabec, and F. Krausz. "Guiding and high-harmonic generation of sub-10-fs pulses in hollow-core fibres at 10^{15} W/cm^2". *Applied Physics B-Lasers and Optics*, 67:263–266, 1998.

[88] A.E. Siegman. "How to (maybe) measure laser beam quality". Optical Society of America Annual Meeting, Long Beach, California, 1997.

[89] A. Paul, E. A. Gibson, X. S. Zhang, A. Lytle, T. Popmintchev, X. B. Zhou, M. M. Murnane, I. P. Christov, and H. C. Kapteyn. "Phase-matching techniques for coherent soft X-ray generation". *IEEE Journal of Quantum Electronics*, 42(1-2):14–26, 2006.

[90] M. Schnurer, Z. Chang, M. Hentschel, G. Tempea, P. Kalman, T. Brabec, and F. Krausz. "Absorption-limited generation of coherent ultrashort soft X-ray pulses". *Physical Review Letters*, 83(4):722–725, 1999.

[91] M. Schnurer, Z. Cheng, M. Hentschel, F. Krausz, T. Wilhein, D. Hambach, G. Schmahl, M. Drescher, Y. Lim, and U. Heinzmann. "Few-cycle-driven XUV laser harmonics: Generation and focusing". *Applied Physics B-Lasers and Optics*, 70:S227–S232, 2000.

[92] Y. Tamaki, J. Itatani, M. Obara, and K. Midorikawa. "Optimization of conversion efficiency and spatial quality of high-order harmonics generation". *Physical Review A*, 62:063802, 2000.

[93] E.A.J. Marcatili and R.A. Schmeltzer. "Hollow metallic and dielectric waveguides for long distance optical transmission and lasers". *Bell Systems Technical Journal*, 43:1783–1809, 1964.

[94] A. Dalgarno and A.E. Kingston. "The refractive indices and Verdet constants of the inert gases". *Proceedings of the Royal Society of London, Seies A, Mathematical and Physical Sciences*, 259(1298):424, 1960.

[95] C. G. Durfee, A. R. Rundquist, S. Backus, C. Herne, M. M. Murnane, and H. C. Kapteyn. "Phase matching of high-order harmonics in hollow waveguides". *Physical Review Letters*, 83(11):2187–2190, 1999.

[96] E. M. Gullikson. "Center for X-ray optics: Optical constants". http://cxro-lbl.gov/optical_constants/.

[97] E.T.F. Rogers, C.A. Froud, W.S. Brocklesby, D.C. Hanna, S.L. Stebbings, A.M. de Paula, M. Praeger, J.J. Baumberg, and J.G. Frey. "Spatially and temporally resolved phase matching calculations for high harmonics generation in a capillary". *Manuscript in preparation*.

[98] E. Constant, D. Garzella, P. Breger, E. Mevel, Ch. Dorrer, C. Le Blanc, F. Salin, and P Agostini. "Optimizing high harmonic generation in absorbing gases: Model and experiment". *Physical Review Letters*, 82(8):1668, 1999.

[99] U. Keller. "Recent developments in compact ultrafast lasers". *Nature*, 424:831–838, 2003.

[100] R. Ell, U. Morgner, F.X. Kartner, J.G. Fujimoto, E.P. Ippen, V. Scheuer, G. Angelow, T. Tschudi, M.J. Lederer, A. Boiko, and B. Luther-Davies. "Generation of 5-fs pulses and octave-spanning spectra directly from a Ti:Sapphire laser". *Optics Letters*, 26(6):373–375, 2001.

[101] S. Backus, C. G. Durfee, M. M. Murnane, and H. C. Kapteyn. "High power ultrafast lasers". *Review of Scientific Instruments*, 69(3):1207–1223, 1998.

[102] M.T. Asaki, C-P. Huang, D. Garvey, J. Zhou, H. C. Kapteyn, and M.M. Murnane. "Generation of 11-fs pulses from a self-mode-locked Ti:Sapphire laser". *Optics Letters*, 18(12):977–979, 1993.

[103] D.E. Spence, P.N. Kean, and W. Sibbett. "60-fsec pulse generation from a self-mode-locked Ti:Sapphire laser". *Optics Letters*, 16(1):42–44, 1991.

[104] U. Keller, G.W. 'tHooft, W.H. Knox, and J.E. Cunningham. "Femtosecond pulses from a continuously self-starting passively mode-locked Ti:Sapphire laser". *Optics Letters*, 16(13):1022–1024, 1991.

[105] F. Salin, J. Squier, and M. Piche. "Mode locking of Ti:Al_2O_3 lasers and self-focusing: A gaussian approximation". *Optics Letters*, 16(21):1674–1676, 1991.

[106] T. Brabec, Ch. Spielmann, P.F. Curley, and F. Krausz. "Kerr lens mode locking". *Optics Letters*, 17(18):1292–1294, 1992.

[107] J. Herrmann. "Theory of Kerr-lens mode locking: role of self-focusing and radially varying gain". *Journal of the Optical Society of America B-Optical Physics*, 11(3):498–512, 1994.

[108] P.F. Moulton. "Spectroscopic and laser characteristics of Ti:Al_2O_3". *Journal of the Optical Society of America B-Optical Physics*, 3(1):125–133, 1986.

[109] J. Zhou, G. Taft, C-P. Huang, M.M. Murnane, H.C. Kapteyn, and I.P. Christov. "Pulse evolution in a broad-bandwidth Ti:Sapphire laser". *Optics Letters*, 19(15):1149–1151, 1994.

[110] T. Brabec, Ch. Spielmann, and F. Krausz. "Limits of pulse shortening in solitary lasers". *Optics Letters*, 17(10):748–750, 1992.

[111] I.P. Christov, V.D. Stoev, M.M. Murnane, and H.C. Kapteyn. "Sub-10fs operation of Kerr-lens mode-locked lasers". *Optics Letters*, 21(18):1493–1495, 1996.

[112] G. Steinmeyer, D.H. Sutter, L. Gallmann, N. Matuschek, and U. Keller. "Frontiers in ultrashort pulse generation: Pushing the limits in linear and nonlinear optics". *Science*, 286:1507–1512, 1999.

[113] F. Verluise, V. Laude, Z. Cheng, C. Spielmann, and P. Tournois. "Amplitude and phase control of ultrashort pulses by use of an acousto-optic programmable dispersive filter: pulse compression and shaping". *Optics Letters*, 25(8):575–577, 2000.

[114] P. Tournois. "Acousto-optic programmable dispersive filter for adaptive compensation of group delay time dispersion in laser system". *Optics Communications*, 140:245–249, 2007.

[115] G.D. Reid and K. Wynne. "Ultrafast laser technology and spectroscopy". In *Enyclopedia of Analytical Chemistry*. John Wiley and Sons, 2000.

[116] R. Trebino. *Frequency-resolved optical gating: the measurement of ultrashort laser pulses*. Springer, first edition, 2002.

[117] P. O'Shea, M. Kimmel, X. Gu, and R. Trebino. "Highly simplified device for ultrashort-pulse measurement". *Optics Letters*, 26:932–934, 2001.

[118] P. O'Shea, M. Kimmel, and R. Trebino. "Increased phase-matching bandwidth in simple ultrashort-laser-pulse measurements". *Journal of Optics B: Quantum and Semiclassical Optics*, 4:44–48, 2002.

[119] E. Hecht. *Optics*. Addison-Wesley, second edition, 1998.

[120] R. K. Nubling and J. A. Harrington. “Launch conditions and mode coupling in hollow-glass waveguides”. *Optical Engineering*, 37(9):2454–2458, 1998.

[121] M. Praeger. University of Southampton Internal Report, 2006.

[122] J.S. Robinson, C.A. Haworth, H. Teng, R.A. Smith, J.P. Marangos, and J.W.G. Tisch. “The generation of intense, transform-limited laser pulses with tunable duration from 6 to 30fs in a differentially pumped hollow fibre”. *Applied Physics B: Lasers and Optics*, 85(4):525–529, 2006.

[123] A. C. Tien, S. Backus, H. Kapteyn, M. Murnane, and G. Mourou. “Short-pulse laser damage in transparent materials as a function of pulse duration”. *Physical Review Letters*, 82(19):3883–3886, 1999.

[124] A. Hertwig, S. Martin, J. Kruger, and W Kautek. “Surface damage and color centers generated by femtosecond pulses in borosilicate glass and silica”. *Applied Physics A*, 79:1075–1077, 2004.

[125] F. R. Powell and J.R. Fox. “Transmittance measurements for a variety of X-ray/EUV filter materials and pinhole leak measurements utilizing a new visible light photometer system.”. In R.B. Hoover and A.B.C. Walter, Jr, editors, *Proceedings of Multilayer and Grazing Incidence X-Ray/EUV Optics II*, volume 2011, pages 428–437. SPIE, 1993.

[126] F. R. Powell, P. W. Vedder, J. F. Lindblom, and S. F. Powell. “Thin-film filter performance for extreme ultraviolet and X-ray applications”. *Optical Engineering*, 29(6):614–624, 1990.

[127] F. Powell. "Care and feeding of soft X-ray and extreme ultraviolet filters". In *Laser-induced Damage in Optical Materials*, volume 1848, pages 503–514. SPIE, 1992.

[128] M. Praeger, A.M. de Paula, C.A. Froud, E.T.F. Rogers, S.L. Stebbings, W.S. Brocklesby, J.J. Baumberg, D.C. Hanna, and J.G. Frey. "Spatially resolved soft X-ray spectrometry from a single-image diffraction". *Nature Physics*, 3.

[129] M. Born and E. Wolf. *Principles of optics*. Cambridge University Press, seventh edition, 1999.

[130] C. Altucci, R. Bruzzese, C. de Lisio, M. Nisoli, S. Stagira, De Silvestrim S., O. Svelto, A. Boscolo, P. Ceccherini, L. Poletto, G. Tondello, and P. Villoresi. "Tunable soft X-ray radiation by high-order harmonic generation". *Physical Review A*, 61:021801, 1999.

[131] F. Zhong, J. Deng, X. Hu, Z. Li, Z. Zhang, and Z. Xu. "The effects of ionization of gases on the high harmonics splitting". *Physics Letters A*, 278:35–43, 2000.

[132] W.M. Wood, G. Focht, and M.C. Downer. "Tight focusing and blue shifting of millijoule femtosecond pulses from a conical axicon amplifier". *Optics Letters*, 13(11), 1988.

[133] G. Agrawal. *Nonlinear Fiber Optics*. Academic Press, third edition, 2001.

[134] M.B. Gaarde, M. Murakami, and R. Kienberger. "Spatial separation of large dynamical nlue shift and harmonics generation". *Physical Review A*, 74:053401, 2006.

[135] T. Pfeifer and M.C. Downer. "Direct experimental observation of periodic intensity modulation along a straight hollow-core optical waveguide". *Journal of the Optical Society of America B*, 24(5), 2007.

[136] "National Institute of Standards and Technology Physical Reference Database:". http://physics.nist.gov/PhysRefData/Handbook/.

[137] B. Dromey, M Zepf, M. Landreman, and S.M. Hooker. "Quais-phasematching of harmonic generation via multimode beating in waveguides". *Optics Express*, 15:7894, 2007.

[138] E. A. Gibson, A. Paul, N. Wagner, R. Tobey, D. Gaudiosi, S. Backus, I. P. Christov, A. Aquila, E. M. Gullikson, D. T. Attwood, M. M. Murnane, and H. C. Kapteyn. "Coherent soft X-ray generation in the water window with quasi-phase matching". *Science*, 302(5642):95–98, 2003.

[139] M. Bargheer, N. Zhavoronkov, R. Bruch, H. Legall, H. Stiel, M. Woerner, and T. Elsaesser. "Comparison of focusing optics for femtosecond X-ray diffraction". *Applied Physics B-Lasers and Optics*, 80(6):715–719, 2005.

[140] W. L. Chao, B. D. Harteneck, J. A. Liddle, E. H. Anderson, and D. T. Attwood. "Soft X-ray microscopy at a spatial resolution better than 15nm". *Nature*, 435(7046):1210–1213, 2005.

[141] J.M. Kenney, C. Jacobsen, J. Kirz, and H. Rarback. "Absorption microanalysis with a scanning soft X-ray microscope: Mapping the distribution of calcium in bone". *Journal of Microscopy*, 138(3):321–328, 1985.

[142] X. D. Zhang, R. Balhorn, J. Mazrimas, and J. Kirz. "Measuring DNA to protein ratios in mammalian sperm head by XANES imaging". *Journal of Structural Biology*, 116(3):335–344, 1996.

[143] W. R. Hunter. "Measurement of optical-properties of materials in the vacuum ultraviolet spectral region". *Applied Optics*, 21(12):2103–2114, 1982.

[144] C. Tarrio, R.N. Watts, T.B. Lucatorto, J.M. Slaughter, and C.M. Falco. "Optical constants of in situ-deposited films of important extreme-ultraviolet multilayer mirror materials". *Applied Optics*, 37(19):4100–4105, 1998.

[145] R. Soufli and E.M. Gullikson. "Reflectance measurements on clean surfaces for the determination of optical constants of silicon in the extreme ultraviolet soft X-ray region". *Applied Optics*, 36(22):5499–5507, 1997.

[146] U. Bonse and M. Hart. "An X-ray interferometer". *Applied Physics Letters*, 6(8):155–156, 1965.

[147] J. Svatos, D. Joyeux, and D Phalippou. "Soft X-ray interferometer for measuring the refractive index of materials". *Optics Letters*, 18(16):1367–1369, 1993.

[148] E. M. Gullikson, P. Denham, S. Mrowka, and J.H. Underwood. "Absolute photoabsorption measurements of Mg, Al, and Si in the soft X-ray region below the $L_{2,3}$ edges". *Physical Review B*, 49(23):16283, 1994.

[149] R. Soufli and E. M. Gullikson. "Absolute photoabsorption measurements of molybdenum in the range 60-930 eV for optical constant determination". *Applied Optics*, 37(10):1713–1719, 1998.

[150] V.L. Kantsyrev, R. Bruch, R. Phaneuf, and N.G. Publicover. "New concepts for X-rays, soft X-ray, and EUV optical instrumentation including applications in spectroscopy, plasma diagnostics, and

biomedical microscopy: a status report.". *Journal of X-ray Science and Technology*, 7:139–158, 1997.

[151] A.H. Compton and S.K. Allison. *X-rays in theory and practice*. Van Nostrand, New York, 1935.

[152] B. Lengeler, J. Tummler, A. Snigirev, I. Snigireva, and C. Raven. "Transmission and gain of singly and doubly focusing refractive X-ray lenses". *Journal of Applied Physics*, 84(11):5855–5861, 1998.

[153] B. Lengeler, C.G. Schroer, M. Kuhlmann, B. Benner, T.F. Gunzler, O. Kurapova, F. Zontone, A. Snigirev, and I. Snigireva. "Refractive X-ray lenses". *Journal of Physics D: Applied Physics*, 38:218–222, 2005.

[154] N.R. Pereira, E.M. Dufresne, R. Clarke, and D.A. Arms. "Parabolic lithium refractive optics for X-rays". *Review of Scientific Instruments*, 75(1):37–41, 2004.

[155] E. H. Anderson. "Nanofabrication and diffractive optics for high-resolution X-ray applications". *Journal of Vacuum Science and Technology B*, 18:2970–2975, 2000.

[156] P. Kirkpatrick and A.V. Baez. "Formation of optical images by X-rays". *Journal of the Optical Society of America*, 38(9):766, 1948.

[157] C. Liu, L. Assoufid, R. Conley, A.T. Macrander, G.E. Ice, and J.Z. Tischler. "Profile coating and its application for Kirkpatrick-Baez mirrors". *Optical Engineering*, 42(12):3622–3628, 2003.

[158] M.R. Howells, O. Combie, R.M. Duarte, S. Irick, A.A. MacDowell, H.A. Padmore, T.R. Renner, S. Rah, and R. Sandler. "Theory and practice of elliptically bent X-ray mirrors", Journal = Optical Engineering, Volume = 39, Number = 10, Pages = 2748-2762, Year = 2000".

[159] S. Matsuyama, H. Mimura, H. Ymoto, Y. Sano, K. Yamamura, and M. Yabashi. "Development of scanning X-ray fluorescence microscope with spatial resolution of 30 nm using Kirkpatrick-Baez mirror optics". *Review of Scientific Instruments*, 77.

[160] R. Huang and D.H. Bilderback. "Single-bounce monocapillaries for focusing synchrotron radiation: modeling, measurements and theoretical limits". *Journal of Synchrotron Radiation*, 13:74–84, 2006.

[161] L. Vincze. *Detailed ray-tracing code for capillary optics*. PhD thesis, University of Antwerp, 1995.

[162] S.B. Dabagov, A. Marcelli, G. Cappuccio, and E. Burattini. "On propagation of X-rays in capillary channels". *Applied Optics*, 39(19):170–177, 2002.

[163] S.V. Kukhlevsky, F. Flora, A. Marinai, K. Negrea, L. Palladino, Reale A., G. Tomassetti, A. Ritucci, G. Nyitray, and L. Kozma. "Diffraction of X-rays in capillary optics". *Applied Optics*, 39(6):1059–1063, 2000.

[164] E.A. Stern, Z. Kalman, A. Lewis, and K. Lieberman. "Simple method for focusing X-rays using tapered capillaries". *Applied Optics*, 27(24):5135–5139, 1988.

[165] P.P. Crooker, W.B. Colson, and J. Blau. "Representation of a gaussian beam by rays". *American Journal of Physics*, 74(8):722–727, 2006.

[166] W.H. Press. *Numerical recipes: the art of scientific computing*. Cambridge University Press, 1986.

[167] J.R. Miller. "Vector geometry for computer graphics". *IEEE Computer Graphics and Animation*, 66:66–73, 1999.

[168] D.H. Bilderback, S.A. Hoffman, and D. Thiel. "Nanometer spatial resolution achieved in hard X-ray imaging and laue diffraction experiments". *Science*, 263:201–203, 1994.

[169] D.H. Bilderback. "CHESS Newsletter: A new computerized capillary puller for hard x-ray applications", 1995.

[170] T. A. Birks and Y. W. Li. "The shape of fibre tapers". *Journal of Lightwave Technology*, 10(4):432–438, 1992.

[171] J.A.R. Samson. *Techniques of XUV spectroscopy*. Wiley and Sons, New York, 1967.

[172] T. Namioka. "Theory of the concave grating". *Journal of the Optical Society of America*, 49:446–460, 1959.

[173] J.D. Garcia and J.E. Mack. "Energy levels and line tables for one-electron atomic spectra". *Journal of the Optical Society of America*, 55(6):654, 1965.

[174] J.L. Tech and J.F. Ward. "Accurate wavelength measurement of the $1s2p\ ^3P^o - 2p^2\ ^3P$ transition in ^{4}He I". *Physical Review Letters*, 27(7):367, 1971.

[175] W.C Martin. "Energy levels and spectrum of natural helium". *Journal of the research of the national bureau of standards*, 64A:19–28, 1960.

[176] A. Morris, N. Jonathan, J.M. Dyke, P.D. Francis, N. Keddar, and J.D. Mills. "High-sensitivity photoelectron spectrometer for studying reactive transient species". *Review of Scientific Instruments*, 55(2):172, 1984.